High Pressure Synthesis and Characterization of Non-Oxide Superconductors

A Thesis

Submitted by

C. I. Sathish

In fulfillment for the Award of the Degree of

Doctor of Philosophy

Graduate School of Chemical Sciences and Engineering,

Hokkaido University, Japan

2013

Abstract

Non-oxide solid materials have attracted considerable attention owing to their unique magnetic and superconducting properties. Non-oxide superconducting materials are relatively stable against chemical attack, and the corresponding critical current density is relatively very high. These compounds have therefore been used in many practical and scientific applications. However, the synthesis of some of them by employing conventional methods like normal solid state reaction is difficult. I expected that a high-pressure and high-temperature technique would be beneficial in the synthesis of these compounds and in further exploring new-composition non-oxide materials with superior properties.

My focus of this study was on the synthesis of a high-quality superconducting non-oxide compound and in the detailed study of its crystal structure, superconducting nature, magnetic and thermal properties. To synthesize high-quality materials, I used a high-pressure and high-temperature method that involved quenching the sample to room temperature before releasing an applied pressure of typically 6-17 GPa. To characterize the materials, high-quality samples were analyzed by synchrotron X-ray diffraction, neutron diffraction, and their magnetic, electrical, and thermal properties were measured. In this study, I focused on three series of materials, namely, transition-metal carbide, BiS_2 layered chalcogenide, and Fe-based silicide.

The cubic δ-MoC phase in the transition-metal carbide was selected to be studied because the carbon stoichiometric phase has never been synthesized. A theoretical study predicted that in the case of stoichiometric MoC, if it is synthesized, superconductivity will appear at a critical temperature that is considerably higher than the critical temperatures that have thus far been achieved (14.7K was claimed to be the highest, although it was not experimentally proven). Under the high-pressure and high-temperature conditions, the cubic δ-$MoC_{0.681}$ and δ-$MoC_{0.746}$ phases were finally synthesized by heating at 6 GPa and 17 GPa, respectively. The stoichiometric MoC was unfortunately not synthesized under these pressure conditions. The characterization of the material indicated that carbon vacancies were formed in the host cubic structure and that the vacancies were highly robust even when the material was prepared from stoichiometric ratios of C and Mo. However, a thermodynamically stable structure with ordered vacancies did not account for the robust features; rather, the theoretically predicted inherent phonon instability at the stoichiometric composition may be the reason for the robust vacancies. In addition, the superconducting properties were intensively studied using a weak coupling model. The critical temperature of 14.3K was

evidenced to reflect the bulk nature of δ-$MoC_{0.746}$.

A new type of layered-structure material with bismuth and sulfur was claimed to be a superconductor, and it had a great impact on research on new superconducting materials. However, the detailed properties of the material and the cause for the superconductivity were not well established. In this study, the BiS_2 layered based $Bi_4O_4S_3$ and $LaOBiS_2$ phases were successfully synthesized by the high-pressure and the high-temperature technique, and their crystal structure and the superconductivity were investigated in detail. The results clearly indicated that the superconductivity does not truly reflect the bulk nature of the BiS_2 layered phases, regardless of the manner in which the compounds were synthesized. This conclusion contradicted the results of ongoing studies on these compounds.

Recently, Fe-based superconductors have attracted considerable attention, and many compounds in this series have been extensively studied. All the compounds are highly toxic in nature because the common As-containing unit (Fe_2As_2 layer) is essential for the superconductivity. Therefore, in this study, non-toxic or less-toxic superconductors were studied to enhance superconductivity further. The exploration of highly abundant silicon materials containing Fe was targeted: heavy fermion materials $Ln_2Fe_3Si_5$ (*Ln* = rare earth element) were prepared by the high-pressure synthesis method, and the chemical substitution effect was investigated. Note that thus far, few studies have focused on these compounds because of difficulties in their synthesis by conventional methods. To my knowledge, systematic chemical substitution has been achieved only little. In this study, successful synthesis of $Yb_2Fe_3Si_5$ and up to 40 at% substitution of Ca for Yb were achieved using the high-pressure synthesis technique, and the resultant systematic changes in the magnetic and electrical properties were analyzed in detail.

In summary, superconductivity and magnetism have been developed toward useful applications; however, many aspects of superconductivity and varieties of magnetism remain unclear, and therefore, there is great scope for future research on them. In the present study, I focused on three series of non-oxide superconducting materials and the potential for further development toward practically useful and scientifically significant superconductors.

List of Abbreviations

high-T_c	High Superconducting Transition Temperature
SC	Superconducting
HP HT	High-Pressure and High-temperature
CBS	Cu-Based Superconductor
PM	Paramagnetic
FM	Ferromagnetic
AFM	Antiferromagnetic
BCS	Bardeen, Cooper, and Schrieffer
AP	Ambient-Pressure
XRD	X-ray Diffraction
EPMA	Electron Probe Micro-Analysis
TEM	Transmission Electron Microscope
PPMS	Physical Properties Measurement System
MPMS	Magnetic Properties Measurement System
ZFC	Zero-Field-Cooled
FC	Field-Cooled
NIMS	National Institute for Materials Science
WHH	Werthamer-Helfland-Hoheberg
SAED	Selected-Area Electron-Diffraction
T_c	Transition temperature

High pressure Synthesis and Characterization of Non-oxide Superconductors

Contents

Chapter I Introduction

1.1 Origin and history of Superconductivity

Discoveries and inventions in the 20th century had renovated human lifestyle. Understanding about phenomenons are yet a mystery. It is a disclosure among such stands the discovery of superconductivity. On 10th July 1908, the great Dutch physicist Heike Kamerlingh Onnes at Leiden University Laboratory experienced his most glorious moment in his career by liquefied helium and opened a new chapter in low temperature physics [1]. Soon after in 8th April, 1911 he surprisingly found that the resistance of mercury dropped down at cryogenic temperatures using his recent invention liquidized helium as a refrigerant. At a temperature of 4.2K he observed that resistance abruptly disappeared as shown in Fig.1.1.1 [2]. This extraordinary phenomenon is called as *superconductivity* by him and the temperature at which it appears is called as *critical temperature* T_c, with this finding a new field in physics named superconductivity has given birth.

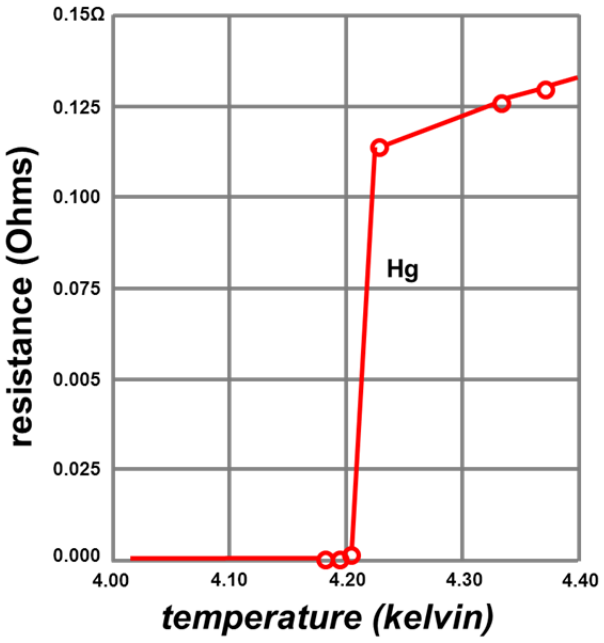

Fig.1.1.1. Resistivity drop in Mercury (extracted from Ref.2)

Later on he observed that by applying a strong magnetic field to a material it retains its normal state with an increase in resistance from zero. He also demonstrated the fact that superconducting materials remain in same state showing zero resistance even for many years. But in ordinary metal, induced current would get decayed rapidly, but superconducting

current rings remain same even for decades of years. Kamerlingh Onnes was awarded the Nobel Prize for physics in 1913 for his contribution and investigations on the properties of matter at low temperatures. And after a year he found an element lead showing superconductivity at T_c 7.2K. This invention paved path for lots of discoveries and many new phases of superconducting materials. A schematic view stating briefly about the history of superconductors that have been discovered so far [3-15] is shown in Fig.1.1.2.

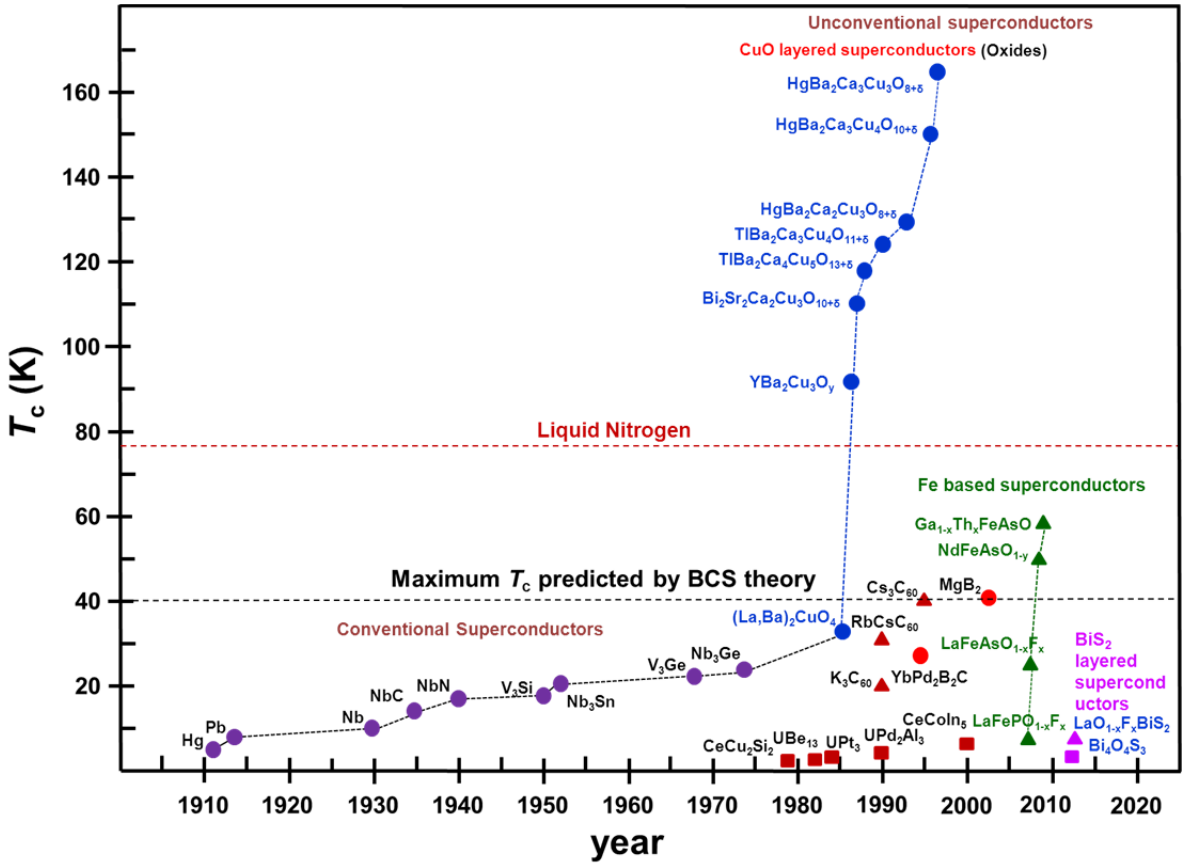

Fig.1.1.2. Brief history of Superconductors (extracted from Ref.3-15)

1.2 Advantages of high-pressure synthesis

High-pressure is an important tool for synthesizing novel phases of materials with different characteristics like composition, chemical bond, structure etc. [16-18]. It's a vast area in physics, materials research and engineering where researchers have lots of hope for developing new principles and permits an exact comparison between experiment and theoretical predictions. High-pressure synthesis favors the formation of compounds which are unable to be prepared by other synthesis technique. It enhances the intrinsic usefulness of this technique for creating new states of matter. The interesting phenomenon arises when the electronic structure of solids is affected by pressure and very large change occurs frequently

in resistance are observed. Phase changes occur without any change in crystal structure but there would be changes in volume and resistance. This change arises due to the electronic rearrangement within the band structure. [19, 20]. Regions of phase diagram that cannot be explored under ambient pressure can be done using high-pressure. Phases that are very stable at high-pressure can change to ambient pressure phase after releasing pressure. So stable high-pressure phase can be maintained while synthesis by immediately lowering the temperature to room temperature before releasing pressure. This process is called quenching which favors dense packing of ions, higher cation oxidation states, higher symmetry etc. [21, 22]. Many substances that exist only under high pressure cannot be obtained at ambient pressure conditions. For example $CaSiO_3$ is an abundant material present in the earth's crust but never detected at normal pressure due to instability through decompression [23].

High-pressure changes structure and properties of the materials in different ways which results in synthesizing new phases of materials. Some of the methods are thermodynamically high-pressure phases, kinetic non-equilibrium phases, intermediate energy phases, stable normal phases, meta-stable phases, modification of grains morphology and state of defects [24-29]. There are different types of high-pressure equipment developed so far. According to the static pressure ranging they are divided into Piston-cylinder type high pressure apparatus which can stabilize 0.1-1 GPa pressure, belt-type apparatus stabilizes 1-10 GPa, kawai-type multi-anvils 10-70 GPa and diamond anvils 100-300 GPa pressure. Schematic view of these anvils is shown in Fig.1.2.1 [30]. By varying the pressure different classifications of materials like super hard materials, wide-gap semiconductors, gems, diamonds, new metals, glasses, polymers, new superconducting materials, pristine substances, optical and insulator materials are synthesized using high-pressure apparatus.

High-pressure synthesis is successful in preparing multiferroic materials like $BiAlO_3$, $BiFeO_3$, $BiGaO_3$ etc. These materials have perovskite structure that shows ferroelectric and ferromagnetic properties [31, 32]. A mercury based high-T_c cuprates superconductors are synthesized under high-pressure which shows a maximum T_c of 164K [33]. Even sulfur element, a well-known wide-band gap insulator under pressure at about 100 GPa becomes metallic and shows a superconducting T_c of 10.1K, while further increasing the pressure to about 160 GPa it shows higher T_c of 17K [34]. As such *R*FeAsO (rare-earth metals) type Fe-based superconductors are also prepared using high-pressure that shows T_c above 40 K [35-37]. High-pressure synthesis favors more than ambient-pressure synthesis

such as enhanced reactivity, prevention of evaporation of materials and modification of phase diagram etc. [38].

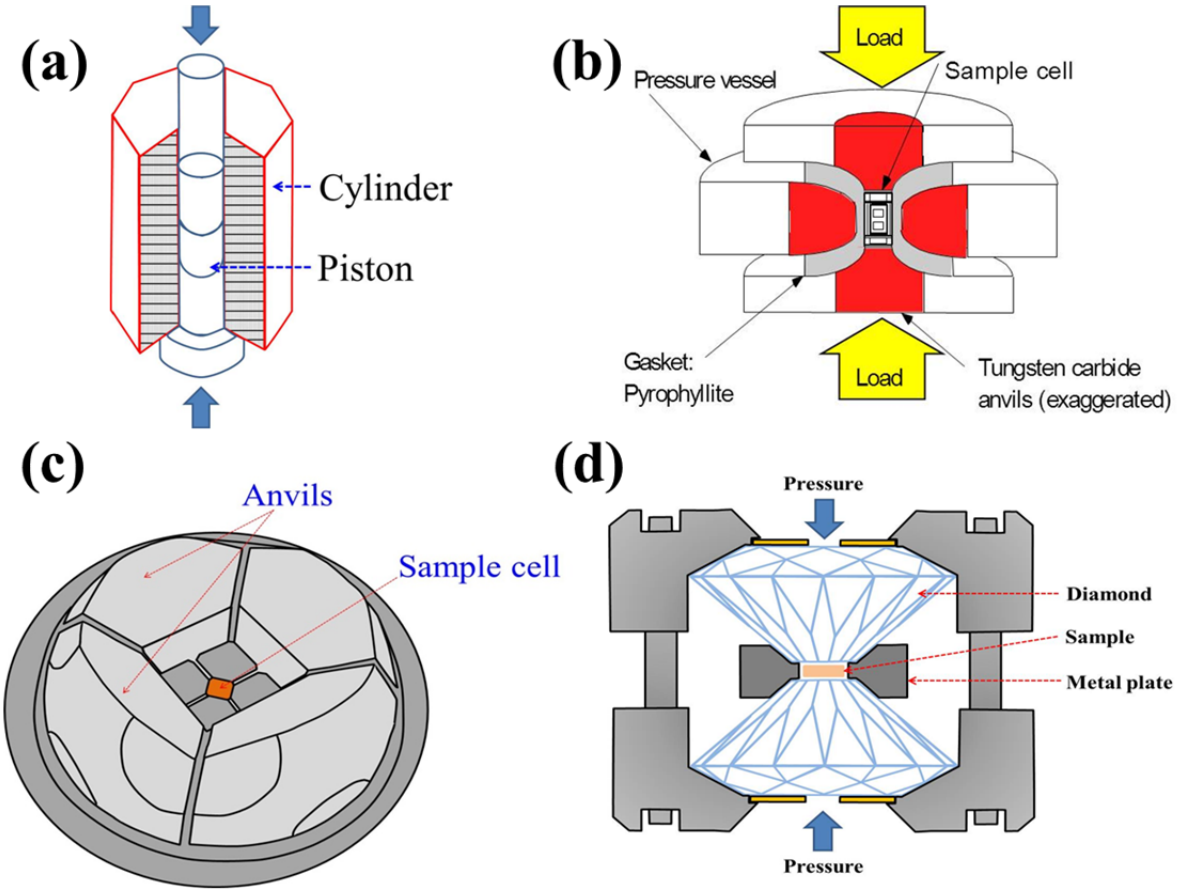

Fig.1.2.1. Different types of high-pressure apparatus (a) piston-cylinder (b) belt-type (c) kawai-type multi-anvil and (d) diamond anvil (extracted from Ref.30).

1.3 Superconductivity in non-oxide materials

It has been passed more than 100 years since the discovery of superconductivity by Dutch physicist Heike Kamerlingh Onnes [2]. So far many classes of superconductors are known like Copper oxide based (CBS), Fe-based high T_c superconductors, Heavy fermion superconductors and BiS_2 layered based superconductors etc. All these superconductors are sub classified into oxide and non-oxide superconductors based on anion and cation which combines to form superconducting layers that induce superconductivity. This thesis focuses on non-oxide materials and a short history of it is as follows. In early 1950's Bernd Matthias, discovered a new class of superconductors by combining ferromagnetic and semiconducting elements $CoSi_2$ with a T_c of 1.33K [39]. Matthias proposed certain rule for finding new

classes of superconductors and it says transition metals are better than simple metals, Peaks of density at Fermi levels are good, High crystallographic symmetry is good, Cubic is best and they stay away from oxygen, magnetism and insulating phases. These rules are very helpful for designing new conventional and metallic superconductors, but it did not clearly lead us to discover new families of unconventional and high temperature superconductors [40]. Soon after John Hulm and G.Hardy reported A15 family of superconductors, which were the first to exhibit high critical currents in the presence of strong applied magnetic field [41]. In 1960's superconducting alloy with Nb:Ti with a T_c of 9.5K was reported and it can remain superconducting in fields as high as 14 tesla [42]. A new class of heavy fermion superconductors was discovered in 1979, which have an antiferromagnetic ground state with rare earth as part of crystal system [43]. The study of heavy fermion superconductors has turned out to be extremely fruitful for materials physics. The 115 family was reported and it shows these new heavy fermion superconductors are quantum critical, [44, 45]. G. Bednorz and A. Muller in 1986 discovered high T_c copper oxides by ambient-pressure synthesis conditions [5] and increase in transition temperature (T_c) was also reported later [46]. In the meantime non-oxide perovskite superconductor $MgCNi_3$ was also discovered by He *et al* [47] followed by Magnesium boride with a T_c of 39K [48]. Soon after the discovery of Fe-based superconductors in 2008 [35, 36], several Fe-chalcogenide systems were also reported [37]. Some of them were synthesized using the solid-state reaction method, and most of the new phases with different stoichiometry were tried using high-pressure and high-temperature synthesis that provided new routes for synthesizing new phases of materials in the field of superconductivity. In this thesis I have focused mainly on three different series of materials as shown below:

1. Transition Metal carbide
2. Layered Bismuth sulfide materials
3. Heavy fermion iron-silicide

I have gathered enough details about the superconductive nature and intrinsic properties of non-oxide transition carbide systems like MoC (molybdenum carbide) followed by the nature of superconductivity in newly discovered BiS_2 layered $Bi_4O_4S_3$ and $LaO_{1-x}F_xBiS_2$ materials and whether substitution can induce superconductivity to magnetic heavy fermion iron silicide systems like $A_2Fe_3Si_5$, AFe_2Si_2 (where A= Rare earth elements). For successive synthesis of these phases high-pressure synthesis methods play a major role.

1.3.1 Crystal structure and superconductivity in Molybdenum carbide

Transition metal carbides and nitrides are well known systems that are studied extensively due to their unique properties and technological applications. The chemical and physical properties include their refractory hardness, thermal stability, corrosion resistance, poisoning resistance, surface reactivity and unique superconducting nature. In addition, they have interesting optical, electronic and magnetic properties and have been used for optical coatings, electrical contacts, diffusion barriers and other uses [49-68]. There are a number of metal carbide phases known from transition metals, but only a few of them are thermodynamically stable, from group IV to VI of the periodic table. Most of the transition metal carbides with 11 phases are cubic in nature where metallic (Mo) and non-metallic (C) atoms occupies face centered cubic lattice and interstitial positions respectively forming a NaCl like structure. But in some cases transition metal carbides crystallize in different phases like hexagonal, orthorhombic etc. Molybdenum carbide is one of the best examples of such type with different phases; Table 1.3.1 gives detailed information of six phases of MoC identified so far.

Table 1.3.1 Structure and stacking sequence of six Mo-C phases

Phase	Structure	Stacking sequence
α-Mo_2C	Orthorhombic	*ABAB*
β-Mo_2C	Hexagonal	*ABAB*
η-MoC_{1-x}	Hexagonal	*ABCACB*
δ-MoC_{1-x}	Cubic	*ABCABC*
γ-MoC	Hexagonal	*AAAA*
γ'-MoC_{1-x}	Hexagonal	*AABB*

Carbon atoms show some order and disorder transformations that contribute the formation of different phases in MoC systems [69]. Due to its advantages molybdenum carbide systems are extensively studied. The final form of the phase diagram is plotted as shown in Fig 1.2.1, extracted from effect of temperature and composition against stability of different MoC phases [70-77]. There are many reports about phase diagram of these carbide phases, but the common fact is that only hexagonal sub-carbides β-Mo_2C and γ-MoC are thermodynamically stable and can be prepared at room temperature. While other two phases

η-MoC_{1-x} and δ-MoC_{1-x} are stable only at high temperatures and high pressures. From the phase diagram we can note that most of the carbide phases show a wide composition range varying from 0.45 to 0.95% of carbon. But, in case of δ-MoC phase, it shows only a narrow composition versus temperature ranging from δ-$MoC_{0.66}$ to δ-$MoC_{0.75}$, because synthesizing stoichiometric amount of 1:1 δ-MoC phase is very difficult under normal conditions. It's very clear from Fig 1.3.1 that, only experimental phase diagram shows stable conditions but other phases and compositions can only be synthesized as meta-stable phases.

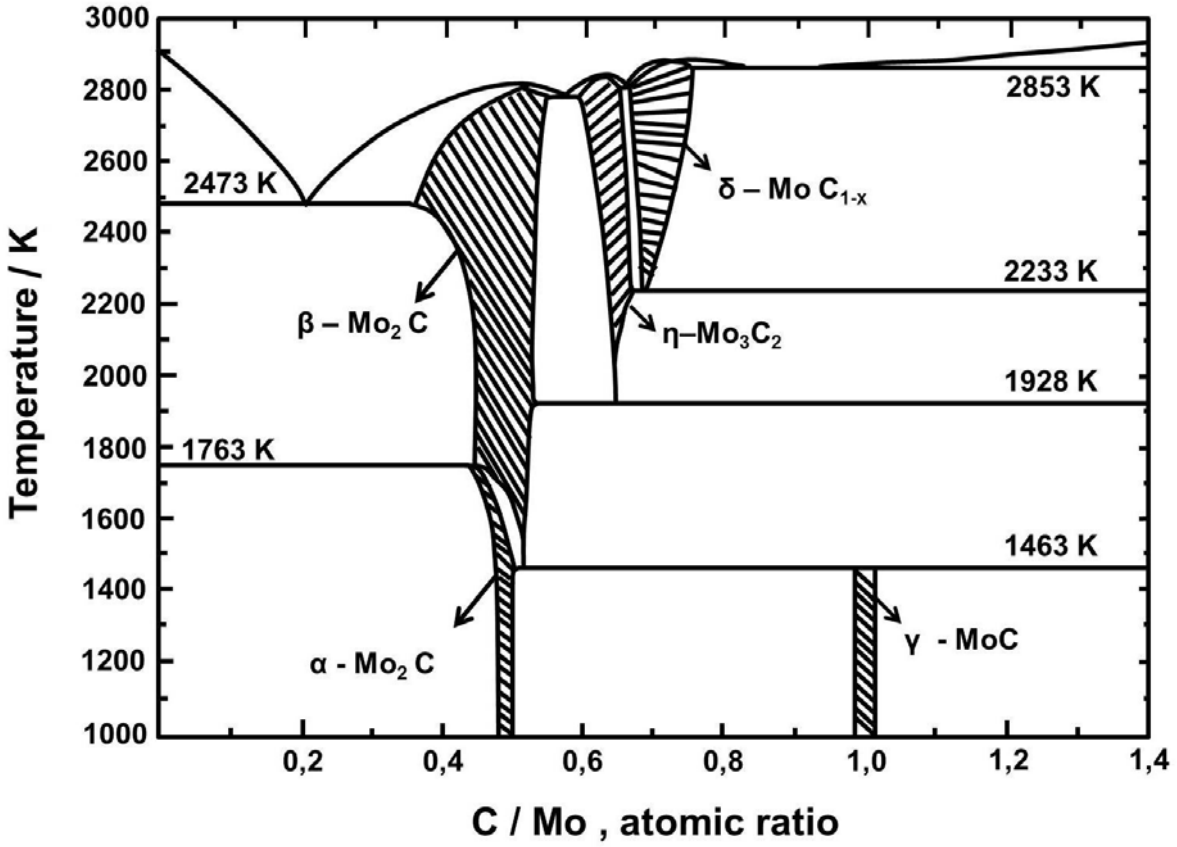

Fig.1.3.1. Phase diagram of Mo-C system under ambient pressure condition (extracted from Ref.74).

There are many theoretical predictions carried out regarding stoichiometry of these carbide phases, where vacancies present contributes to symmetry changes in these structures. Geometric structures of some stoichiometric phases are shown in Fig.1.3.2. The γ phase has a hexagonal structure and isostructural to WC phase where γ′ & η are hexagonal phases. The fourth structure δ is simple like the well-known structure of NaCl with an fcc Bravais lattice. Stoichiometric amount of δ $MoC_{0.75}$ is the only stiffest phase among all four phases, followed by γ and γ′. Density of states is an important parameter to understand more about the bonding and electronic structure of a compound. The electronic structure of above

mentioned phases is studied and theoretical predictions are reported earlier. It has been reported that these phases are not stoichiometric and they exist over a wide concentration range. In transition metal carbide systems carbon atoms are more localized and are closer to the atoms due to bonding charges and the case is different in nitrides. Because the bound charges for nitrides are easily distorted than transition metal carbides with covalent bonding charge. Mono carbides are unstable that has ten or more electrons with a NaCl type structure, and that gets phase transition easily to a thermodynamically stable phase could be expected. Jhi *et al,* [78] reported in his first pseudopotential method that mechanical properties of transition metal carbides are influenced by vacancies and those vacancies results to harden host matrix. On the other hand bonding properties also initiates particular macroscopic behaviours that can lead to instabilities that prevent structure formation in stoichiometric ratios.

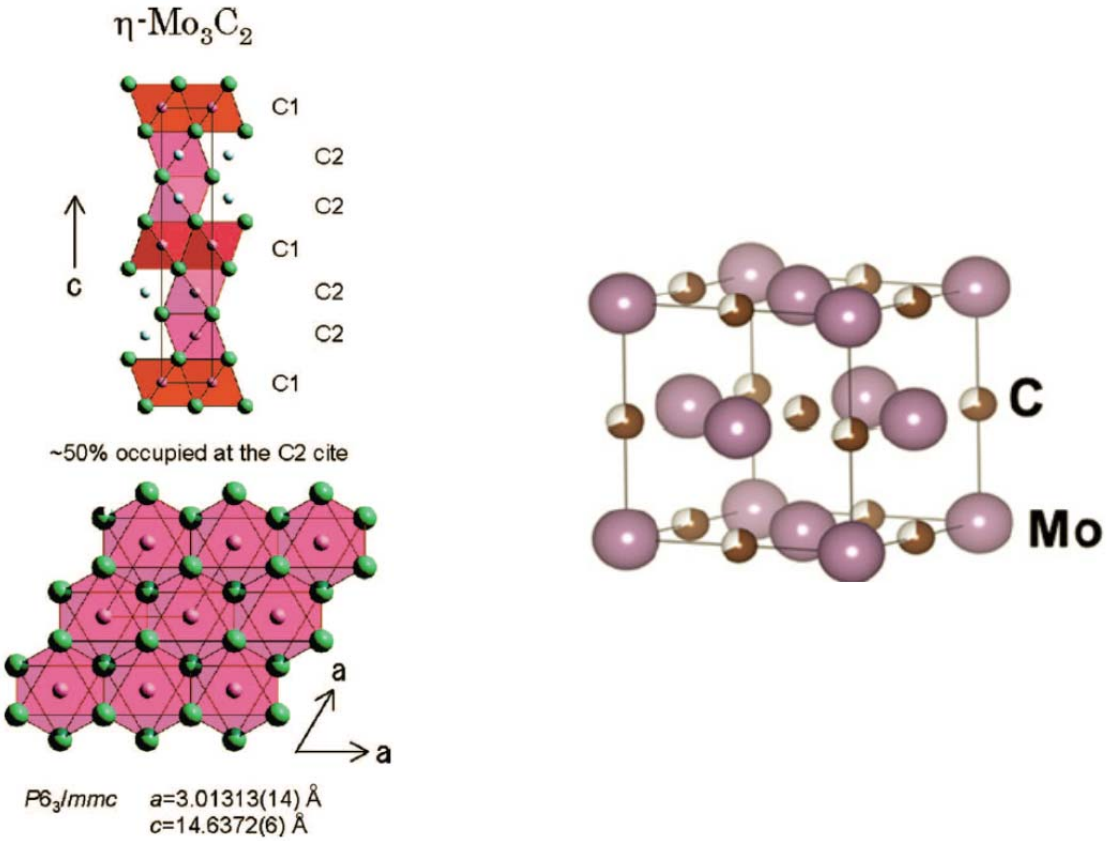

Fig.1.3.2. Pictorial view of Mo_3C_2 phase and MoC (extracted from Ref.79 & 80).

Density of state (DOS) profile for different carbides and nitrides of Zr, Nb and Mo are very similar, but there is a systematic increase of DOS at Fermi level. From lattice constants and bulk moduli the same systematic movements can be noticed. Molybdenum carbides and nitrides are proposed to be good applicant that can show high T_c was projected

from a regular increase in the density of states at Fermi level $N(E_F)$ [81-83]. Superconducting transition temperatures of different carbides and nitrides are very low than expected which was predicted from DOS arguments using quantitative muffin-tin calculations [84]. Were β-Mo_2C and γ-MoC phases showing T_c around 2.8K and 8.3K while η-MoC_{1-x}, δ-MoC_{1-x} T_c is around 8.9K and 14.3K. As the stability of MoC is weaker than MoN it's estimated that T_c will be smaller than predicted [85]. Calculations of elastic constants predicts MoC is a stable phase, but the mystery is stoichiometric MoC with B1 structure has never been synthesized. To know about the key point behind this nature, phonon frequency of MoC phase at some selected points from Brillouin zone was estimated. Phonon frequency at Γ point shows, there is no indication of phonon anomaly and was well comparable with the phonon frequency of NbC [86-88, 90]. In the case of NbC anomalous region becomes more pronounced and shifts toward *X* point was noted from phonon spectra, though NbC phase is very stable and synthesized at normal conditions. As phonon spectra of these carbides follow same systematic trends like lattice constants, bulk moduli and $N(E_F)$ it's more clear that phonon anomaly of MoC becomes more prominent and in some cases phonon modes become unstable and structure gets distorted at particular temperatures. Some report regarding phonon instabilities in MoC indicate that if studies are extended to *BZ* region we can find some anomaly near point *X* [89, 90]. Schematic view of phonon spectrum for B1 type MoC and MoN along Brillouin zone is shown in Fig.1.3.3.

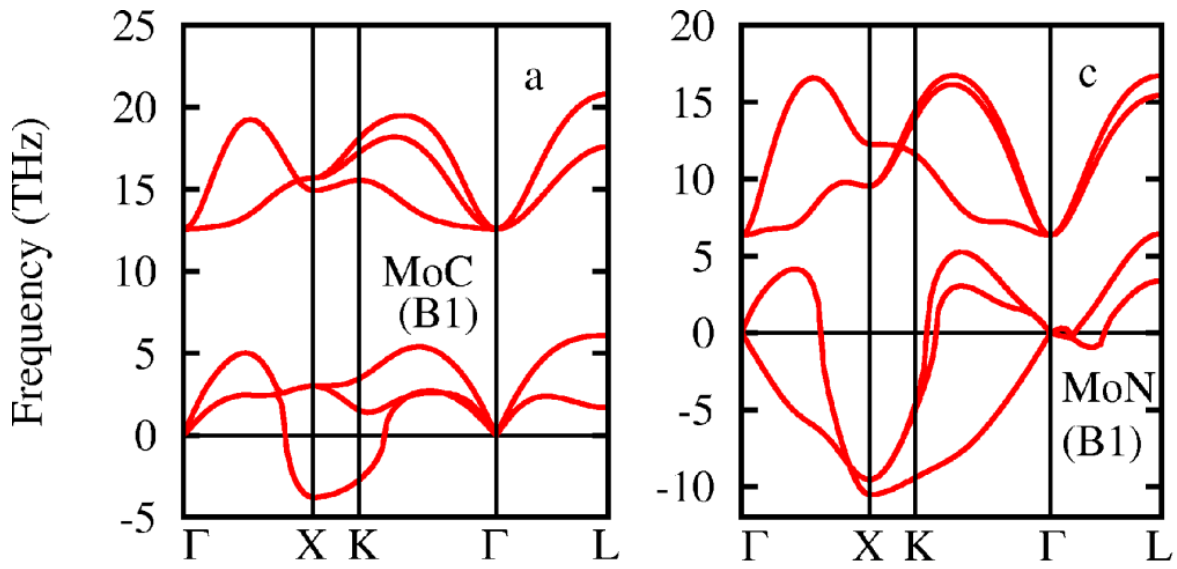

Fig.1.3.3. Phonon spectrum for B1 Molybdenum carbides and nitrides in Brillouin zone (extracted from Ref. 90)

Frequency calculations at point *X* for MoC indicate half of optical longitudinal phonons as in NbC and acoustic longitudinal phonons are unstable at point *X*. This was comparable with the previous reports on elastic constants of MoC that has high stable elasticity. While, near *X* points Fermi surfaces of MoC and MoN shows indications of nesting effect and not as in NbC and TaC [91, 92]. So synthesizing high quality crystals of MoC is unsuccessful and this instability is due to extreme phonon softening near *X* point. In addition, it has been reported that MoC and MoN can never be synthesized experimentally and the properties of this phase have never been studied [90]. As mentioned above there are numerous difficulties in preparing non-oxide δ-MoC and studying the properties of this material in detail. The main aim of this thesis is to investigate a detailed study on δ-MoC by synthesizing stoichiometric B1 stable phase using high-pressure and high-temperature synthesis and to extract the intrinsic properties like electrical and thermal transport in detail.

1.3.2 Bismuth-sulfide based chalcogenide systems

Layered materials that show superconducting properties provide great interest in the field of physics due to its attractive electronic and magnetic properties. They are two dimensional crystal structured materials and unusual superconductivity is favored due to this nature. A series of layered superconductors starting from cuprates, Fe-based and Magnesium diborate belongs to this series [93-106]. Chalcogenide systems are important layered superconducting materials that attract researchers due to their unique structure and properties. Some of these materials show existence of both magnetism and superconductivity, while some of them are insulators. In 1970,'s a series of transition metal chalcogenide systems were reported and found a base for a new group of materials. Transition metals react with chalcogenide like sulfur, selenium and tellurium to form compounds with a layered crystal structure like that of graphite, with the general formula MX_2 where, M is a metal and X is a chalcogen [107-109]. The most extensively studied transition metal dichalcogenide's are the disulfides and diselenides of group IV-B metals Ti, Zr, Hf, group V-B metals like V, Nb, Ta and group VI-B metals Mo, W. Some other stoichiometric ratios are also possible in these systems like tri-selenides $NbSe_3$ and $TaSe_3$ that are interesting quasi one-dimensional materials [110, 111]. The basic crystal structure of these systems is composed of three atom-stick, covalently bonded layers with only weak van der Waals-type interlayer bonding. Each individual layer is made of three hexagonally close packed planes. They stack in two different ways in ABA sequence or the ABC sequence. The ABA sequence forms a trigonal prismatic

coordination of metal atoms using six nearest chalcogen atoms, while the ABC sequence tends to form an octahedral coordination. After a long break in the development of chalcogenide superconductors in 2008, Hsu *et al* [37], reported the superconductive nature in anti-PbO type FeSe chalcogenide with a T_c of 8K that attracted superconductive research in chalcogenide systems. Very soon, systems like FeS, FeSe and FeTe was reported [112-116], The superconducting transition in FeSe increased dramatically to 37K by synthesizing under high pressure [117] and recent reports by K added FeSe system with excess of Fe, where the T_c raised to 44K [118]. FeTe system by substitution of Se/S for Te induced superconductivity by suppressing antiferromagnetic transition. Apart from this $TiSe_2$ which has a simple layered structure [119, 120] but Bi_2Se_3 a well-known topological insulator that has layered type structure [121, 122]. Some of the chalcogenide systems are shown in Fig.1.3.4. As these chalcogenide systems contain a simple layered structure with van der Waals gap, external ions can be easily added to the interlayer sites that can change physical properties.

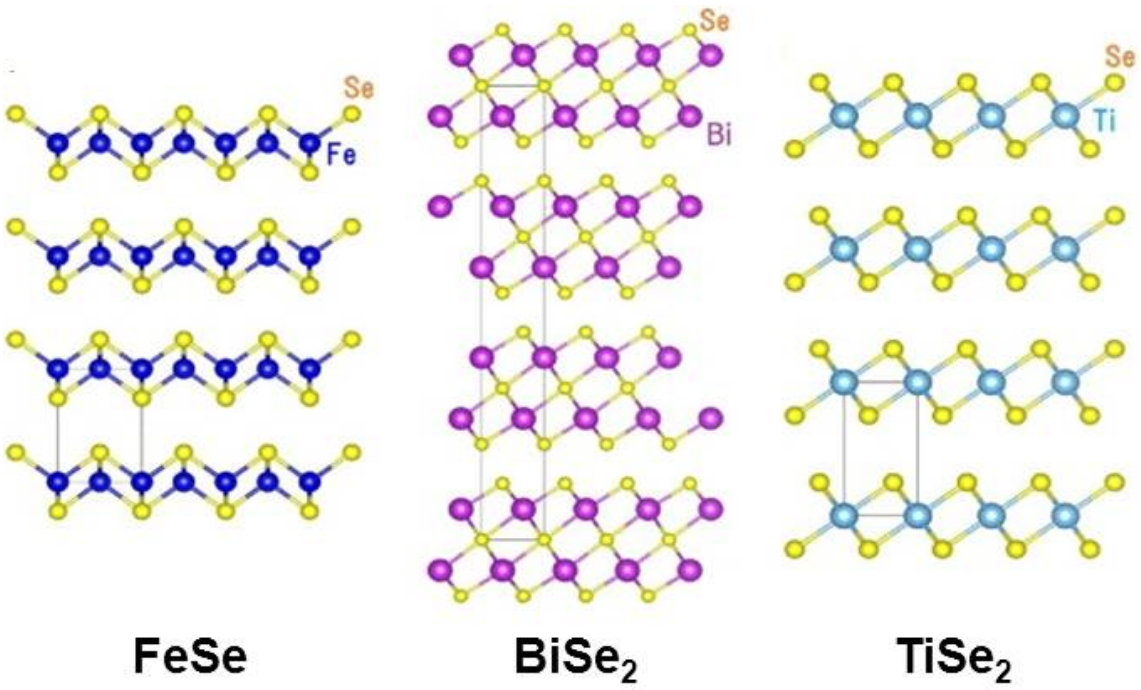

Fig.1.3.4. Crystal structure of typical calcogenides FeSe, $TiSe_2$ and $BiSe_2$ (extracted from Ref.131).

Very recently Mizuguchi *et al,* reported a new family of superconductors with bismuth oxy-sulfide layered $Bi_4O_4S_3$ system [123-126], with a low temperature transition of 4.5K. This consists of layered BiS_2 planes as that of layered CuO_2 planes and Fe-based high T_c superconducting materials. It was reported that it consists of a sequence of rock-salt type

BiS_2 layers and $Bi_4O_4(SO_4)_{1-x}$ layers (blocks), where x indicates lack of SO_4^{2-} ions at the interlayer sites. The parent phase (x = 0) is $Bi_6O_8S_5$ and $Bi_4O_4S_3$ corresponds to the x = 0.5 and these defects at the interlayer sites are common for layered materials. From the band calculations, also they report that $Bi_4O_4S_3$ (x = 0.5) is a metal whereas the parent phase of $Bi_6O_8S_5$ (x = 0) is a band insulator that contains Bi^{3+} ions. Soon after another superconducting BiS_2 layered material $REO_{1-x}F_xBiS_2$ (RE- rare earth) was also reported. These systems are $LaO_{1-x}F_xBiS_2$, $NdO_{1-x}F_xBiS_2$, $CeO_{1-x}F_xBiS_2$ and $PrO_{1-x}F_xBiS_2$ [127-1130], where the superconducting transition differs between 2.7 to 5.6K was reported. [131]. However, a clear picture, of superconducting nature in this, a series of materials is unknown and no clear evidence of superconductivity was confirmed. Therefore, my aim as a part of this thesis was to prepare these materials using high-pressure technique and to study their electric, magnetic, thermal properties of this system and also to know the exact reason for the occurrence of superconducting nature.

1.3.3 Structure and properties of Fe-based systems

Discovery of superconductivity in $La(O_{1-x}F_x)FeAs$ layered iron based superconductor with relatively high transition temperature by Hideo Hosono and his group members in 2008 [35], lead researchers a great breakthrough and new high T_c Fe-based superconductors family raised. After this invention, researchers were interested in developing new superconducting materials other than High-T_c CuO-layered superconducting materials. So far, there are many reports on iron pnicitide superconducting systems and yet clear mechanisms about superconducting nature in these series are largely un explored. The highest T_c ever achieved so far in Fe-based series is ~56K [132, 133]. The Major importance of Fe based materials is synthesizing these materials at high-pressure and high-temperature (*HPHT*) method is highly efficient than solid state reaction methods. Because $LnFeAsO_{1-x}F_x$ (Where Ln = rare earth) type materials release gas while heating in a sealed tube and fluorine loss can be observed. Short sintering time and maintaining sample in capsules are the major advantages when synthesizing under *HPHT* method. Also *HPHT* prepared samples show small unit cell constants and lattice parameters with high-T_c that favor them from other methods. There are several good motives why these Fe based superconductors are so interesting, because they have motivating physics like the coexistence of superconductivity and magnetism. They provide different series of compounds with their multi-band electronic structure that offers hope for discovering the mechanism behind high temperature

superconductivity and finding ways to increase T_c. Iron based superconductors have good application importance due to their high H_{c2} values than cuprates and high isotropic critical currents [134-137] and highly applicable in electrical power and magnetic applications. The coexistence of superconductivity and magnetism makes them interesting in the field of spintronics [138]. Many families of Fe-based superconductors and magnetic materials are known with different structures. There are four different classes of iron based materials according to their structures. They are,

1. 111 type LiFeAs with tetragonal *P*4/*nmm* space group and PbFCl type structure.
2. 1111 type LnFeAsO (Ln-lanthanides) with tetragonal *P*4/*nmm* space group and ZrCuSiAs type structure.
3. 122 type $BaFe_2As_2$ with tetragonal I4/mmm space group and $ThCr_2Si_2$ type structure.
4. 11 type FeSe with tetragonal *P*4/*nmm* space group and PbO type structure.

Crystal structures of 1111, 111, 122, 11 phases of Fe-based materials are shown in Fig 1.3.5.

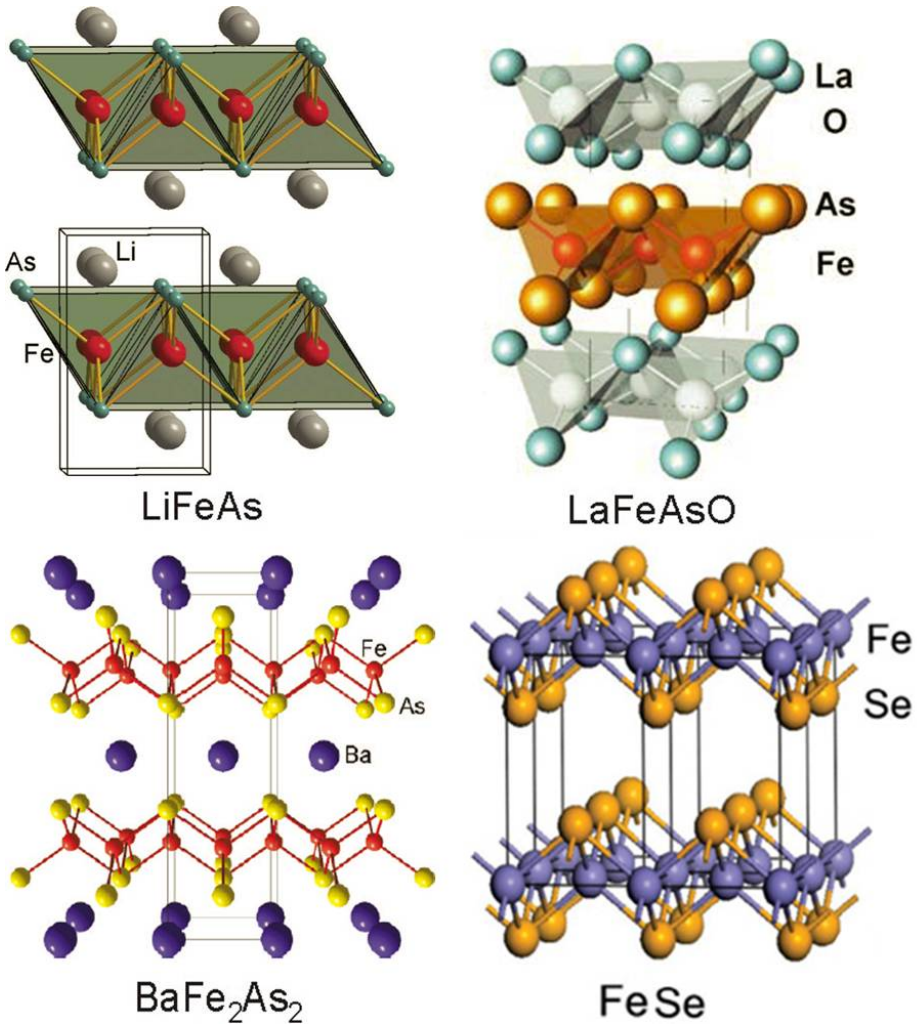

Fig.1.3.5. Crystal structures of 111, 1111, 122, 11 phases of Fe-based materials (extracted from Ref.139-141 and 37).

From band structure calculations there are two electron and hole pockets on Fermi surface which was explained by two band model [142]. Where these compounds show similar electronic band structure and electronic states at Fermi level which are occupied mostly by Fe 3*d* electrons. Structure of these compounds is complex and due to the presence of five conduction bands it shows complex Fermi levels. Doping to these compounds leads to many unusual superconducting and normal state properties. It is reported that Fe based 122 systems have electron like Fermi surface which doesn't show superconducting nature [143]. In the case of 122 compounds there is a wide range of physical phenomenons like magnetic phase transitions, various types of magnetic ordering, heavy fermions, crystal field effects, mixed rare earth ions and superconductivity. The research done by me is mainly focused on Ternary Fe-Si systems $M_xT_ySi_z$ where M is a rare earth element and T a transition metal. These ternary silicide systems forms complicated structure and show mixed phases with complex properties. While in binary Fe-based systems like 122 phases, at particular temperature and pressure, each phase will be in equilibrium with at least two of its neighboring phases and this number may be large in ternary systems. Single phase of ternary Fe-Si systems are very difficult to synthesize, because they show mixed phases by due course of time. Hence, to prove the physical properties are intrinsic to a given phase or it is from an impurity contribution considerable numbers of neighboring phases are tested in a ternary system. Some of the ternary silicide systems contain more than one superconducting phase, and if it is a magnetic material, it shows two transition temperatures in the same compound is also common in these types of complex systems. Much attention has been given to focus on the competition between superconductivity and magnetism observed in several rare-earth compounds [144].

Even if there is an absence of superconductivity the nature of magnetic order in many of these systems are still lacking. The recent discovery of superconductivity and magnetism in $M_2Fe_3Si_5$ compounds [145-149] represents coexistence of superconductivity and magnetic properties that strongly depend on the choice of rare earth materials. In many of these ternary intermetallic systems, hybridization between localized *f*-electrons of rare earth elements and itinerant conduction *d*-electrons supplied by surrounding atoms leads to extraordinary physical phenomena. Due to this many ternary systems were synthesized with different compositions and shows a variety of appealing physical property behavior including superconductivity and coexistence of magnetism and superconductivity along with valance fluctuations , kondo effect and large positive magneto resistance and some of these have large

Sommerfeld coefficient (γ) of electronic specific heat. Some of the ternary systems like $Ce_2Rh_3Sn_5$ and $Yb_2Fe_3Si_5$ are moderate heavy fermion systems with mixed-valance behavior and $Yb_2Fe_3Si_5$ is a kondo lattice system and a heavy fermion with γ ~500 $mJmol^{-1}K^{-2}$ [150]. High-pressure synthesis has helped to develop good superconducting materials like the Tm and Lu systems in ternary silicides at low temperatures [151-154]. Substitution and doping may be possible to increase the T_c in these compounds, but there are no reports on doping or substitution of electrons or holes in these systems due to synthesizing difficulties. Therefore, my aim as part of this thesis is to successfully synthesizing these compounds by high pressure and to carry out a detailed study on this system by substitution or doping.

1.4 Basic characteristics of superconductivity

To know more about superconductors certain basic characteristics features should be known. Before describing as superconducting sample first we should identify the type of superconductivity whether it's *Type-I* or *II* superconductors and parameters like Superconducting transition temperature, upper critical field, lower critical field, penetration depth, coherence length, etc. are to be known. Here in below units we explain some of the basics in detail.

1.4.1 Type-I and Type-II Superconductors

In superconducting materials when high magnetic fields are applied, they have the ability to exist either in normal state or superconducting state. Based on it, they are classified into two types. When a superconductor is placed in external magnetic field *H*, if we increase the magnetic field superconducting transition (T_c) starts to decrease. Superconducting nature gets vanished if external magnetic field exceeds critical field, H_c and that material behaves as if a normal conductor. This behaviour occurs when magnetic flux gets penetrated through the material, for example pure metals like lead, niobium, tin etc. shows such kind of behaviour at low temperature. Such superconductor that goes from superconducting state to normal state above a critical magnetic field H_c is known as *Type-I* superconductors. When temperature dependent magnetic field measurements are carried out amount of critical magnetic field H_c varies in *Type-I* superconductor. Schematic view of *Type-I* superconductor in the presence of applied magnetic field is shown in Fig.1.4.1. For a *Type-I* superconductor H_c is mathematically expressed as,

$$H_c(T) = H_C(0)\left[1 - \left(\frac{T}{T_c}\right)^2\right] \qquad (1.1)$$

Where $H_c(0)$ is the value of critical field at absolute zero.

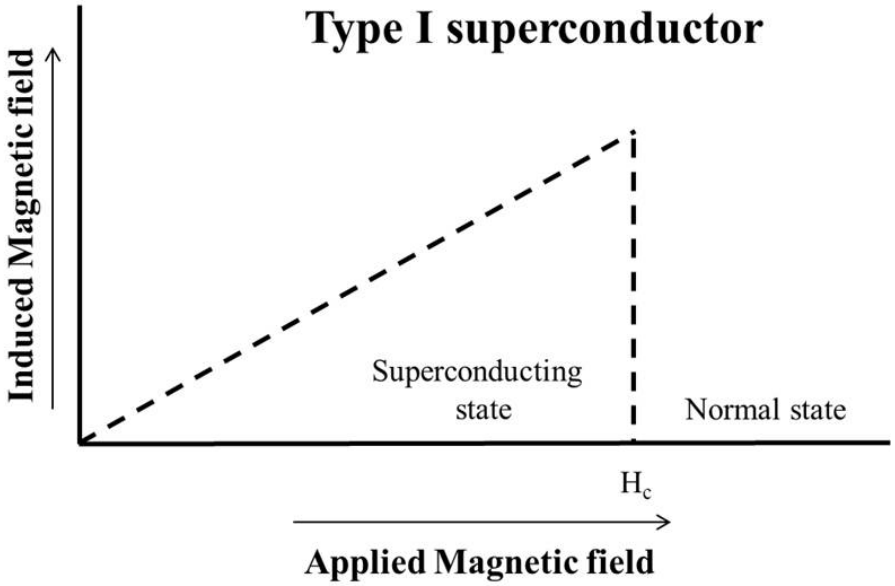

Fig.1.4.1. *Type –I* superconductors in the presence of an external magnetic field (extracted from Ref. 155)

In a superconductor when applied magnetic field is lesser than critical field H_{c1} then the material is in highly superconducting state and there is no magnetic flux penetration. But when applied magnetic field pierces into the sample and exceeds upper critical field H_{c2},

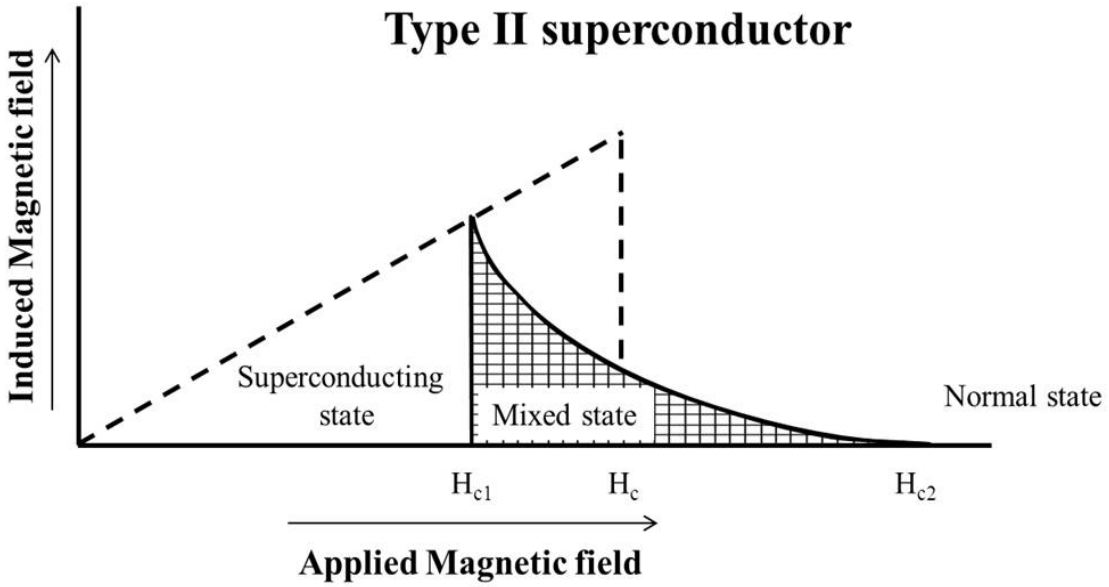

Fig.1.4.2. Type-*II* superconductors in the presence of an external magnetic field (extracted from Ref.155)

magnetic flux gets pierced completely and superconducting nature destroys completely. Area between H_{c1} and H_{c2} is in a *mixed state* and mentioned as *vortex state*. When superconducting materials are in a mixed state it shows zero resistance and restricted flux penetration but if we further increase applied field, materials turn to normal conducting state. High-T_c materials like Fe based and CuO based materials belong to *Type II* superconductors. Schematic view of *Type-II* superconductor in the presence of an applied magnetic field is shown in Fig.1.4.2.

In addition a Type-II superconductor has both lower and upper critical fields H_{c1} and H_{c2} respectively, which is mathematically expressed as,

$$H_{c1} = \frac{\Phi_0 \ln \kappa}{4\pi\lambda^2} \qquad (1.2)$$

$$H_{c2} = \frac{\Phi_0}{2\pi\xi^2} \qquad (1.3)$$

If applied magnetic field flow perpendicular through the surface of a superconductor then it will be actual upper critical field H_{c2}. But if it flows parallel then there will be a thin layer of superconducting nature over the sample until it reaches higher critical field $H_{c3} = 1.69\ H_{c2}$.
Penetration depth (λ) measures depth of external magnetic field that penetrates from the surface of a superconductor. It varies with temperature as given by the expression

$$\lambda(T) = \lambda_0 \left[1 - \left(\frac{T}{T_c}\right)^2\right]^{-1/2} \qquad (1.4)$$

To measure superconducting *coherence length* ξ_{GL} at $T = 0$ it can be estimated from single-band Ginzburg-Landau relation

$$\xi_{GL} = \sqrt{\frac{\phi}{2\pi H_{c2}(0)}} \qquad (1.5)$$

Where ϕ_0 is the flux quantum and $H_{c2}(0)$ is the upper critical field at zero temperature [156]. Both λ and ξ are temperature dependent quantities. Abrikosov explained with an expression from the ratio of $\kappa = \lambda/\xi$ that obeys *Type-I & II* superconductors. If $k < 1/\sqrt{2}$ then such materials will be *Type-I* superconductors and if $k > 1/\sqrt{2}$ it will be *Type-II* superconductors. He also explained that both *Type-I & II* superconductor's shows completely different responses to an applied magnetic field [157]. In case of *Type-I* it completely expels magnetic flux from inside, while *Type-II* does so only in higher applied magnetic fields. Reason for such behaviour in both *Type-I & II* is that, interface between superconductor and normal state is different. Also surface energy is positive for *Type-I* and negative in the case of *Type-II* superconductors. From the two limiting cases $k \ll 1$ and $k \gg 1$, we can know the difference

of *Type-I & II* superconductors. Schematic view of both the cases is shown in Fig.1.4.3 (a) $\lambda << \xi_{GL}$ and (b) $\lambda >> \xi_{GL}$.

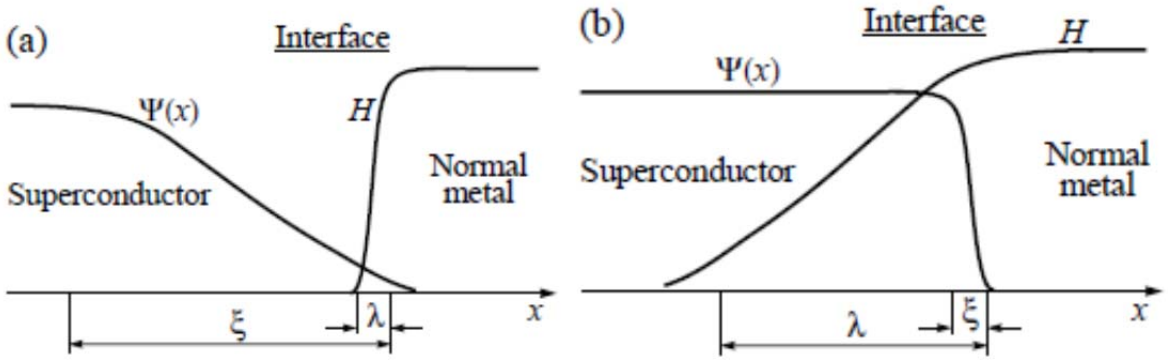

Fig.1.4.3. *O*rder parameter Ψ and magnetic field *H* in the area of superconductor-normal metal boundary at (a) $k << 1$ and (b) $k >> 1$ (extracted from Ref.157).

1.4.2 Bardeen Cooper and Schrieffer (BCS) Theory

In 1957, three scientists J. Bardeen, L. Cooper and R. Schrieffer proposed the first microscopic theory of superconductivity that predicts quantitatively many properties of elemental superconductors, which is known as *BCS theory* [158]. It successively explains about the fundamental mechanism of superconductors for low T_c metals and alloys. BCS theory explains three points regarding the nature of superconductivity. It does not concentrate on any interactions, but for the formation of Cooper pair's phonons play an important role, and compares the predictions formulated from theories with that of experimental results. Predictions of this theory mainly focused on similarities of electron-electron, electron-phonon interactions and pairing of s-wave vectors [159]. When an electron travels in a lattice it polarizes and attracts positive charge ions simultaneously neglecting the negative charged ones. Due to continuous polarization of lattice it follows by attracting another electron and both combines up to form Cooper pairs. The travelling electron can polarize lattice, attract the positively charged ions, and repel the negatively charged ions. As such, the polarization in lattice is continued by attracting a second approaching electron, and both electrons couples to form pairs. Schematic view of Cooper pair formation is presented in Fig.1.4.4. Columbic repulsion would be very week between the two electrons because before second electron reaching first electron it travels away to farer distance. When comparing freely conducting electrons and coupled electrons the mean distance for coupled electrons will be comparably too large. BCS theory successfully explains certain factors, like it shows a second order phase

transition. There exists an energy gap 2Δ which is highest at lower temperatures and that decreases simultaneously to zero at T_c can be detected by electronic excitation spectrum. It largely supports Meissner effect, specific heat and resistivity at zero temperatures.

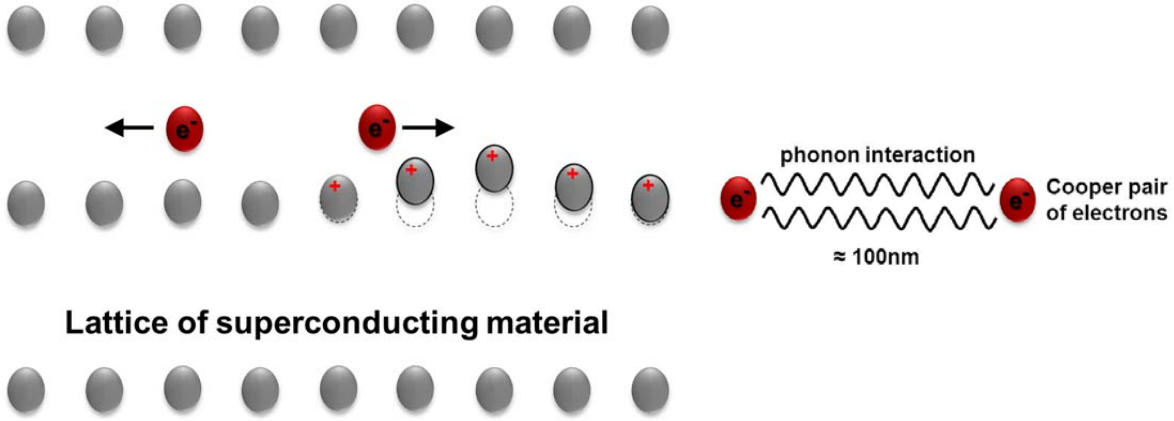

Fig.1.4.4. Schematic of Cooper pair formation (extracted from Ref.160)

1.4.3 Specific heat

The thermal properties of superconductors have been extensively studied and specific heat is one very important measurement to differentiate superconductor's bulk property. When normal metal is applied by a small amount of thermal energy, some energy is used to motivate lattice vibrations and the remaining is used to increase the kinetic energy of conduction electrons. The specific heat behavior of a superconductor is like that of a normal metal that contributes electrons (C_e) and lattice (C_g). For the normal metals at low temperatures it can be expressed as,

$$C_n = C_{en} + C_{gn} = \gamma T + A(T/\Theta)^3 \qquad (1.6)$$

Where γ is Sommerfeld constant, which is proportional to density of electronic states at the Fermi surface, Θ is Debye temperature and A is a numerical constant for all metals. The two contributions for normal phase can be separated experimentally by plotting C_n/T vs. T^2, so that the slope of the resulting curve is A/Θ^3, and the intercept is γ.

So, in superconducting phase

$$C_s = C_{es} + C_{gs} \qquad (1.7)$$

Fig.1.4.5 shows superconducting jump in Gallium metal and values of both superconducting (H=0) and normal phase ($H \geq H_c$) shows a sharp jump in superconducting phase of the order of 2 γT_c at T_c and a rapid decrease of specific heat in superconducting phase to values below

normal phase varies about as T^3. It is very difficult to understand the difference between superconducting phase and normal phase entirely because, change in electronic contribution is assumed to be as same in that of lattice contribution. This seems to be reasonable in view of electronic nature in superconductors and is supported by the absence of any observable changes in lattice contributions thereby detecting any minimal changes in elastic properties. On this assumption

$$C_s - C_n = C_{es} - C_{en} \qquad (1.8)$$

From this, we can determine the electronic contribution of superconducting phase from measured values of specific heat difference after $C_{en} = \gamma T$ has been determined separately [161].

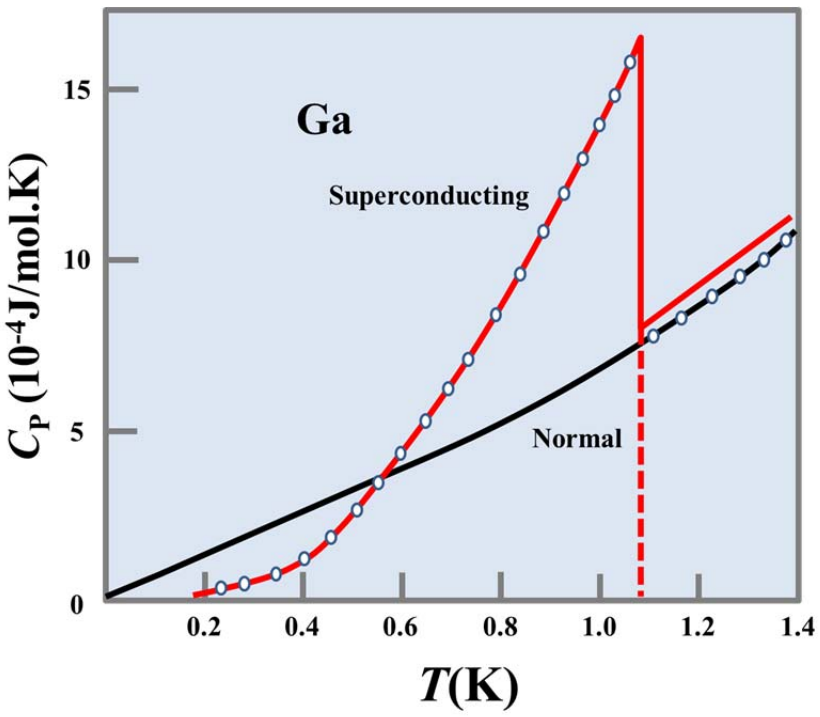

Fig.1.4.5. Specific heat vs. Temperature of superconducting Gallium (extracted from Ref.159).

1.5 Fundamentals of Magnetism

Magnetism is a phenomenon by which materials can attract or repulse each other which is known for thousands of years earlier from the use of feeble permanent magnets in forms of lodestones. Ancient Greece and Chinese said these lodestones align in longitudinal directions which later lead to the first usage of magnets in creating compass. After long years

Pierre de Maricourt discovered in 1263 that magnets have two poles North and South Pole. Later William Gilbert who was a physician under Queen Elizabeth in 1600 reported that earth itself is a giant magnet. Danish physicist Hans Christian Orsted later in 1820 discovered that electricity and magnetism are interrelated. Also Michael faraday and Joseph Henry put forth the idea of electric and magnetic fields experimentally which lead to the invention of dynamo which was the first electric motor. In 19th century there was lot of progress like the invention of superconductors, Meissner effect etc. and many theories and predictions with mathematical calculations were put forth. The basic principles and mechanisms behind this is too complex and still the true face behind is unrevealed. Technological growth uses magnetism and magnetic materials to design different devices and instruments. As the need for sources of new materials with high efficiency hunting of materials and fundamental aspects are still going on. All materials contain some kind of magnetic property in it, when such materials are placed in external magnetic field some magnetic moments are noticed and based on that materials can be classified into different types of magnetism, paramagnetic, ferromagnetic, antiferromagnetic, diamagnetic and ferromagnetic respectively.

1.5.1 Diamagnetism

Diamagnetism is a type of magnetism that is very weak, not permanent and it can only exist in an applied magnetic field which was discovered by Michael Faraday in 1845. In diamagnetic materials there is no net magnetic moment if an external field is not applied so they are known as non-magnetic materials. By applying an external magnetic field the electrons gets motion in a direction opposite to applied field and the relative permeability μ_r will be less than one and magnetic susceptibility value would be negative. Superconductors are perfect diamagnets and when they are placed in an external magnetic field gets expelled of (Meissner effect). In most of the cases diamagnetism arises from pairing of electrons and no permanent net magnetic moment per atom. Fig.1.5.1 (a) shows schematic view of a diamagnetic material when there is no field and an external field is applied. The atomic dipole moments are noted by arrows and when an applied magnetic field is induced, the poles are aligned towards opposite side [161]. Theoretically by assuming a linear material and relative permeability $\mu_r \approx 1$ we can write as

$$\chi = \frac{\mu_0 M}{B} \qquad (1.9)$$

Where $M = \chi H$ and $B = \mu_0 H$. So we can rewrite it as,

$$\chi = -\frac{N}{V}\frac{\mu_0 e^2}{6m}\sum_i \langle r_i^2 \rangle \qquad (1.10)$$

From the given equation we can obtain that, susceptibility value would be negative and is indicated as $\chi_{dia} < 0$ and would be independent of temperature [162].

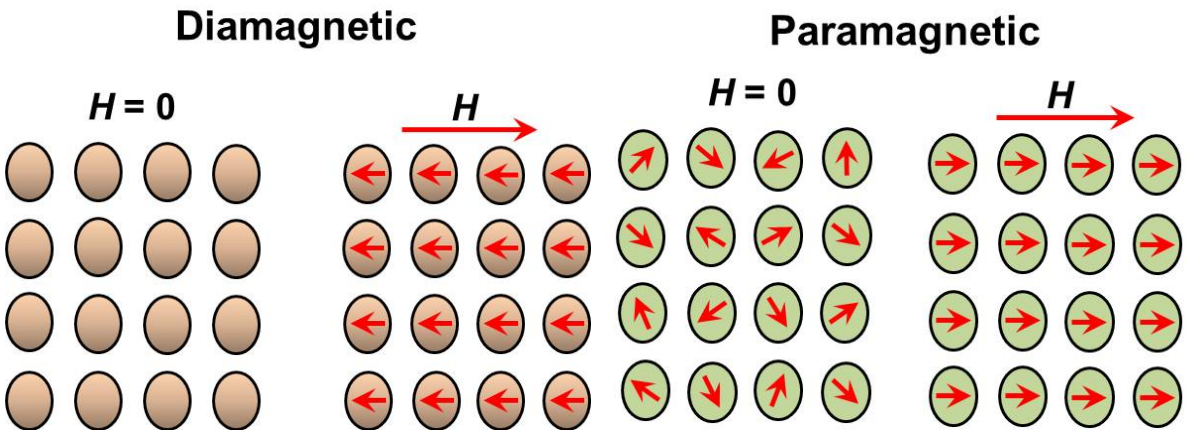

Fig.1.5.1. (*a*) Diamagnetic material with and without magnetic field. (*b*) Paramagnetic material with and without an external magnetic field (extracted from Ref.161).

Temperature dependence of magnetic susceptibility χ for different diamagnetic and paramagnetic materials is schematically shown in Fig.1.5.2, where susceptibility behaviour changes upwards to positive in case of paramagnetic material and it behaves as an insulating or semiconducting like property and shows negative susceptibility with superconducting property in case of diamagnetic materials.

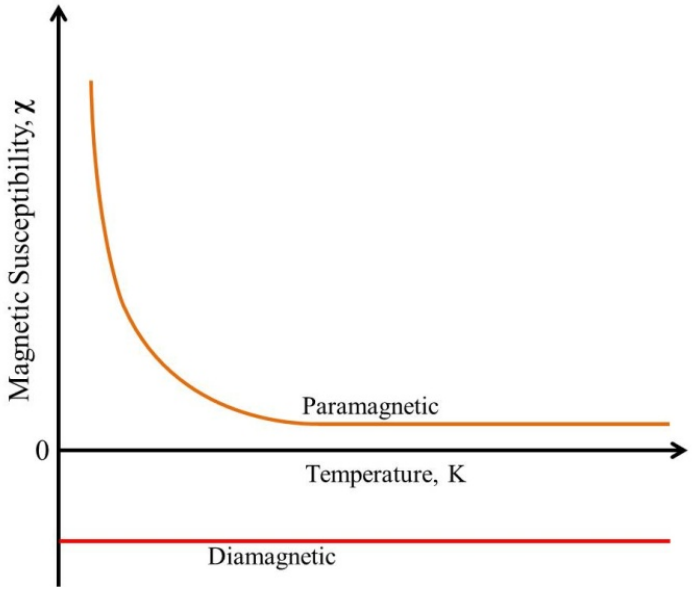

Fig.1.5.2. Temperature dependence of Magnetic susceptibility for paramagnetic and diamagnetic material (extracted from Ref.155).

1.5.2 Paramagnetism

Paramagnetism is a mechanism where atoms or molecules of a substance, which possess a permanent, spin magnetic moment that aligns in the direction of applied magnetic field. If there is an absence of applied magnetic field they orient randomly so that the material doesn't possess any net magnetization. Schematic view of atomic dipole orientation with and without magnetic field is shown in Fig.1.5.1 (b). Magnetic dipole acts as if they are individual and they get isolated from the neighboring dipoles. When an external magnetic field is applied the value of relative permeability μ_r increases and would be greater than one, but when compared with other magnetism it is smaller with positive magnetic susceptibility [161]. The value of susceptibility for paramagnetic materials would be ranging from 10^{-5} to 10^{-2}. As diamagnetic and paramagnetic materials can only exhibit magnetization at any applied magnetic field they are considered to be non-magnetic materials at normal state. Fig.1.5.3 shows the schematic view of *B*-versus-*H* for both paramagnetic and diamagnetic materials, where the flux density *B* would be comparable for both of them under vacuum conditions.

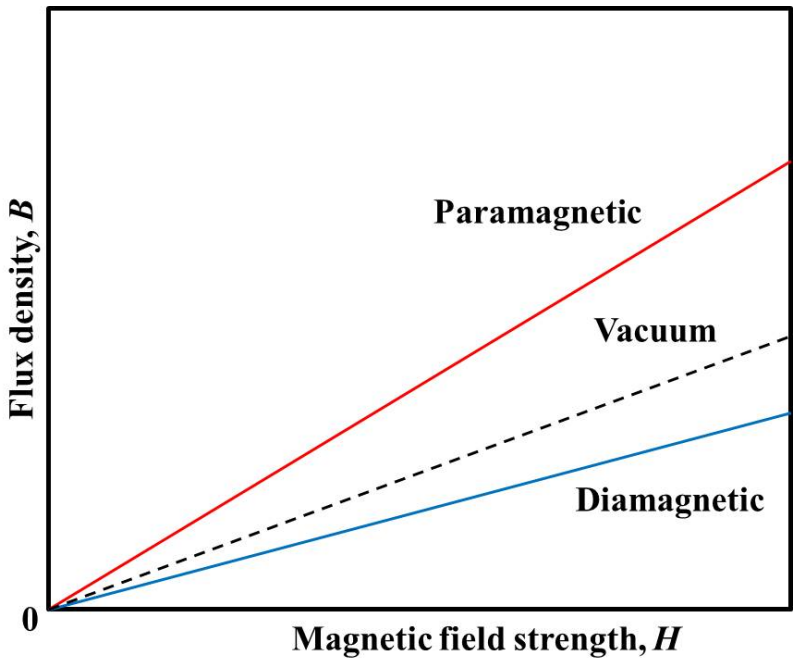

Fig.1.5.3. Schematic view of flux density *B* versus magnetic field strength *H* of diamagnetic and paramagnetic materials (extracted from Ref.161).

In order to know the magnetic susceptibility of a paramagnetic material we should calculate the number of magnetic dipole moments that align parallel by applying an

external magnetic field. The magnetic dipole moments that occur in paramagnetic materials are due to electron spinning without interacting with each other. Paramagnetism that arises in all atoms and molecules are due to unpaired electrons which are present in the outermost orbitals. In some metals it occurs due to magnetic moments that are associated with spins of conducting electrons. Susceptibility of a paramagnetic material is expressed as $\chi(T) = C/T$, where C is a constant and is called the Curie constant. This expression is known as *Curie law*. For characterizing a paramagnetic material reciprocal magnetic susceptibility is plotted versus temperature and a fitting gives a straight line that as shown in Fig.1.5.4. Most of the materials they don't obey curie law so modified Curie-Weiss law is used. It is expressed as given below,

$$\chi(T) = \frac{C}{T-\theta} \qquad (1.11)$$

Where, θ is a constant called Curie-Weiss temperature, normally all paramagnetic material obeys this expression and the value would be equal to zero. In some cases the value of θ would be small or less than 10 K as if they obey Curie-Weiss law. Based on the intercept of

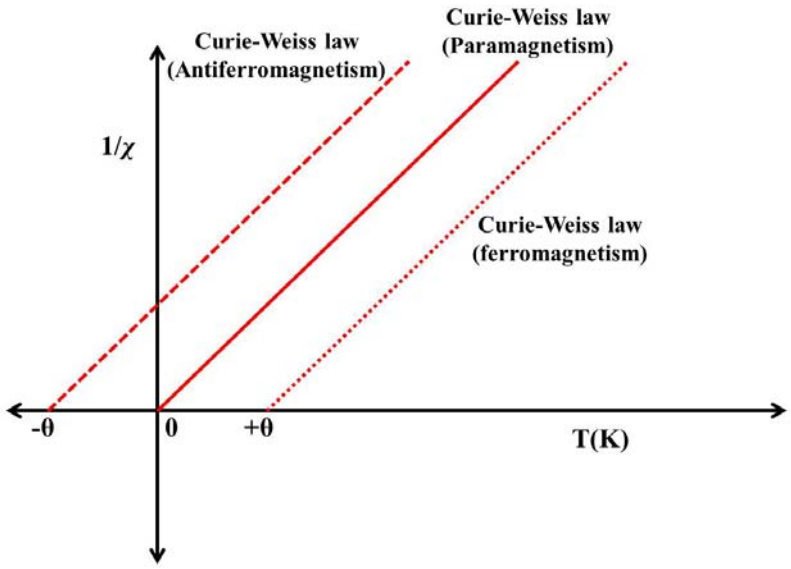

Fig.1.5.4. $1/\chi$ vs. T of different magnetism (extracted from Ref.163).

Curie-Weiss law sign of θ helps to know whether magnetic interaction would help the neighboring moments to align in the same direction or another direction (see Fig. 1.5.4). There are two different types of paramagnetism i.e., Pauli paramagnetism and Van Vleck paramagnetism. Pauli paramagnetism arises when applying external field magnetic moments get aligned due to the conduction electrons. The value of χ would be very small and is

temperature independent. Van Vleck paramagnetism arises due to thermal excitation in low-lying ground states of the system and is independent of temperature. The properties of paramagnetism are not of much practical importance, but it helps to understand the theory of ferromagnetism and ferrimagnetism.

1.5.3 Ferromagnetism

Ferromagnetism is the strongest type of magnetism among magnetic materials, without applying any external field they possess a permanent magnetic moment. Also electron spins are aligned with or without the presence of an external magnetic field. When external magnetic field is applied it spins up in the direction of applied field. Fig.1.5.5 shows the schematic view of spin arrangements in ferromagnetic material. Best example for such type of magnetism is Fe, some other transition metals like Co, Ni and Rare-earth elements like Gd, Nd, Sm etc. also shown ferromagnetic behaviour. Ferromagnetic materials show high magnetic susceptibility which is around 10^6. Another field quantity, M, called *magnetization* of solid, is defined by the expression,

$$B = \mu_0 H + \mu_0 M \qquad (1.12)$$

In the presence of an external field H, magnetic moments within a material tend to line up with field and strengthen by their magnetic fields; the term $\mu_0 M$ is a measure of this contribution. Therefore, if $H << M$ then we can write as,

$$B \cong \mu_0 M \qquad (1.13)$$

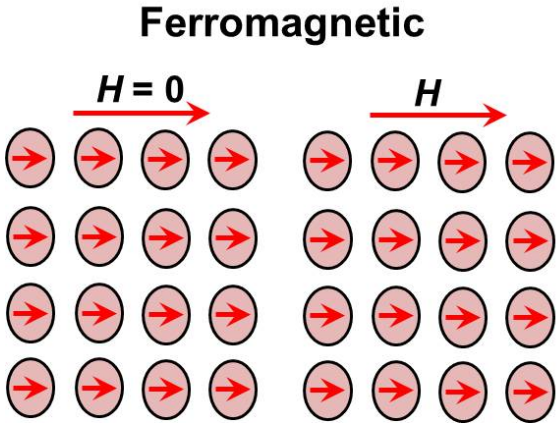

Fig.1.5.5. Schematic view of Ferromagnetic material with and without applied magnetic field (extracted from Ref.161).

Temperature dependence of magnetic susceptibility χ for ferromagnetic and antiferromagnetic materials is schematically depicted in Fig.1.5.6, The ferromagnetic materials shows a long-range order, which can undergo a phase transition at Curie temperature T_c close to Curie-Weiss temperature θ as shown in Fig.1.5.4. If θ > 0 material is ferromagnetic, and transition temperature, known as *Curie temperature* T_c is defined by

$$T_c = \frac{g\mathcal{J}\mu_B(\mathcal{J}+1)\lambda M_S}{3k_B} = \frac{n\lambda\mu_{eff}^2}{3k_B} \qquad (1.14)$$

Below Curie temperature material will be ferromagnetically ordered and above Curie temperature it behaves as paramagnetic materials which show Curie-Weiss behavior. Ferromagnetic materials shows typical *M*(*H*) curve at fixed temperatures and it behaves like a *hysteresis*. Schematic view of hysteresis loop is given in Fig 1.5.7. By fixing temperature and increasing magnetic field it gradually increases and reaches a point known as *saturation magnetization* which is usually denoted as M_s. When *H* returns to zero the value of magnetization is known as *remanent magnetization* M_r. Saturation magnetization is an intrinsic property and remanent magnetization depends upon synthesis and treatment of the material commonly known as history of that material [161].

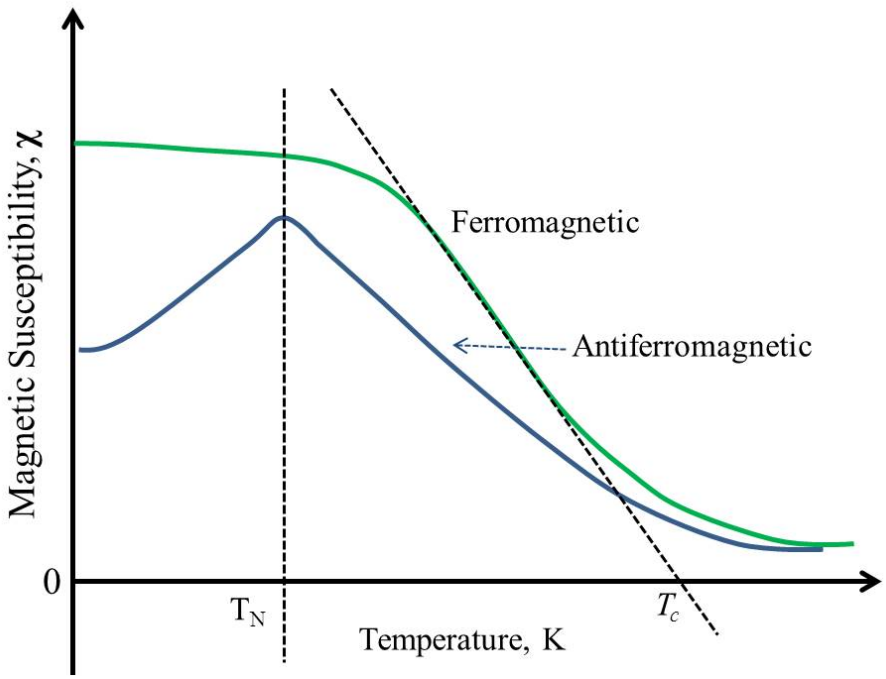

Fig.1.5.6. Temperature dependent magnetic susceptibility of ferromagnetic and antiferromagnetic material (extracted from Ref.155).

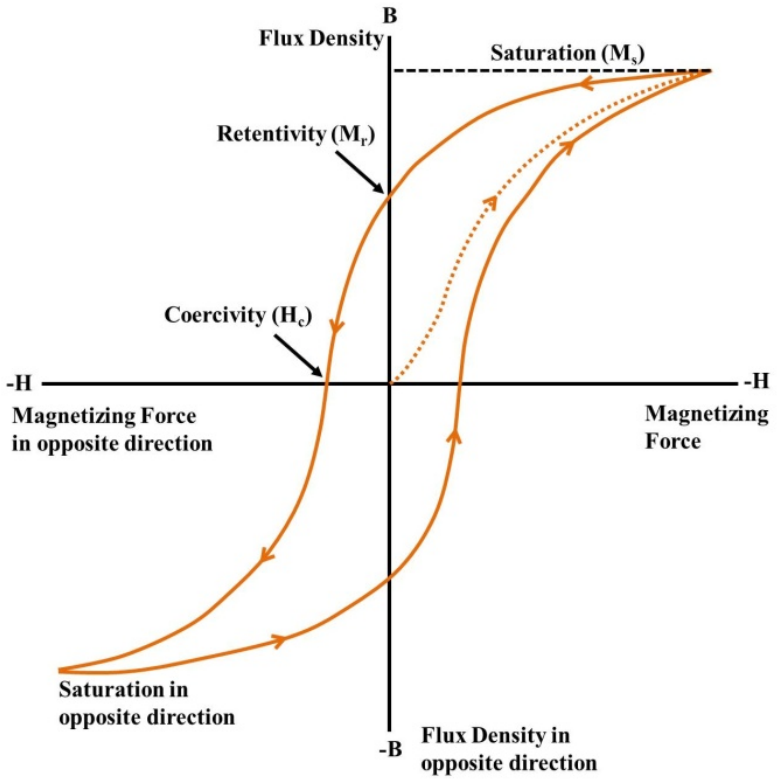

Fig.1.5.7. Hysteresis behavior of a magnetic material (extracted from Ref.161).

1.5.4 Antiferromagnetism

When an external magnetic field is applied magnetic moments gets lined up and adjacent magnetic moments are aligned in opposite directions. This phenomenon of magnetic moment coupling between adjacent atoms in materials is termed *antiferromagnetism.* Manganese oxide (MnO) is a ceramic material, which is one of the best examples that show this kind of behaviour. Manganese oxide is ionic in character, having both $Mn^{2+}$and O^{2-} ions. There is no net magnetic moment with O^{2-}ions, because spin moments gets cancelled with the orbital moments. But Mn^{2+} ions possess a net magnetic moment originated from spin moments. Arrangement of Mn^{2+} ions in the crystal system makes adjacent ions to arrange antiparallel. Schematic arrangement of this behaviour is represented in Fig 1.5.8, where magnetic moments gets opposed to each other and get cancels so that there will be no net magnetic moment in the solid [161]. Temperature dependent magnetic susceptibility for antiferromagnetic material is shown in Fig.1.5.6. Antiferromagnetic phase transition is known as Néel transition and it's usually denoted as T_N. above Néel temperature T_N the material would be paramagnetic that exhibits Curie-Weiss behavior. Néel temperature T_N and is defined as

$$T_N = \frac{g J \mu_B (J+1) |\lambda| M_S}{3k_B} \quad (1.15)$$

$$T_N = \frac{n|\lambda|\mu^2{}_{eff}}{3k_B} \quad (1.16)$$

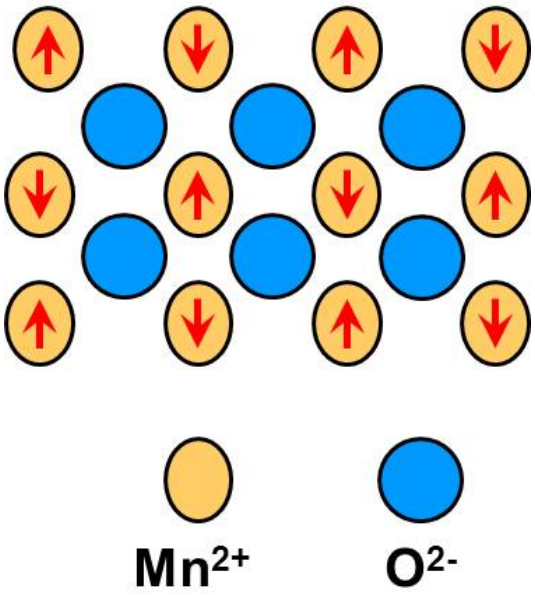

Fig.1.5.8. Schematic representation of antiparallel alignment of spin magnetic moments in antiferromagnetic manganese oxide (extracted from Ref.161).

1.5.5 Ferrimagnetism

Ferrimagnetism is a type of permanent magnetization that arises in solids and materials that exhibit such type of magnetisation are termed Ferrimagnets. Ferromagnets and ferrimagnets are similar from the macroscopic point of view, but the net magnetic moments are different. Ferrimagnets are very similar like antiferromagnets because the magnetic moments are antiparallel arranged, the only difference is that adjacent moments will have different magnitudes. Here the larger magnetic moment aligns parallel to applied magnetic field but smaller moments align opposite. Different magnetic moments align up to create a large net magnetic moment. Ferrimagnets are widely used to prepare permanent magnets and they are non-electric conducting ceramics. To know more about the principles of ferrimagnetism cubic ferrite is a good example and it's represented by the chemical formula MFe_2O_4 where M represents any metallic elements. Fe_3O_4 may be formula as Fe^{2+} O^{2-} - $(Fe^{3+})_2$ (O^{2-}) where Fe ions exist in both +2 and +3 valence states in the ratio of 1:2. Spin magnetic moment for Fe^{2+} and Fe^{3+} ion, would be 4 and 5 Bohr magneton, where O^{2-} ions are

magnetically neutral. There are antiparallel spin-coupling interactions between the Fe ions, which arises from imperfect cancellation of spin moments [161].

1.6 Aim of the thesis

The main aim of this thesis is to prepare non-oxide superconducting materials by using high-pressure and high-temperature technique and to investigate their intrinsic properties. There are many series of oxide materials synthesized using the high-pressure technique but very few works has been done in non-oxide materials using the HPHT technique. Here I chose three series of materials and extensively investigated the crystal structure, nature of superconductivity along with magnetic, electrical and thermal properties of these compounds.

(i) Ordering and Superconductivity in non-stoichiometric interstitial molybdenum carbide

To synthesize and investigate stoichiometric cubic δ-MoC by using HPHT synthesis technique, because stoichiometric δ-MoC has never been synthesized using the solid-state reaction method. I have reported the successive synthesis of cubic δ-MoC_{1-x} for the first time under different high-pressure conditions and studied the exact structure of this system. Superconducting nature and intrinsic properties like magnetic, electrical and thermal are reported for the first time.

(ii) Structure and Superconductivity in BiS_2 layered materials

To synthesize and investigate the superconducting nature of BiS_2 layered $Bi_4O_4S_3$, $LaO_{1-x}F_xBiS_2$ and to study the physical properties of this system in detail is my aim. As Bi and S are low melting point elements, synthesis of this material under ambient pressure conditions leads to the formation of eutectic alloy and some of the elements are volatile so an exact stoichiometric ratio of these materials cannot be synthesized to know its exact nature (i.e. crystal structure and properties). So I placed the sample in platinum capsule and heated under high pressure in order to stop escaping of gases while heating and quenching stops formation of eutectic alloy. For the so prepared samples structure is verified and their transport, magnetic and thermal properties are measured. Another BiS_2 layered materials $LaO_{1-x}F_xBiS_2$ was also prepared using the above-mentioned method and their structural,

transport, magnetic and thermal properties were also measured.

(iii) Substitution effects on the heavy fermion FeSi systems.

To synthesize heavy fermion FeSi systems using high-pressure and high-temperature technique and to introduce superconductivity by substitution of impurities. In addition to investigate the transport, magnetic and thermal properties of these system in detail. Heavy fermion FeSi systems are difficult to be synthesized under the normal pressure conditions and substitution or doping that can introduce superconductivity on these systems are entirely challenging. So I have successfully synthesized $Yb_2Fe_3Si_5$ followed by substituting calcium in Yb site using HPHT technique and studied the properties of these materials in detail.

References

[1] H. K. Onnes, research notebooks 56,57, Kamerlingh Onnes Archive, Boerhaave Museum, Leiden, the Netherlands.

[2] H. K. Onnes “The resistance of pure mercury at helium temperatures". Commun. Phys. Lab. Univ. Leiden **12**: 120. (1911).

[3] D. Van Dirk, and K. Peter, Physics Today **63**, 38 (2010).

[4] K. A. Müller, and J. G. Bednorz, Proc. Nati. Acad. Sci. USA **84**, 4678-4680 (1987).

[5] J. G. Bednorz, and K. A. Müller, Z. Physik, B **64** (1), 189-193. (1986)

[6] M. K. Wu, J. R. Ashburn, C. J. Torng, P. H. Hor, R. L. Meng, L. Gao, Z. J. Huang, Y. Q. Wang, and C. W. Chu, Phys. Rev. Lett. **58**, 908-910 (1987).

[7] A. Schilling, M. Cantoni, J. D. Guo, and H. R. Ott, Nature **363**, 56 (1993).

[8] L. Gao, Y. Y. Xue, F. Chen, Q. Xiong, R. L. Meng, D. Ramirez, C. W. Chu, J. H. Eggert, and H. K. Mao, Phys. Rev. B **50**, 4260 (1994).

[9] Y. Kamihara, T. Watanabe, M. Hirano, and H. Hosono, J. Am. Chem. Soc. **130**, 3296 (2008).

[10] Y. Kamihara, H. Hiramatsu, R. Kawamura, H. Yanagi, T. Kamiya, and H. Hosono, J. Am. Chem. Soc. **128** (31), 10012-10013 (2006).

[11] M. Rotter, M. Tegel, and D. Johrendt, Phys. Rev. Lett. **101**, 107006 (2008).

[12] Z. A. Ren, W. Lu, J. Yang, W. Yi, X. L. Shen, C. Zheng, G. C. Che, X. L. Dong, L. L. Sun, F. Zhou, and Z. X. Zhao, Chinese Phys. Lett. **25**, 2215 (2008).

[13] Y. Mizuguchi, H. Fujihisa, Y. Gotoh, K. Suzuki, H. Usui, K. Kuroki, S. Demura, Y. Takano, H. Izawa, and O. Miura, Phys. Rev. B **86**, 220510R (2012).

[14] S. G. Tan, L. J. Li, Y. Liu, P. Tong, B. C. Zhao, W. J. Lu, and Y. P. Sun, Physica C **483**, 94 (2012).

[15] Y. Mizuguchi, S. Demura, K. Deguchi, Y. Takano, H. Fujihisa, Y. Gotoh, H. Izawa, and O. Miura et al., arxiv: 1207.3567.

[16] P. F. McMillan, Nat. Mater. **1**, 19-25 (2002).

[17] P. F. McMillan, High. Press. Res. **23**, 7-22 (2003).

[18] J. V. Badding, Ann. Rev. Mater. Sci. **28**, 631-658 (1998).

[19] H. T. Hall, Rev. Sci. Instrum. **31**, 125-131 (1960).

[20] R. S. Bradley, and D. C. Munro, "*High-pressure chemistry*" Pergamon press, Oxford (1965).

[21] L. J. Parker, T. Atou, and J. V. Badding, Science **273**, 95-97 (1996).

[22] L. J. Parker, and M. Hasegawa, T. Atou *et al*., Eur. J. Solid State. Inorg. Chem. **34**, 693 (1997).

[23] R. J. Hemley, and R. E. Cohen, Ann. Rev. Earth Planet. Sci. **20**, 553-560 (1992).

[24] V. V. Brazhkin, and S. V. Popova, J. Less Common Metals **138**, 39-45 (1988).

[25] V. V. Brazhkin, and A. G. Lyapin, High. Press. Res. **15**, 9-30 (1996).

[26] S. M. Sharma, and S. K. Sikka, Progr. Mater. Sci. Res. **40**, 1-77 (1996).

[27] V. V. Brazhkin, A. G. Lyapin, and R. N. Voloshin S. V. Popova, E. V. Tat'yanin, and N. F. Borovikov, S. C. Bayliss, and A. V. Sapelkin, Phys. Rev. Lett. **90**, 145503 (2003).

[28] H. Kanda, Radiat. Eff. Defects Solids **156**, 163-172 (2001).

[29] E. M. Dianov, V. M. Mashinsky, V. B. Neusruev *et al*., Opt. Lett. **22**, 1089-1991 (1997).

[30] V. V. Brazhkin, High. Press. Res. **27**, 333-351 (2007).

[31] A. A. Berlin, T. Wuernisha, T. Kamiyama *et al*., Chem. Mat. **18**(1), 133-139 (2006).

[32] Z. H. Chi *et al*., J. Appl. Phys. **98**, 103519-103523 (2005).

[33] L. Gao, Y. Y. Xue, F. Chen, Q. Xiong, R. L. Meng, D. Ramirez, C. W. Chu, J. H. Eggert, and H. K. Mao, Phys. Rev. B **50**, 4260 (1994).

[34] H. Luo, S. Desgreniers, Y. K. Vohra, and A. L. Ruoff, Phys. Rev. Lett. **67**, 2998 (1991).

[35] H. Takahashi, K. Igawa, K. Arii, Y. Kamihara, M. Hirano, and H. Hosono, Nature **453**, 376 (2008).

[36] Y. Kamihara, T. Watanabe, M. Hirano, and H. Hosono, J. Am. Chem. Soc. **130**, 3296 (2008).

[37] F. C. Hsu *et al,* Proc. Natl. Acad. Sci. USA**. 105**, 14262 (2008).

[38] P. M. Shirage *et al*., Physica C. **469**, 355-369 (2009).

[39] B. T. Matthias, Phys. Rev. **87**, 380 (1952).

[40] T. H. Geballe, and J. K. Hulm, "Bernd Theodor Matthias" (National Academies Press, 1996).

[41] George F. Hardy, and John K. Hulm, Phys. Rev. 884 (1952).

[42] J. K. Hulm, and R. D. Blaugher, Phys. Rev. **123**, 1569-1580 (1961).

[43] F. Steglich, J. Aarts, C. D. Bredl, W. Lieke, D. Meschede, W. Franz, and H. Schafer, Phys. Rev. Lett. **43**, 1892–1896 (1979).

[44] H. Hegger, C. Petrovic, E. G. Moshopoulou, M. F. Hundley, J. L. Sarrao, Z. Fisk, and J. D. Thompson, Phy. Rev. Lett. **84**, 4986-4989 (2000).

[45] C. Petrovic, P. G. Pagluiso, M. F. Hundley, R. Moschovich, J. L. Sarrao, J. D. Thompson, Z. Fisk, and P. Monthoux, J. Phys. Condens. Matter. **13**, L337–L342 (2001).

[46] Schilling, M. Cantoni, J. D. Guo, and H. R. Ott, Nature **363**, 56-58 (1993).

[47] T. He, Q. Huang, A. P. Ramiraz, Y. Wang, K. A. Regan, N. Rogado, M. A. Hayward, M. K. Haas, J. J. Slusky, K. Inumara, H. W. Zandbergen, N. P. Ong, and R. J. Cava, Nature. **411**, 54 (2001).

[48] J. Nagamatsu, N. Nakagawa, T. Muranaka, Y. Zenaitani, and J. Akimitsu, Nature. **410**, 63 (2001).

[49] E. Furimsky, Applied Catalysis A: General, **240**, 1-28 (2003).

[50] C. Kral, W. Lengauer, D. Rafaja, and P. Ettmayer, J. Alloy & Comp, **265**, 215-233 (1998).

[51] A.-M. Alexander, and J. S. J. Hargreaves, Chem. Soc. Rev, **39**, 4388- 4401 (2010).

[52] G. Vitale, M. L. Frauwallner, E. Hernandez, C. E. Scott, and P. Pereira-Almao, App. Cat. A: Gen, **400**, 221-229 (2011).

[53] C. C. Yu, S. Ramanathan, and S. T. Oyama, J. Cataly, **173**, 1-9 (1998).

[54] S. Wang, X. Wang, Z. Zhang, and Y. Qian, J. Mat. Sci, **38**, 3473-3478 (2003).

[55] P. Liu, and J. A. Rodriguez, J. Chem. Phys, **120**, 5414 (2004).

[56] J. C. Grossman, A. Mizel, M. Côté, M. L. Cohen, and S. G. Louie, Phy. Rev B, **60**, 6343-6347 (1999).

[57] J. S. Lee, *Metal Carbides*, in: Encyclopedia of Catalysis, John Wiley & Sons, Inc., (2002).

[58] J. S. Lee, and D. J. Ham, *Metal Nitrides*, in: Encyclopedia of Catalysis, John Wiley & Sons, Inc., (2002).

[59] L. I. Johansson, Surf. Sci. Rep, **21**,177-250 (1995).

[60] S.T. Oyama, *The chemistry of Transition Metal Carbides and Nitrides*, First ed., Blackie Academic & Professional, Glasgow, 1996.

[61] J. G. Chen, Chem. Rev, **96**, 1477-1498(1996).

[62] S.T. Oyama, J. Sol. Stat. Chem, **96**, 442-445 (1992).

[63] P. Ettmayer, Annu. Rev. Mater. Sci, **19**, 145-164(1989).

[64] L. Volpe, and M. Boudart, J. Sol. Sta. Chem, **59**, 332-347 (1985).

[65] S. T. Oyama, J. C. Schlatter, J. E. Metcalfe III, and J.M. Lambert Jr, Ind. & Eng. Chem. Res, **27**, 1639-1648 (1988).

[66] R. Marchand, F. Tessier, and F. J. Disalvo, J. Mate. Chem, **9**, 297-304 (1999).

[67] A. G. Cairns, J. G. Gallagher, J. S. J. Hargreaves, D. McKay, E. Morrison, J. L. Rico, and K. Wilson, J. Alloy & Comp, **479**, 851-854 (2009).

[68] S.T. Oyama, Cat. Today, **15**, 179-200 (1992).

[69] H W. Hugosson, O. Eriksson, and L. Nordstrom, J. Appl. Phys. **86**, 3758-3767(1999).

[70] E. Rudy, S. Windlisch, A. J. Stosick, and J. R. Hoffman, Trans. AIME **239**, 1247 (1967).

[71] E. Rudy, Compendium of phase diagram data, Tech.Rep.AFML-TR-65-2 (1969).

[72] L. E. Toth, *Transition metal Carbides and Nitrides*, eds J. L. Margrave, Refractory materials, Vol.7 (Academic Press, New York, London, 1971).

[73] W. Krauss, and C. Politis in *Superconductivity in d- and f-Band metals,* eds. W. Buckel and W. Weber (Karlsruhe Nuclear research Centre, KfK, Karlsruhe, Germany, 1982), pp.439.

[74] P. Villars, and L. D. Calvert, *Pearson's Handbook of Crystallographic Data for Intermetallic Phases*, Vol.3 (American Society of Metals, Ohio, 1985).

[75] W. Krauss, Diploma Work, Faculty of Physics, University of Karlsruhe (1981).

[76] N. S. Athanasiou, and Studienarbeit, Faculty of Engineering, University of Karlsruhe (1983).

[77] W. Krauss, Ph.D. Thesis, Faculty of Physics, University of Karlsruhe, KfK Rep.No 4118 (1986).

[78] S. H. Jhi, S. G. Louie, M. L. Cohen, and J. Ihm, Phys. Rev. Lett. **86**, 3348 (2001).

[79] K.Yamaura, Q. Huang, M. Akaishi, and E. Takayama-Muromachi, Phys. Rev B, **74**, 184510-184515 (2006).

[80] K. Yamaura, Q. Huang, and E. Takayama-Muromachi, Phys. C. **468**, 1135-1137 (2008).

[81] W. E. Pickett, B. M. Klein, and D.A. Papaconstantopoulos, Physica B & C **107B**, 667 (1981).

[82] D.A. Papaconstantopoulos, W. E. Pickett, B. M. Klein, and L. L. Boyer, Nature (London) **308**, 494 (1984).

[83] Y. Zhoa, and S. He, Solid state Commun. **45**, 281-283 (1983).

[84] B. M. Klein, and W. E. Pickett in *Superconductivity in d- and f-Band metals,* eds. W. Buckel, and W. Weber (Karlsruhe Nuclear research Centre, KfK, Karlsruhe, Germany, 1982), p.439.

[85] E. L. Haase, J. Low Temp. Phys. **69**, 245 (1987).

[86] G. L. W. Hart, and B. M. Klein, Phys. Rev. B. **61**, 3151-3154 (2000).

[87] S. Y. Savrasov, Phys. Rev. B **54**, 16470-16486 (1996).

[88] M. Gupta, and A. J. Freeman, Phys. Rev. Lett, **37**, 16223 (1976).

[89] See, e.g., B. M. Klein and W. E. Pickett, in Superconductivity in d- and f-band metals 1982, Proc. of the IV. Conf., edited by W. Buckel and W. Weber (Kernforschungszentrum Karlsruhe GmbH, Karlsruhe, 1982), and references therein

[90] E. I. Isaev, S. I. Simak, I. A. Abrikosov, R. Ahuja, Y. K. Vekilov, M. I. Katsnelson, A. I. Lichtenstein, and B. Johansson, J. App. Phys **101**, 123519 (2007).

[91] M. J. Mehl, B. M. Klein, and D. A. Papaconstantopoulos, in Intermetallic Compounds, Principles and Practice, edited by J. H. Westbrook and R. L. Fleischer, John Wiley and Sons, London, Vol. 1, Chap. 9 (1994).

[92] H. T. Strokes, and D. M. Hatch, for more information visit http://www.physics.byu.edu/stokesh/isotropy.html.

[93] J. G. Bednorz, and K. A. Müller, *Z. Phys.* B **64**,189 (1986).

[94] M. K. Wu, J. R. Ashburn, C. J. Torng, P. H. Hor, R. L. Meng, L. Gao, Z. J. Huang, Y. Q. Wang, and C. W. Chu, Phys. Rev. Lett. **58**, 908 (1987).

[95] H. Maeda, Y. Tanaka, M. Fukutomi, and T. Asano, Japan. J. Appl. Phys. **27**, L209 (1998).

[96] A. Schilling, M. Cantoni, J. D. Guo, and H. R. Ott, Nature **363**, 56 (1993).

[97] Y. Kamihara, T. Watanabe, M. Hirano, and H. Hosono, J. Am. Chem. Soc. **130**, 3296 (2008).

[98] X. H. Chen, T. Wu, G. Wu, R. H. Liu, H. Chen, and D. F. Fang, Nature **453**, 761 (2008).

[99] Z. A. Ren *et al,*Chin. Phys. Lett. **25**, 2215 (2008).

[100] M. Rotter, M. Tegel, and D. Johrendt, Phys. Rev. Lett.**101**, 107006 (2008).

[101] X. C. Wang, Q. Q. Liu, Y. X. Lv, W. B. Gao, L. X. Yang, R. C. Yu, F. Y. Li, and C. Q. Jin, Solid State Commun. **148**, 538 (2008).

[102] K. W. Yeh *et al,* Europhys. Lett. **84**, 37002 (2008).

[103] Y. Mizuguchi, F. Tomioka, S. Tsuda, T. Yamaguchi, and Y. Takano, Appl. Phys. Lett. **94**, 012503 (2009).

[104] J. Guo, S. Jin, G. Wang, S. Wang, K. Zhu, T. Zhou, M. He, and X. Chen, Phys. Rev. B **82**, 180520 (2010).

[105] J. Nagamatsu, N. Nakagawa, T. Muranaka, Y. Zenitani, and J. Akimitsu, Nature **410**, **63** (2001).

[106] Y. Takano, H. Takeya, H. Fujii, H. Kumakura, T. Hatano, K. Togano, H. Kito, and H. Ihara Appl. Phys. Lett. **78**, 2914 (2001).

[107] J. A. Wilson, F. J. Disalvo, and S. Mahajan, Adv. Phys. **24**, (1975) 117.

[108] J. A. Wilson, and A. D. Yoffe, Adv. Phys. **18**, 193 (1969).

[109] P. J. Disalvo, Low. Temp. Phys LT-**13**, 417 (1974).

[110] N. P. Ong, and P. Monceau, Phys. Rev. B, 16, 3443 (1977).

[111] S. Kagoshima, Jpn. J. Appl. Phys. **20**, 1617 (1981).

[112] L. A. Taylor, and L. W. Finger: Carnegie Inst. Washington Geophys. Lab. Annu. Rep.

69, 318 (1970).

[113] A. R. Lennie, S. A. T. Redfern, P. F. Schofield, and D. J. Vaughan, Mineral. Mag. **59**, 677 (1995).

[114] G. Hagg, and A. L. Kindstrom: *Z.* Phys. Chem. B **22**, 453 (1933).

[115] H. Haraldsen, F. Grønvold, and J. Vihovde, Tidsskr. Kjemi Bergves. **4**, 96 (1944).

[116] T. M. McQueen, Q. Huang, V. Ksenofontov, C. Felser, Q. Xu, H. Zandbergen, Y. S. Hor, J. Allred, A. J. Williams, D. Qu, J. Checkelsky, N. P. Ong, and R. J. Cava, Phys. Rev. B **79**, 014522 (2009).

[117] S. Margadonna,Y. Takabayashi, Y. Ohishi, Y. Mizuguchi, Y. Takano, T. Kagayama, T. Nakagawa, M. Takata, and K. Prassides, Phys. Rev. B **80**, 064506 (2009).

[118] An-min Zhang, T. Xia, K. Liu, W. Tong, Z. Yang, and Q. Zhang, Sci. Reports, 01216 (2013).

[119] E. Morosan, H. W. Zandbergen, B. S. Dennis, J. W. G. Bos, Y. Onose, T. Klimczuk, A. P. Ramirez, N. P. Ong, and R. J. Cava, Nature Phys. **2**, 544 (2006).

[120] A. F. Kusmartseva, B. Sipos, H. Berger, L. Forr´o, and E. Tuti˘s, Phys. Rev. Lett. **103**, 236401 (2009).

[121] Y. S. Hor, A. J. Williams, J. G. Checkelsky, P. Roushan, J. Seo, Q. Xu, H. W. Zandbergen, A. Yazdani, N. P. Ong, and R. Cava, J. Phys. Rev. Lett. **104**, 057001(2010).

[122] X. L. Qi, and S. C. Zhang, Rev. Mod. Phys. **83**, 1057 (2011).

[123] Y. Mizuguchi, H. Fujihisa, Y. Gotoh, K. Suzuki, H. Usui, K. Kuroki, S. Demura, Y. Takano, H. Izawa, and O. Miura arXiv:1207.3145 (2012) (note to publishers: this article is not DOI 10.1016/j.physc.2012.08.003 —there is a mistake at arXiv)

[124] Y. Mizuguchi, S. Demura, K. Deguchi, Y. Takano, H. Fujihisa, Y. Gotho, H. Izawa, and O. Miura, J. Phys. Soc. Japan **81**, 114725 (2012).

[125] S. Demura *et al* 2012 arXiv:1207.5248

[126] K. Ishida, Y. Nakai, and H. Hosono, J. Phys. Soc. Japan.**78**, 062001 (2009).

[127] Y. Mizuguchi, and Y. Takano, J. Phys. Soc. Japan.**79**, 102001 (2010).

[128] Y. Mizuguchi, and Y. Takano, *Z. Kristallogr.* **226**, 417 (2011).

[129] J. Xing, S. Li, X. Ding, H. Yang, and H. H. Wen 2012 arXiv:1208.5000

[130] R. Jha, S. K. Singh, and V. P. S. Awana 2012 arXiv:1208.5873

[131] K. Deguchi, Y. Takano, and Y. Mizuguchi, Sci. Technol. Adv. Mater. **13**, 054303 (2012).

[132] J. Paglione, and R. L. Greene, Nat. Phys. **6**, 645-658 (2010).

[133] Z. A. Ren, W. Lu, J. Yang, W. Yi, X. L. Shen, C. Zheng, G. C. Che, X. L. Dong, L. L. Sun, F. Zhou, and Z. X. Zhao, Chinese Phys. Lett. **25**, 2215 (2008).

[134] M. Putti, I. Pallecchi, E. Bellingeri, M. R. Cimberle, M. Tropeano, C.Ferdeghini, A. Palenzona, C. Tarantini, A. Yamamoto, J. Jiang, J. Jaroszynski, F. Kametani, D. Abraimov, A. Polyanskii, J. D. Weiss, E. E. Hellstrom, A. Gurevich, D. C. Larbalestier, R. Jin, B. C.Sales, A. S. Sefat, M. A. McGuire, D. Mandrus, P. Cheng, Y. Jia, H. H. Wen, S. Lee, and C. B. Eom, Sup. Sci. Technol. **23**, 034003 (2010).

[135] P. J. W. Moll, R. Puzniak, F. Balakirev, K. Rogacki, J. Karpinski, N. D. Zhigadlo, and B.Batlogg, Nat. Mater. **9**, 628 (2010).

[136] A. Gurevich, Rep. Prog. Phys. **74**, 124501 (2011).

[137] A. A. Kordyuk, Low. Temp. Phys, **38**, 888-899 (2012).

[138] U. Patel, J. Hua, S. H. Yu, S. Avci, Z. L. Xiao, H. Claus, J. Schlueter, V.V. Vlasko-Vlasov, U. Welp, and W. K. Kwok, Appl. Phys. Lett. **94**, 082508 (2009).

[139] J. H. Tapp, Z. Tang, L. Bing, K. Sasmal, B. Lorenz, P. C. W. Chu, and A. M. Guloy, Phys. Rev. B **78**, 060505(R) (2008).

[140] T. Nomura *et al*., 2008 arXiv:0804.3569

[141] D. Mandrus, A. S. Sefat, M. A. McGuire, and B. C. Sales, Chem. Mater. **22**, 715-723 (2010).

[142] S. Raghu, Qi. X, C. Liu, D. J. Scalapino, and S. Zhang, Phys. Rev. B 77, 220503 (2008).

[143] K. Terashima *et al*., Proc. Natl Acad. Sci. USA **106**, 7330 (2009).

[144] H. F. Braun, Phys. Lett. A **75**, 5, 386–388 (1980).

[145] J. D. Cashion, G. K. Shenoy, D. Niarchos, P. J. Viccaro, and A.T. Aldred, J. App. Phys. **52**, 2180–2182 (1981).

[146] H. Sasame, T. Masubuchi, K. Takase, Y. Takano, and T. Watanabe, J. Phys: Conf. series: **150**, 052226 (2009).

[147] C. B. Vining, and R. N. Shelton, Phys. Rev. B: **28**, 5, 2732–2742 (1983).

[148] Y. Singh, S. Ramakrishnan, Z. Hossain, and C. Geibel, Phys. Rev. B: **66**, 014415 (2002).

[149] Y. Singh, and S. Ramakrishnan, arXiv: 0303618v1.

[150] Y. Singh, S. Ramakrishnan, Z. Hossain, and C. Geibel, Phys. Rev. B, **66**, 014415 (2002).

[151] H. F. Braun, Phys. Letters **75**A, 386 (1980).

[152] H. F. Braun, C. U. Segre, F. Acker, M. Rosenberg, S. Dey, U. Deppe, and J. Magn. Magn. Mater. **25**, 117 (1981).

[153] A. R. Moodenbaugh, D. E. Cox, and H. F. Braun, Phys. Rev. B **25**, (1981) 4702.

[154] C. B. Vining, and R. N. Shelton, Phys. Rev. B **28**, 2732 (1983).

[155] R.Nigam, *Docotr Philosophy thesis,* (2010).

[156] E. H. Brandt, Phy. Rev. B. **37**, 2349-2352 (1988).

[157] A. A. Abrikosov, *Zh. Eksp. Teor. Fiz.* (Rus.) **32**, 1442 (1957).

[158] J. Bardeen, L. Cooper, and J. Schrieffer, *Phys. Rev.* **108**, 1175 (1957).

[159] Charles P. Poole, Jr, *Hand book of superconductivity*, Academic press (2000). **(b)**R. B. Heimann, *Classic and Advanced ceramics: From Fundamentals to Applications,* WILEY-VCH Verlag GmbH & Co.KGaA, Weinheim (2010).

[160] http://hyperphysics.phy-astr.gsu.edu/hbase/solids/coop.html.

[161] William D.Callister,Jr. *Materials science and Engineering –An Introduction* ,7th Edition , John wiley & sons,Inc (2007).

[162] Mathias Getzlaff, *Fundamentals of Magnetism,* Springer Berlin Heidelberg New York ISBN 978-3-540-31150-8 (2008).

[163] A. Kumar, *Doctor of Philosophy thesis,* (2012).

Chapter 2 Experimental techniques

2.1 Introduction

Experimental techniques play the key role in experimental condensed matter physics. Numerous methods have been developed in the past decades for synthesizing and characterization of materials. Synthesizing a good sample in preferred conditions helps us to know the exact intrinsic properties of the materials. Many complex phenomenon's like magnetism, superconductivity, structural ordering and phase transition are successively studied using the experimental techniques. Material synthesized in proper conditions favor the materials to show its desired properties. There are many experimental routes for preparing polycrystalline bulk samples like solid-state ambient pressure method (*APHT*), high-pressure high-temperature synthesis method (*HPHT*) and arc-melting method are quite commonly used. Out of it, high-pressure synthesis methods favors in many ways, usage of the sample for synthesis is very limited i.e.; 0.10 to 0.3g, favor's formation of new phases due to temperature quenching. It saves reaction time, and also less escapes of poisonous gas while heating are some of them. There are many reports on the synthesis of oxide superconducting material using high-pressure and high-temperature method and it is very limited for non-oxide material.

This thesis is based on the synthesis of non-oxide superconducting materials using HPHT method for stoichiometric cubic molybdenum carbides, new BiS_2 based layered materials and heavy fermion $Yb_2Fe_3Si_5$ preparation and substituting Ca for Yb to introduce superconductivity. The as-prepared materials were characterized using X-ray powder diffraction technique to find its crystal structure and Rietveld refinement was done using RIETAN program. Transport, magnetic and thermal properties were carried out using the Physical property measurement system (PPMS) and Magnetic Property Measurement System (MPMS) from Quantum design, USA. Detailed discussions about the synthesizing procedure and characterization techniques are given in the following section.

2.1.1 High-pressure and high-temperature synthesis

High-pressure synthesis has given massive support for researchers in preparing new materials in the field of superconducting and magnetic materials. Several years back only a small knowledge of this technique was known, people used gas-compressor systems, cold-seal vessels, and autoclaves as initial devices for preparing samples under enhanced pressure conditions. Initially Bridgman developed certain anvil systems to prepare samples

under high-pressure method [1] and Bundy developed a new pair of anvils [2], which geared up the development of Hall belt type apparatus [3], where experiments were carried up to a pressure of 10GPa and the samples were heated up to 2000^{o}C simultaneously. Initially in 1980's National Institute for Materials Science (*NIMS*) Tsukuba, Japan also started using flat-belt (*FB*) type high pressure apparatus which was designed for both high-pressure and high-temperature synthesis of diamond and related materials in a approximate pressure range 8GPa. In this type of *HPHT* apparatus two anvils is present one at the upper side and another at the bottom. The upper anvil of *FB* type apparatus is fixed to the upper part of fixed setup and is separated using an insulating sheet to avoid contact between anvil and upper plate. The lower anvil is connected to cylinder and isolated using insulating sheet where the sample is mounted using a set of gaskets for it. Sample mounted to lower anvil raises up along with cylinder and then the upper gasket is placed after reaching an appropriate height. In order to estimate the volume change of the sample during compression, displacement of anvil against load used for pressing is estimated using different sensors. The load used for pressing is manually controlled using a separate nozzle pump. Once it reaches the targeted pressure it would be kept on hold until the heating is cut off. Before applying heat to sample water is circulated in space between upper anvil and lower anvil which is tightened using the rubber gasket. Graphite heater attached to anvils is supplied with high power which generates heat, voltage and current are monitored during heating. Heat in anvils is monitored using a temperature sensor and electrical resistance is monitored for all runs. After heating at a desired temperature for a period of time samples are quenched, and then the pressure will be released.

Sample cell arrangement comprises an outer pyrophyllite sleeve of 26 mm diameter with a steel ring in it and center portion consists of a graphite heater which is 12 mm diameter followed by sodium chloride and 10 % zirconium oxide sleeve inside graphite heater in order to break the contact between sample and heater. Platinum or tantalum capsules of 6.8 mm in diameter and 4.5 mm in length were used to accommodate samples weighing about 0.3g, and samples weighed were pressed and sealed. As such two pre pressed samples are placed into the sample cell by sealing both sides with NaCl and 10% ZrO mixed pellets of 6.8 mm diameter and finally, by using the graphite sleeves. Before placing the sample into gasket a current ring assembly (ceramic piece made of zirconia covered by a hard steel ring of 4 mm thick) with stainless steel plate on one side and molybdenum plate on the other side which is about 26 mm in diameter is placed into the gasket. Current ring assembly protects

the tungsten carbide anvil from thermal insulation and supply a large heating current to graphite heater present in the sample cell. The salt sleeve (NaCl and 10% ZrO mixed sleeves) present inside graphite heater serves as an insulator and as a furnace for samples placed inside the sample cell.

In 1958, Tracy Hall invented the first multi-anvil [4], high-pressure apparatus which consists of a tetrahedral-anvil which is capable of attaining simultaneous pressures up to 10 GPa and temperatures above 3000 K. In the past half century, multi-anvil apparatus (MAA) were increasing gradually and now cubic anvil apparatus can reach pressures close to 100 GPa at high temperatures. In early 1980's these high-pressure apparatus was utilized along with *insitu* X-ray diffraction and synchrotron radiation facilities. Now there are various technologies to develop these kinds of apparatus for laboratory use for studying the behaviour of materials by varying the pressure and temperature. Cubic anvil type high-pressure apparatus is also used to prepare samples, pictorial view of instrument facility in our lab is shown in Fig.2.1.1.

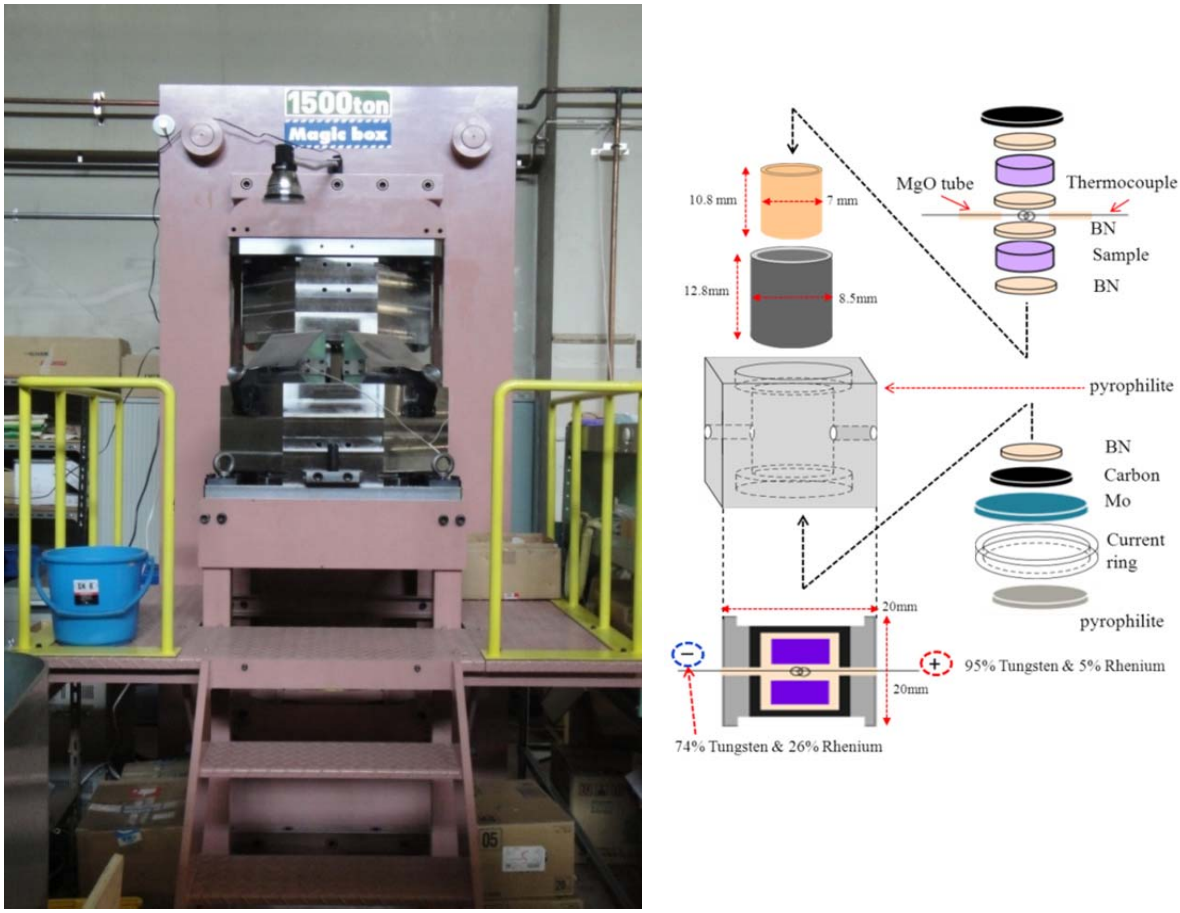

Fig.2.1.1. Pictorial view of Cubic anvil high-pressure apparatus, (b) schematic view of the sample arrangement into the sample cell

The instrument contains two heavy blocks made of stainless steel. The lower part is mounted with five cubic anvils, the top block is fixed, and one cubic anvil is mounted to it. All the anvils and blocks are separated using insulation sheets in order to break the contact between the anvils. Bottom five cubic anvils are arranged in regular position with proper intervals and sample is placed in between them. A schematic view of the sample cell arrangement is shown in Fig.2.1.1 (b). Heavy block which holds all five anvils in bottom position is raised upwards and a pump controls the press load. Anvil displacement versus press load is checked in order to know the change in volume of the sample. Heating power is supplied to graphite heater and the voltage and current are monitored during heating. Temperature is monitored by a W:Re5-W:Re26 thermocouple during heating. Details of sample prepared using this instrument are presented in chapter 3, 4 & 5.

Synthesis of δ-MoC_{1-x} by belt-type HPHT

Polycrystalline δ-MoC_{1-x} is prepared from fine molybdenum (99.99%, ~3 μm, Kojundo Chemical Lab.) and carbon (Tokai carbon) powders. A mixture of both powders with a varying molecular ratio of Mo: C = 1: 1-x (x = 0.00, 0.05, 0.10, 0.15, 0.20, 0.25, 0.30, 0.35) was each set into a flat belt-type high-pressure apparatus in which the powder mixture was heated at 2000°C for 10–30 min at an elevated pressure of 6 GPa, followed by quenching to ambient temperature before releasing the pressure.

Synthesis of $Bi_4O_4S_3$ and $LaO_{1-x}F_xBiS_2$ by cubic anvil HPHT

Polycrystalline $Bi_4O_4S_3$ is prepared from fine Bi_2O_3 (99.99%; Soekawa Chemical Co., Tokyo), Bi_2S_3 (99.9%; Kojundo Chemical Lab. Co., Sakado), and S (99.99%; Kojundo Chemical Lab. Co.) powders. The above mentioned powders are mixed in a stoichiometric molecular ratio and placed in a cubic multi-anvil high-pressure apparatus. They are heated at a specific temperature between 500 and 900°C for 30 min at an elevated pressure of 3 GPa and quenched to room temperature before releasing pressure. The mixture is sealed in a Pt capsule and separated from Pt by a hexagonal boron nitride inner cell. The inner cell did not react with mixed components, as it was evident from its unchanged color (white) after heating. Also, polycrystalline samples of $LaO_{1-x}F_xBiS_2$ with x = 0, 0.1, 0.2, 0.3, 0.4, 0.5, 0.6, 0.7, 0.8, 0.9, 1.0) are prepared using fine powders of La (99.99%; rare metallic.co Ltd), La_2O_3 (99.99%; rare metallic.co Ltd), LaF_3 (99.99%; rare metallic.co Ltd), Bi_2S_3 (99.9%; Kojundo Chemical Lab. Co., Sakado), and S (99.99%; Kojundo Chemical Lab. Co.) powders. The above-mentioned powders are mixed in a stoichiometric molecular ratio, transferred to a

Pt capsule sealed and placed in a cubic multi-anvil HP apparatus. They are heated at a specific temperature between 850 to 890°C for 30 min at an elevated pressure of 2 GPa and quenched to room temperature before releasing pressure.

Synthesis of $Yb_{2-x}Ca_xFe_3Si_5$ by cubic anvil HPHT

Polycrystalline samples of $Yb_{2-x}Ca_xFe_3Si_5$ with x = 0, 0.2, 0.4, 0.6, and 0.8 are synthesized by mixing fine powders of pure Yb (99.9% purity; Rare Metallic Co., Ltd), Iron (Fe; 99.9% purity; Rare Metallic Co., Ltd), Silicon (Si; 99.9% purity; Wako Pure Chemical Industries, Ltd), and calcium silicide (CaSi; laboratory made). CaSi is prepared from Ca and Si pieces (99.9% purity; Rare Metallic Co., Ltd) by an arc melting method in an argon atmosphere by repeatedly arc melting to obtain a homogeneous mixture. Approximately 10% of Ca pieces are further added to the stoichiometric starting composition during the melting process. A 1:1 ratio of Ca:Si is confirmed by x-ray diffraction (XRD) from a sample of the prepared powder. A well ground mixture of all powders is pressed into a pellet, placed in a pre-prepared pyrophyllite sample cell, and heated in a cubic anvil type high-pressure apparatus at 1500°C under a pressure of 5 GPa for 20–30 min and quenched to ambient temperature before releasing the pressure.

2.1.2 Solid state reaction method under ambient pressure

The solid-state reactive method is most widely used for synthesizing from a mixture of solid starting materials. A solid metal does react in normal temperatures so high temperature heating is needed for synthesizing compounds of good quality. The desired amount of samples are weighed in glove box, ground well, pelletized, and placed in a quartz tube that is sealed at one end before placing the sample and closed using a knob at the other end and finally sealed under vacuum conditions in order to get rid of moisture absorbent in pelletized sample. The as-prepared sample in quartz tube is heated at desired conditions. Drawbacks of preparing samples under this condition are: they consume more time and the quantity of powders for preparing a pellet sample is too high and costly. In this thesis I report the preparation of polycrystalline $Bi_4O_4S_3$ sample prepared under solid state reaction method. $Bi_4O_4S_3$ sample was prepared, using fine powders of Bi_2O_3 (99.99%; Soekawa Chemical Co., Tokyo), Bi_2S_3 (99.9%; Kojundo Chemical Lab. Co., Sakado), and S (99.99%; Kojundo Chemical Lab. Co.). The stoichiometric mixture is pressed into a pellet and heated at 450°C for 10 hours in an evacuated quartz tube.

2.1.3 ARC melting method

ARC melting under vacuum condition is a secondary melting process for preparing metal blocks with good mechanical uniformity for highly challenging applications. Preparing samples by arc-melting method favors some advantages like alloys of high quality that cannot be prepared by other methods and consumes less time for melting different elements to form alloys. For synthesizing some complex systems, starting compositions play a major role; because it forms mixtures while long heating and to avoid such cases certain alloys can be prepared using an arc melting method that can favor the formation of a single face material. In the same way for preparing samples like molten materials using arc melting method solidification time can be tightly controlled.

Fig.2.1.2. Pictorial view of arc melting furnace

In addition, it controls microstructure and the ability to minimize separation while heating. Some complex alloys that cannot be prepared using the normal synthesis techniques can be easily prepared using arc melting methods. Elements like carbon, sulfur and

magnesium that have high vapor pressure are contaminated easily and this can be lowered. While preparing these samples some gas can be evolved but while using the melting process gas evolved could be collected in the chamber from liquid melts of substances that are used for melting. Also porous nature formation in alloys can be eliminated. Pictorial view of the arc melting furnace provided in our group is shown in Fig.2.1.2

2.2 Structural characterization

2.2.1 Powder X-Ray diffraction

X-ray powder diffraction (XRD) is an instrumental technique primarily used for identifying crystalline phase of a material and the purity of sample prepared. In 1985, the greatest Scientist W.C. Röntgen discovered X-rays, and diffraction theory was put forth by Max von Laue in the year 1910. Followed by the English physicists Sir W.H. Bragg and his son Sir W.L. Bragg developed a new relationship in 1913 to explain the mechanism of X-ray diffraction. They explained that when an incident beam strikes to the surface of a material a diffracted beam of X-rays will leave the crystal at an angle equal to that of the incident beam. The general relationship between the wavelength of incident X-rays, angle of incidence and spacing between crystal lattice points of atoms is known as the Bragg's law, given as

$$n\lambda = 2d \sin\theta \qquad (2.1)$$

Where n is the order of reflection, λ is the wavelength of incident X-rays, d is the interplanar spacing of the crystal and θ is the angle of incidence. The scheme of Bragg's law is shown in Fig.2.2.1. If the Bragg's law is satisfied, then reflected beams would be in phase and the interactions of waves are interconnected. The patterns as collected can be identified using ICDD (International Centre for Diffraction Data) powder diffraction file (PDF). Powder pattern can be indexed from a set of d-spacing values and is sometimes very difficult to identify the exact phase's that crystallizes in lower symmetry. So structural refinement programmers can be used to refine the structure to extract the exact phase, commonly the programs such as RIETAN suite are generally used [6-9]. The detected crystalline phase provides information about unit cell dimensions and chemical composition of materials. In this thesis powder diffraction patterns of as-synthesized materials were collected using the X'Pert Pro system (PANalytical) using monochromatic Cu-Kα radiation. The diffractograms were recorded in the 2θ ranging from 5-80° with 2θ step size of 0.06° and step time of 2s.

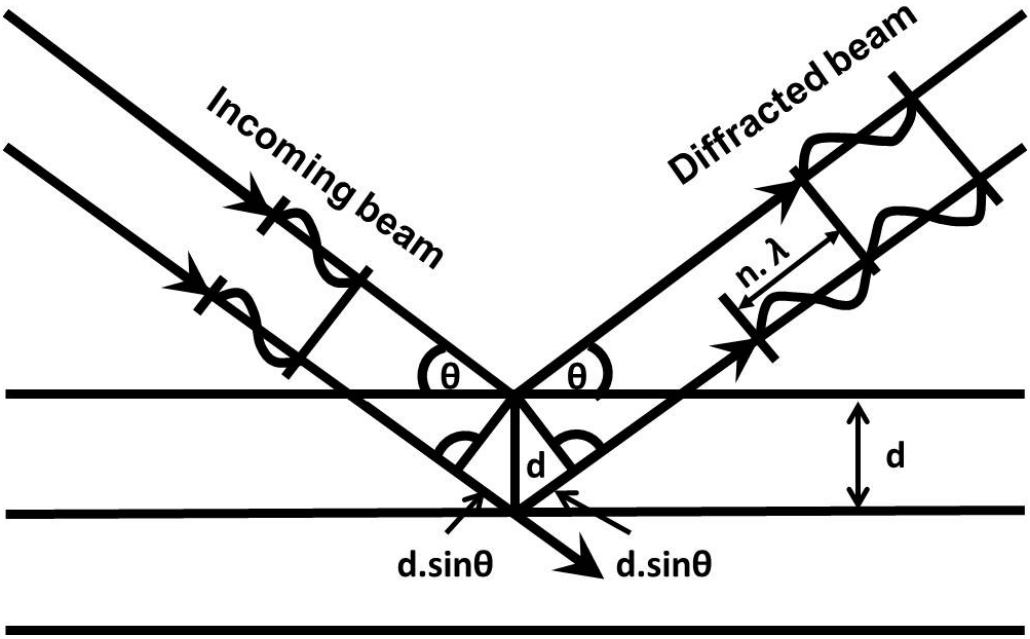

Fig.2.2.1. Schematic view from the derivation of Bragg's law (extracted from Ref.5).

2.2.2 Rietveld refinement

Powder diffraction is one of the best methods for identifying phases, measure lattice parameters and imperfections in the crystal structure of some materials. However several methods were put forth to known more from the observed patterns and to figure out the structures, later in 60's H.M. Rietveld created some new solutions how to refine the crystal systems, identifying phases, point out structural imperfections and analyzing the structure. So far lots of developments have taken place in this technique and information's of crystal systems are studied in detail. Refinement technique is nothing but matching the measured profiles with the theoretical approach by varying the parameters. For a perfect refinement of diffraction lines there are six factors that play a vital role in smoothing the affected relative intensities. The six factors are Lorentz factor, polarization factor, structure factor, absorption factor, temperature factor and multiplicity factor. Before starting a refinement some important steps should be carefully solved. To collect data from a desired sample, instrumental quality should be rectified i.e. diffractometer geometry, alignment and the radiation suitable for sample. Sample molders and divergence slits should be carefully fixed in order to get rid of large background that can destroy sample quality.

Background contribution for peaks has two approaches either it can be subtracted or it can be modeled by using some functions which contains several refinable parameters. Simple pattern files can be subtracted were peaks are fixed to standard position but for some

complex patterns it should be refined several times to bring it in a standard position and the variance would be assumed to be zero as it cannot be estimated. While refining background using modeled polynomial functions would be the perfect method to get a good fit. In some rare cases if polynomial functions don't fit perfectly into patterns then background subtraction would be the only choice. In the case of synchrotron XRD patterns there are high possibilities of structural disorders so the background should be subtracted.

Peak shape functions provide accurate shapes of peaks which gives a good fit to Rietveld refinement. Good peak shapes are observed only by a better measurement technique from the instrument itself or the 2θ values vary. Peak shape functions are investigated according to Lorentzian and Gaussian parameters using pseudo-Voigt approximation in the case of neutron and X-ray diffraction data's. If full width half max values are not properly refined then Gaussian parameters U, V and W would lead to some unusual parameters even if Lorentzian parameters like x and y will be in good agreement and fitting. Before refinement we should choose a proper fitting model and input the atomic positions. If proper structure models are not known then there would be change in profile parameters that can deviate calculated intensities from observed one and further refinement makes complications to proceed further. In such case structure free models are being used initially to fit observed intensities to generate initial profile parameters. The reliable structural model can be achieved by further proceeding with changing the profile parameters and refining for several times. Initially, before starting to refine profile parameters we should check if the observed and calculated intensities can match well. For this before starting refinement we should measure the sample with some standard like Si to get exact unit cell parameters. Rietveld refinement should be started by using a good structure model followed by subtracting the background and inputting profile parameters, unit cell parameters etc. Achieving a good refinement, several cycles of refinement of all parameters are needed. We should monitor profile fit and parameter shift while refining several cycles because they are the major information's for a pattern or it can be monitored by checking the reliability factor R. If reliability factor is too high then the input parameters are not proper. For proceeding further, refinement parameters should be changed and refined further several times. Profile parameters and structural parameters should be refined simultaneously to get a good fit.

Best Rietveld refinement fit for observed and calculated patterns can also be observed numerically using R values. Where the weighted profile R_{wp} is given as

$$R_{wp} = \{\sum_i w_i [y_i(obs) - y_i(calc)]^2 / \sum_i w_i [y_i(obs)]^2\}^{1/2} \quad (2.2)$$

To calculate fitting of peaks, R_{wp} with background elimination also should be calculated. Expected R value should be identical with the R_{wp} value then R_{exp} can be given as

$$R_{exp} = [(N - P) / \sum_i^N w_i y_i(obs)^2]^{1/2} \quad (2.3)$$

Where N and P are number of observations and parameters, for goodness of fit ratio of both R_{wp} and R_{exp} are determined

$$\chi^2 = R_{wp}/R_{exp} \quad (2.4)$$

R_{wp} value that is obtained finally after every refinement is the best fit of data that is given using Rietveld refinement for a structure [10-21].

2.2.3 Transmission Electron Microscopy (TEM)

TEM is a microscopic technique, when a beam of electrons is transmitted through an ultra thin sample, it analyses the microstructure with atomic scale resolutions. TEM consists of four different parts, Electron gun, electron lenses, Sample stage and Viewing chamber. This forms as a whole an electro-optical system called the TEM column. The TEM electro optical system is mainly divided into two parts, First one called illumination system which defines how electrons hit the sample and second is the imaging system that determines how an image or diffraction pattern are formed. In TEM, electrons are emitted by a filament and it's accelerated by high voltage (100-300 kV). This accelerating voltage determines wavelength of the electron beam and mathematically related by an equation,

$$\lambda = (\frac{1.5}{V})^{1/2} \quad Å \quad (2.5)$$

Once if it leaves the electron source, electron beam is focused using electromagnetic lens and metal apertures. As to get a final image in TEM three types of lenses are essential and they are the condenser, objective and projector lenses. The main function of condenser lens is to focus clearly on the beam of electrons coming towards sample, and to give uniformity for the sample. Objective lens plays the role to enlarge an illustrated portion of specimen and to further focus more by projector lens. The electrons that pass on to form

images are sometimes stooped or deflected by dense atoms present in the sample and that area is being subtracted from sample image. Thus, images are formed in black and white and projector lens images to the phosphor screen. Image darker portion represents that very few electrons were transmitted through, sometimes it can be denser or thicker. While the lighter area corresponds, more electrons are transmitted through thinner or less dense area. As mentioned in the above portion wavelength of electron accelerated in a TEM is much smaller than that normally used for an X-ray diffraction. This diffraction can be used to reveal more of the two dimensional distribution of reciprocal lattice points. TEM selects the nano grain size of single crystals for diffraction experiments so it is very limited for other methods to do so [22].

2.2.4 Electron Probe Micro Analysis (EPMA)

Electron probe microanalysis is a hybrid instrument with the combination of a Scanning electron Microscope (SEM) and X-ray fluorescence spectrometer (XRF). Electron microprobe is generally used for X-ray microanalysis and to image materials. The samples taken for analysis should be solid materials that are conductive and stable under vacuum, also while electron beam bombardment. The prime feature of this technique is focusing a fine spot size of about 1μm. Samples of such size are imaged in detail and analyzed to estimate the

Fig.2.2.2. Pictorial view of Electron probe micro analyzer

qualitative and quantitative variations in its chemical composition and microscopic distribution of elements are also spotted. Materials like alloys, metals, minerals, glasses, thin films etc. are analyzed. A pictorial view of EPMA facility JXA-8900F from JEOL present in material analysis station at NIMS is shown in Fig.2.2.2. Sample preparation for EPMA is an important step in getting good results as the samples are too small in micron size gets contaminated easily over its surface. The samples prepared must be clean and surface should be polished flatly to approximately 0.05 μm in addition, it should be stable under vacuum and electron bombardment. Once if the sample is prepared it should be coated with a layer of carbon or any conductive material using an evaporator and the thickness of coating should be roughly 10-15 nm. EPMA is normally used to determine the chemical information and the spatial information. Also two different mapping modes are available, namely digital mapping and counter mode mapping. Both of them give good results with a slower acquirement with low resolutions [23].

2.3 Transport, magnetic and thermal measurements

Superconducting Quantum Interference Device (SQUID) is one of the most sensitive devices available for measuring the physical and magnetic properties of materials. Magnetic and Physical property measurements shown throughout this thesis was carried out using MPMS and PPMS designed by Quantum design USA. A basic mechanism of SQUID while measuring a sample is that it does not detect the magnetic field directly, but the sample moves through a superconducting coil, where current is being supplied. The magnetic moment present in sample produces an electric current and is detected by the coils. The net change of current in the detection coil produces variations in SQUID output which is proportional to the magnetic moment of the sample. Magnetic and Physical property measurement systems are explained in detail below.

2.3.1 Magnetic property measurement system (MPMS)

Any kind of metals or alloys can exhibit some type of magnetic behavior. Magnetometer is used for measuring the amount of magnetism in a material. To know the type of magnetism we should study how the magnetization gets changed at different temperature and changes in size at different magnetic field. There are two different principal magnetic measurements to determine the type of magnetism. They are Magnetization as a function of applied magnetic field named as M(H) measurement and magnetization as a

function of temperature known as M(T) measurement. Where H is the applied magnetic field applied from the superconducting coil. M(H) measurements are carried out at a fixed temperature T and by varying the applying magnetic field H which shows a hysteresis like behavior. In case of M (T) measurements the applied field H will be fixed and temperature T will be varied. These measurements give information's regarding the origin of the magnetic behavior.

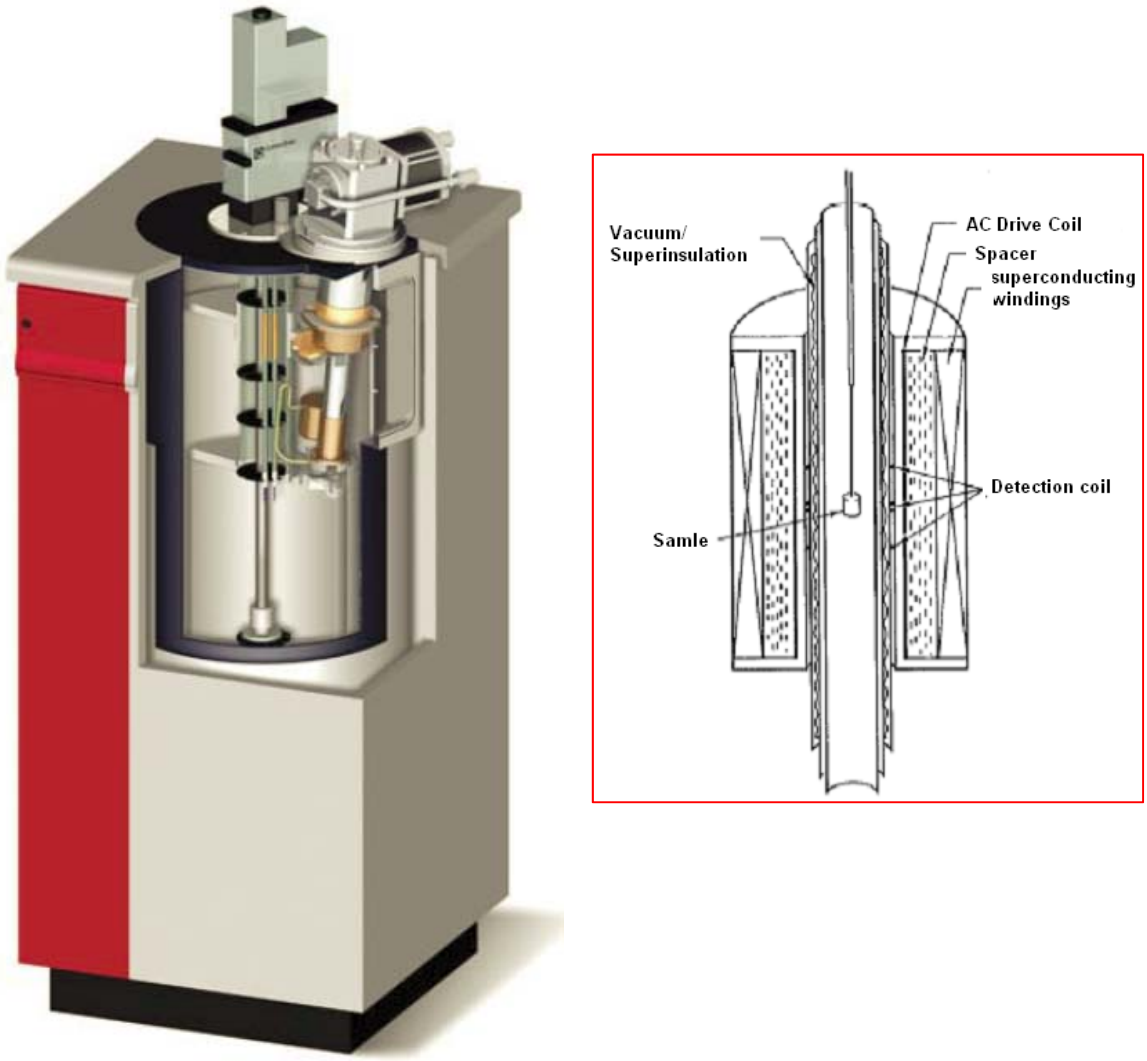

Fig.2.3.1. Pictorial view of Magnetic property measurement system and schematic expanded view of sample in between the detection coil (extracted from Ref.26)

In this thesis Magnetic susceptibility (χ) measurements for the transition carbide MoC samples, BiS_2 based layered $Bi_4O_4S_3$, $LaOBiS_2$ and Ca substituted $Yb_2Fe_3Si_5$ were carried out using Quantum Design Magnetic Property Measurement system (MPMS), which

works using a superconducting solenoid magnet. The pictorial view of this measurement facility in our laboratory is shown in Fig.2.3.1. The samples are measured from 2 to 15K in a magnetic field (H) of 10 Oe in both the field cooling (FC) and Zero field cooling process (ZFC). Loosely gathered powders of the samples weighing about 15 mg to 30 mg is measured by placing it in the sample holder. The schematic view in Fig.2.3.1 shows how the sample should be placed in between the detection coil before measurement. The scanning length of the sample is 4 cm and at each point the susceptibility is measured three times in order to get an average value. For studying the magnetic behavior of $Yb_2Fe_3Si_5$ samples substituted by calcium for Yb, M(T) measurements were carried out by varying the temperature from 2 - 390K in a fixed applied magnetic field of 1 kOe. Magnetic hysteresis loops are also measured in the same process by varying the applied magnetic field [24-27].

2.3.2 Physical property measurement system (PPMS)

Physical property measurement system (PPMS) from Quantum design was used to measure the transport properties like Electrical and Thermal transport. Electrical transport measurement otherwise known as the resistivity measurement and thermal transport includes thermopower or Seebeck coefficient (k), thermal conductivity (σ) and heat capacity (C_p) is measured in all the samples given in this thesis. Temperature dependent resistivity is measured to know zero resistivity and T_c by measuring it in different temperatures ranging between 2 to 300K. Field dependent resistivity is also measured by varying fields between 0 Oe to 9 Tesla to know the intrinsic properties like the upper critical field H_{c2}, etc. DC resistivity is measured using the four probe method where a piece of the sample is cut and polished to a rectangular shape, which is fixed with 4 slices of gold or platinum wires using silver epoxy as current and voltage leads over the top of the sample. To reduce contact resistance, silver epoxy used for contact points are heated or placed in a vacuum oven to completely dry the contact points. On the user bridge board over measuring puck there are three channels each having four labeled contact pads where the four terminals in the sample is connected with it. A schematic view of the DC resistivity puck is shown in Fig.2.3.2, where three samples are soldered to measurement puck for four probe measurements. Contact points are checked clearly using a multimeter to confirm whether the connection between sample and probes are properly fixed. The sample pack as prepared is mounted to sample chamber in PPMS instrument for measurement using puck extractor. While measure sample 1 to 5 mA of

current is passed through a sample and we can observe some corresponding voltage drops across both voltage probes. The resistivity of the sample is calculated using the formula,

$$\rho = R\frac{A}{L} \qquad (2.6)$$

Where, A represents an area of cross-section for the sample, L distance between two voltage probes and R is the measured resistance.

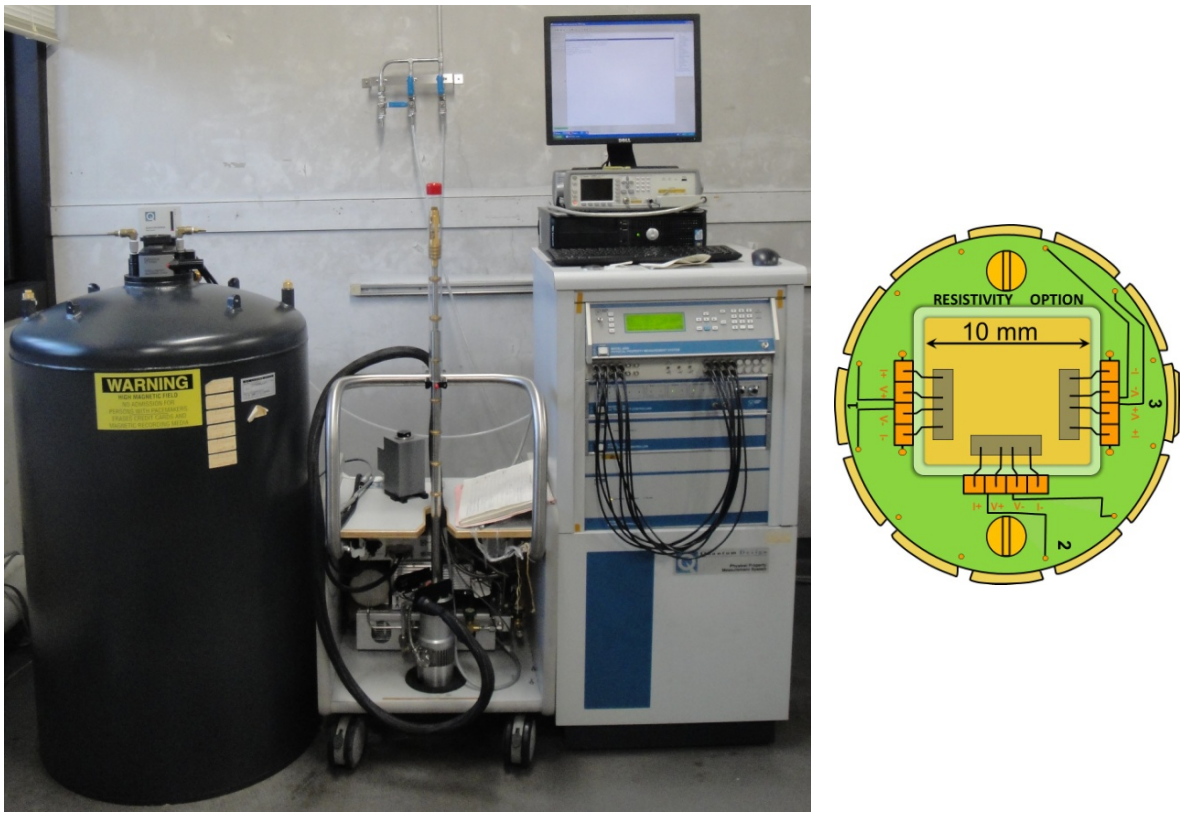

Fig.2.3.2. PPMS 9 tesla from Quantum design and schematic view of designated DC resistivity puck with three samples for concurrent measurements

Specific heat (Cp) measurement also shown in this thesis is carried out using Quantum design PPMS instrument facility in our lab as shown in Fig.2.3.2. Specific heat is nothing but known amount of heat required for changing the temperature of a 1gm material by 1K. The prime hope of measuring specific heat in solids is that can provide considerable information about lattice, electronic, and even magnetic properties of materials. Specific heat measurements, gives results between experimental results and theoretical predictions of electronic and magnetic energy levels. We use the relaxation technique to measure the specific heat of the sample that combines each measurement cycle, which is a heating period followed by a cooling period. The specific heat option fits the entire temperature response of

the sample platform by using a numerical model that considers both thermal relaxation of sample platform to bath temperature and relaxation between sample platform and sample itself. We used small square shaped samples weighing approximately around 8 - 15 mg. Specific heat measurements for each sample were carried out at different temperature ranging between 2-300K under 9 Tesla magnetic field.

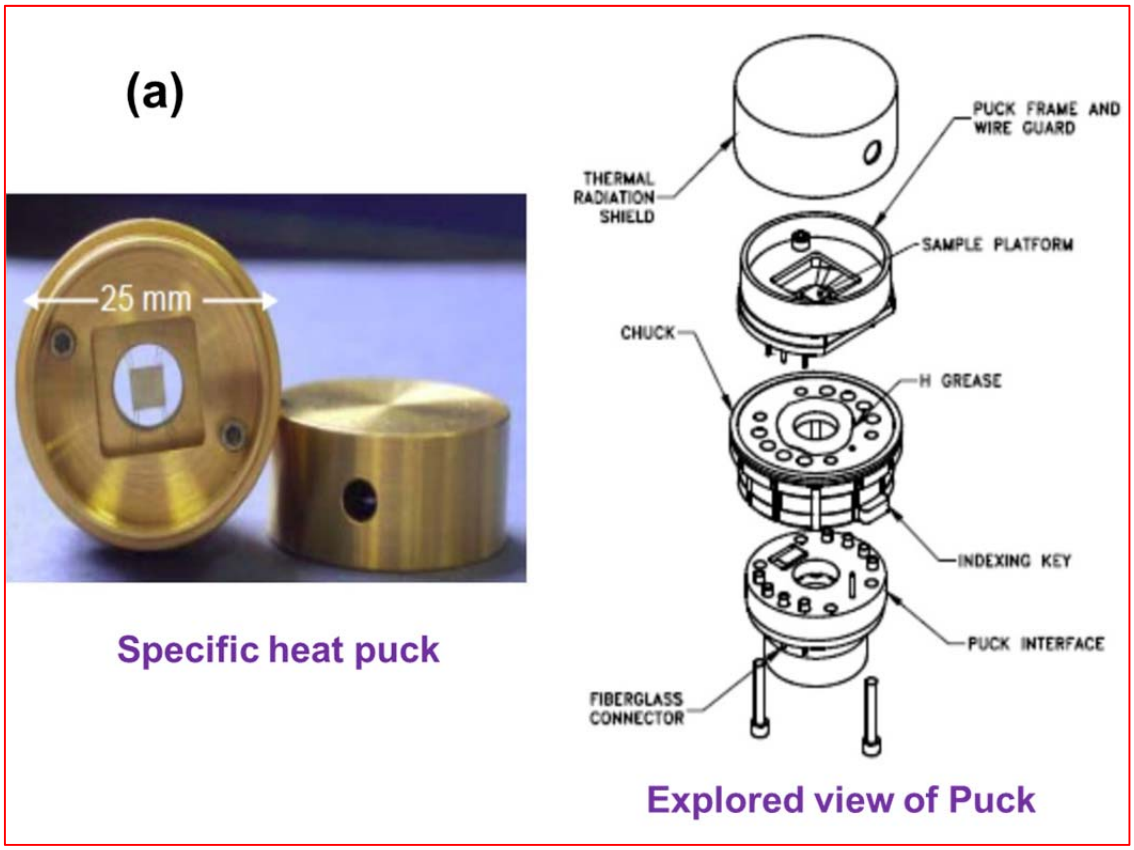

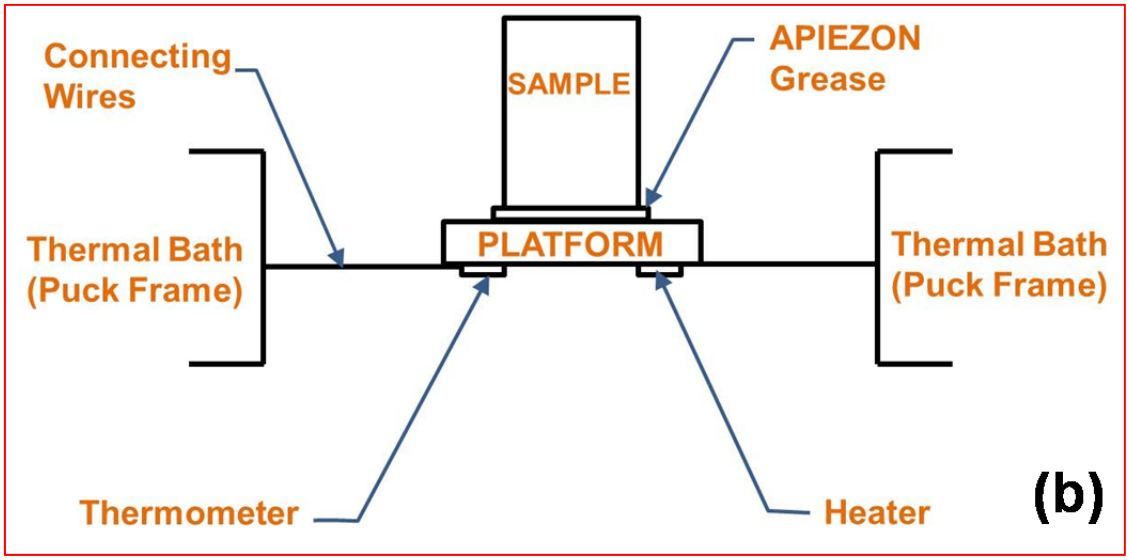

Fig.2.3.3. (a) Pictorial and explored view of the puck (b) Scheme of sample mount for heat capacity measurements in side view (extracted from Ref.26).

Pictorial and explored view of the heat capacity puck is shown in Fig.2.3.3. Puck contains three parts like, resistive platform heater, platform thermometer and puck thermometer. While the sample platform itself acts as puck thermometer, platform heater and platform thermometer are attached bottom side of it. Electrical connections for platform thermometer and heater are connected using four different wires on both sides holding as if the sample platform. Frame of puck prevents from damage to sample platform and four wires on both sides. Thermal contact of puck to base of the sample chamber is through a chunk which is above green fiberglass connector and which also locks puck to base chamber. Before start using any puck it should be calibrated. Before starting to measure sample first addenda measurement should be carried out using a thin layer of apiezon grease which acts as a thermal contact to the platform. Puck is mounted to the base chamber after applying a thin layer of grease and sufficient amount of vacuum about 0.01 mTorr is applied to eliminate residual gas. A charcoal holder is used to decrease pressure at the base of the chamber. Proper sequence files are selected for addenda measurement and executed. Same way the sample is mounted to puck and measurements are carried out at desired temperature range. Different models are used for analyzing raw measurement data to assume sample and sample platform are in good thermal contact. The simplest model is normally used by heat capacity software to measure addenda and most samples. Two-tau model is used if thermal contact between sample and sample platform is poor because it stimulates the effect of heat flowing between sample platform and puck [24-27].

References

[1] P. W. Bridgman, J. Appl. Phys, **12**, 461 (1941); Rev. Mod. Phys, **18**, 1(1946).

[2] F. P. Bundy, Rev. Sci. Instr, **48**, 591 (1977).

[3] H. T. Hall, Rev.Sci.Instr, **31**, 125 (1960).

[4] Robert C. Liebermann Hig. Press. Res, **31**, 4, 493–532 (2011).

[5] http://serc.carleton.edu/research_education/geochemsheets/techniques/XRD.html

[6] F. Izumi, J. Ceram. Soc. Jpn, **111**, 617 (2003).

[7] F. Izumi, S. Kumazawa, T. Ikeda, W-Z.Hu, A. Yamamoto, and K. Oikawa, Mater. Sci. Form, **59**, 378 (2001).

[8] F. Izumi, and T. Ikeda, Mater. Sci. Form, **198**, 321 (2000).

[9] F. Izumi, and K. Monna, Solid state Phenomena, **130**, 15 (2007).

[10] D. Watkin, *Refinement of crystal structures*, pages- 169-185.

[11] W. Clegg, A. J. Blake, R. O. Gould, and P. Main, *Crystal structure analysis: principles and practice*, Oxford University press, Oxford UK (2001).

[12] A. W. F. Edwards, John Hopkins University press, Baltimore, USA (1992).

[13] C. Giacovazzo, H. L. Monaco, G. Artoli, D. Veterbo, G. Ferraris, G. Gilli, G. Zanotti, and M. Catti, *Fundementals of crystallography*, 2nd edn, Oxford University press (2002)

[14] F. H. Herbstein, Acta.Crystallogr, **B56**, 547-557 (2000).

[15] U. Van der Maelen, Crystallogr. Rev, **7**, 125-180 (1999).

[16] P. Müller, R. Herbst-Irmer, A. L. Spek, T. R. Schneider, and M. R. Sawaya, *Crystal Structure refinement: A Guide to SHELXL*, Oxford University press.UK (2006).

[17] S. Parkin, Acta Crystallogr, **A56**, 157-162.

[18] A. L. Spek, J. Appl. Crystallogr, **36**, 7-13 (2003).

[19] D. E. Tronrud, Acta Crystallogr, **D60**, 2156-2168 (2004).

[20] N. Walker, and D. Stuart, Acta Crystallogr, **A39**, 158-166 (1983).

[21] D. J. Watkin, Acta Crystallogr, **A50**, 411-437 (1994).

[22] R. F. Egerton, *Physical principles of Electron Microscopy*, An Introduction to TEM, SEM, AEM, Springer science + Business Media, Inc, New York, USA (2005).

[23] J. I. Goldstein, D. E. Newbury, P. Echlin, D. C. Joy, C. Fiori, and E. Lifshin, *Scanning electron Microscopy and X-ray Microanalysis*, 2nd Edn, Plenum, New York. (1992)

[24] M. McElfresh, *Quantum Design,* (1994).

[25] C. L. Fleck, *Docotr Philosophy thesis,* (2011).

[26] D. Martien, *Quantum Design,* (2002).

[27] Quantum design Inc. *PPMS Manual*, 11th edition (2004).

Chapter 3 Structural, superconducting, magnetic and thermal properties of cubic molybdenum carbide

3.1 δ-$MoC_{0.681}$ cubic molybdenum carbide phase

In this chapter, I would like to discuss in detail about the transition metal carbide δ-MoC_{1-x} phase. Binary transition metal (*Tr*) carbides normally crystallize in a cubic structure if the Hägg's rule ($r_C/r_{Tr} < 0.59$, r_C and r_{Tr} refer to the atomic radii of carbon and *Tr*, respectively) is satisfied [1]. As a result of strong covalency between the *p*-wave and the sp^3d^2 hybrid function, *Tr* carbides typically presents great hardness and high melting point characteristics [2,3]. Interestingly, binary *Tr* carbides also show superconductivity (SC) in a relatively high critical temperature (T_c). In particular, cubic δ-MoC_{1-x} possesses a T_c of 14.7K [4-8] which is in the same range of NbC (11.1K), TaC (10.35K), and WC (10.0K) [5]. This SC in binary *Tr* carbides is believed to be related to the density of states at the Fermi level, $N(E_F)$, as well as to the strong covalency of these materials [9-12].

Although δ-MoC_{1-x} was reported to have the highest T_c among the binary *Tr* carbides [4-8], magnetic and electrical data corresponding to this phase are lacking in the literature. Thus, very little is known about the nature of the SC in δ-MoC_{1-x}. A related compound such as hexagonal η-Mo_3C_2 showed a weak coupling SC with slightly anisotropic features [13,14], whereas a strong-coupled SC with a nodal gap was suggested for Mo_3Al_2C phases [15,16]. Regarding the stoichiometric cubic MoC phase, which crystallizes in a NaCl-type structure (often referred to a B1-type), calculated phonon spectra revealed that imaginary frequencies run along the high-symmetry Γ-X direction thereby suggesting a dynamical instability [10]. In addition, a pronounced anomaly in the phonon dispersion along the [100] and [110] directions was theoretically suggested for this structure [11,12]. A "double-shell" model representing the polarizability of valence (first shell) and d (second shell) electrons might account the observed phonon dispersion anomaly in MoC [11]. In addition to that, collective electron instability, as a result of a charge fluctuation between the *d* shells, was predicted to occur, although this phenomenon is usually suppressed in many materials by electron-phonon interactions [12]. The presence of anomalies in the stoichiometric MoC lattice has been pointed out as a plausible approach to further increase T_c in *Tr* carbide materials [9-12,17-23].

Synthesis of cubic MoC_{1-x} was first reported in 1961 [8]. Although several synthetic methods have appeared thereafter [4-7], important features such as the carbon nonstoichiometry and a possible order structure of the carbon vacancies still remain unexplained up to date. Besides, superconducting parameters of cubic MoC_{1-x} other than T_c seem to be unavailable in the literature. This study is thus aiming to fill this gap by focusing on the study of carbon vacancies and the superconducting properties of cubic δ-MoC_{1-x} synthesized by a high-pressure method.

3.1.1 Experimental

Polycrystalline δ-MoC_{1-x} was prepared from fine molybdenum (99.99%, ~3 μm, Kojundo Chemical Lab.) and carbon (Tokai carbon) powders. A mixture of both powders with a varying molecular ratio of Mo: C = 1: 1-x (x = 0.00, 0.05, 0.10, 0.15, 0.20, 0.25, 0.30, 0.35) is set into a flat belt-type high-pressure apparatus in which the powder mixture is heated at 2000°C for 10–30 min at an elevated pressure of 6 GPa, followed by quenching to ambient temperature before releasing the pressure. Note the heating temperatures ≤ 1700°C under 6 GPa pressure resulted in the formation of hexagonal η-Mo_3C_2 phase [13]. The as-prepared materials were structurally characterized by X-ray diffraction (XRD) at ambient condition using a monochromatic Cu-Kα radiation in an X'Pert Pro from PANalytical. A Si standard physically mixed in each sample is used to correct the zero-point shift in 2θ. A single sample (x = 0.30) is selected for further synchrotron X-ray diffraction (SXRD) studies performed by using a large Debye-Scherrer camera at the BL15XU beamline of SPring-8 (λ = 0.342259 Å and 0.65297 Å) in Japan. The solid is further studied by neutron diffraction (ND) at ambient conditions using a Ge(331) monochromatic (λ = 1.839 Å) neutron beam in a high-resolution powder diffractometer installed in the HANARO reactor at the Korea Atomic Energy Research Institute [24]. 1.6 grams of powder sample are used to collect the ND data in a 2θ range from 10° to 160° with steps of 0.05°. The crystal structure is analyzed by a Rietveld method using the program RIETAN-FP [25]. In addition, the solid material is investigated by a selected area electron diffraction (SAED) method in a transmission electron microscope (Tecnai-F20) from Philips Electron Optics, which was operated at 200 kV.

A physical properties measurement system from Quantum Design is used to measure the electrical resistivity (ρ) of the polycrystalline dense pellets at temperatures between 2 to 300K upon cooling by a four-probe method with an ac-gauge current of 10 mA

at a frequency of 110 Hz. Silver epoxy is used to fix gold wires on the pellets. The ρ vs. T measurements are performed with different magnetic field below 90 kOe. Specific heat

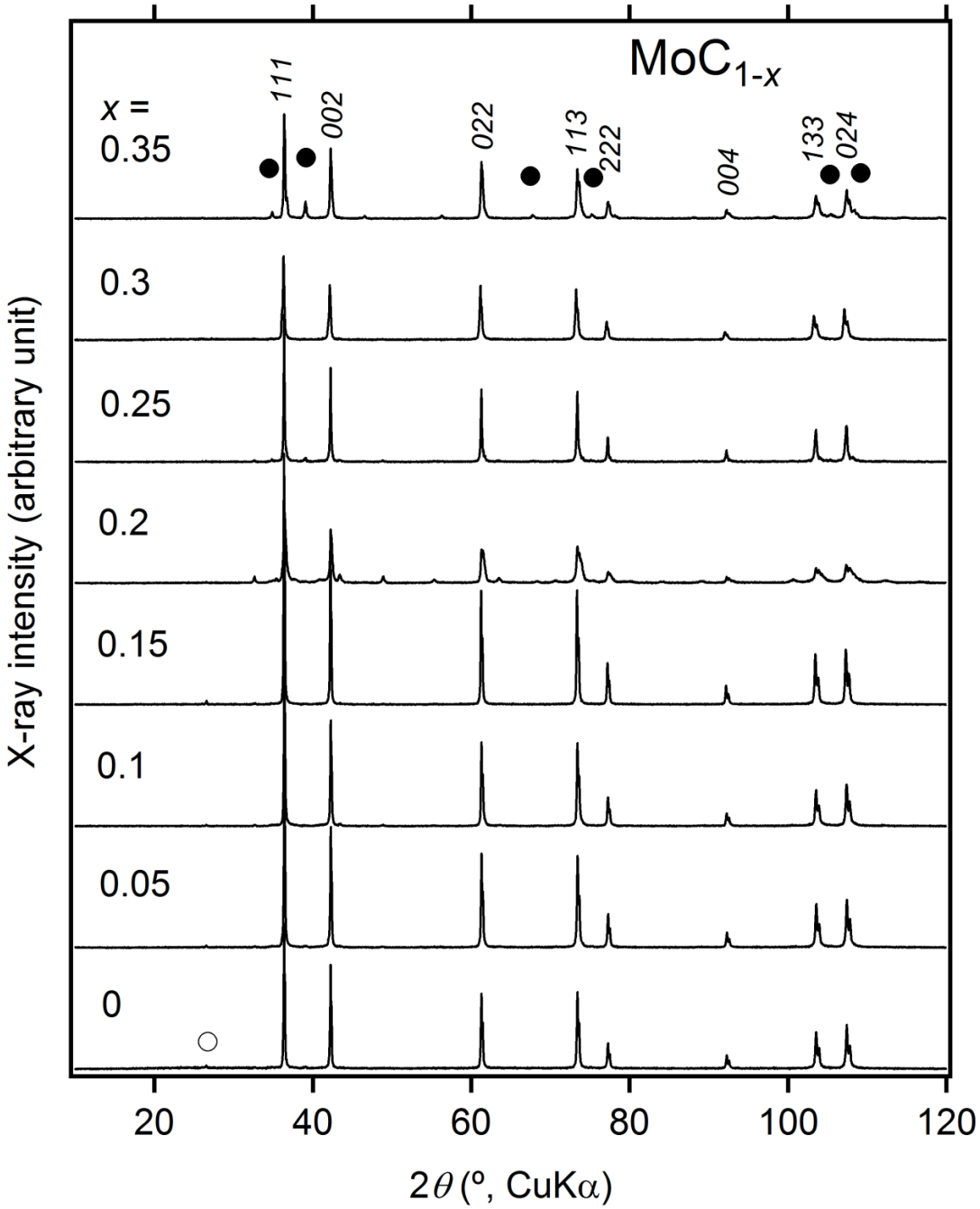

Fig.3.1.1. Powder XRD patterns from a series of MoC_{1-x} samples. Starting composition x is shown for each pattern. Characteristic peaks for the cubic Mo-C phase are labeled by the Miller indexes. Solid and open circles indicate peaks for η-Mo_3C_2 and graphite phases, respectively.

(C_p) measurements are carried out in the same apparatus with temperature range between 2

to 300K upon cooling by a quasi-adiabatic method. Magnetic susceptibility (χ) is measured in a magnetic property measurement system from Quantum Design at temperatures ranging from 2 to 30K in an applied magnetic field of 10 Oe under field-cooling (FC) and zero-field-cooling (ZFC) conditions. Isothermal magnetization between −10 kOe and 10 kOe is recorded in the same apparatus at a fixed temperature below 10 K.

3.1.2 Structural properties

The different quenched polycrystalline pellets of MoC_{1-x} shows fairly small variation in the room temperature XRD profiles, as shown in Fig.3.1.1. The major peaks of MoC_{1-x} are well characterized by assuming a cubic NaCl-type structure, as previously reported [4-8]. Small peaks corresponding to a graphite phase are detected in an expanded view of the XRD patterns, thereby suggesting that a certain amount of carbon might have been excluded from formation of the main phase. Carbon vacancies are thus likely to be accommodated in the MoC_{1-x} cubic structure. Since the graphite peaks did not offer accurate structural information, the amount of carbon excluded from the structure is indirectly

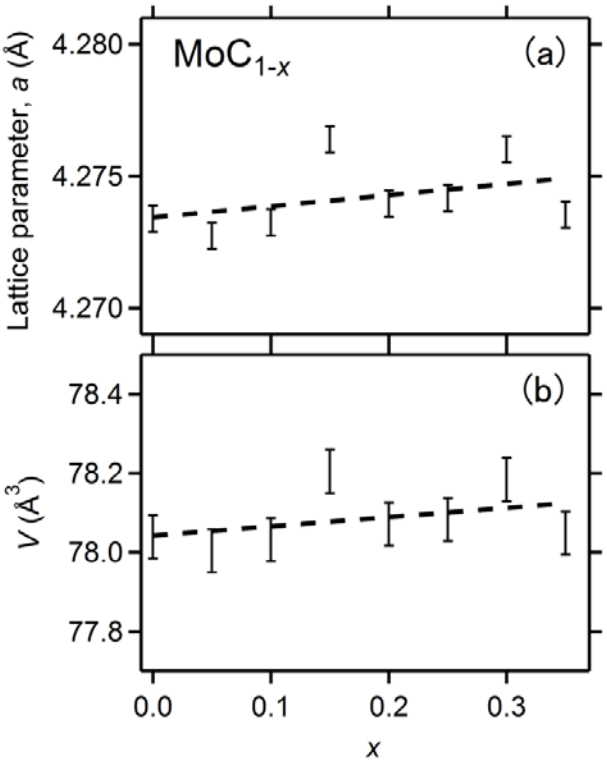

Fig.3.1.2. (a) Lattice parameter and; (b) unit-cell volume of the cubic Mo-C phase as a function of the x value.

obtained from the lattice parameter and the volume of the cubic unit cell, which were

obtained by carefully analyzing the XRD patterns as shown in Figs.3.1.2a and 3.1.2b. Both parameters did not change appreciably with starting carbon concentration. Thus, the formation of carbon vacancies in the cubic structure is seemed to be almost invariable with the starting composition. Note that the diffractograms for $x = 0.35$ sample showed additional peaks ascribed to a hexagonal phase (Fig.3.1.1), probably η-Mo_3C_2 (T_c = 7.4K) [13]. x = 0.35 seems to be the limit for the synthesis of the cubic phase.

In order to confirm this assumption, I have subjected the $x = 0.3$ sample to an electron microscopy study. The SAED patterns, projected along various directions including [001] and [110] zone-axes, as shown in Fig.3.1.3 (a-d) is revealed in a good order of diffraction spots as expected for a *Fm*-3*m* structure model [4-8] showing a lattice parameter of a = 4.27 Å. Satellite spots around the primary spots are undetected, thereby ruling out the formation of a superstructure in long range involving the carbon vacancies. Meanwhile weak streaks are seen in the zone axe [100] projection as shown in Fig.3.1.3c, suggesting a possible formation of weak order of vacancies in short range. The observation by SAED hence suggests that nearly 30% vacancies of carbon do not order in long range in the host structure.

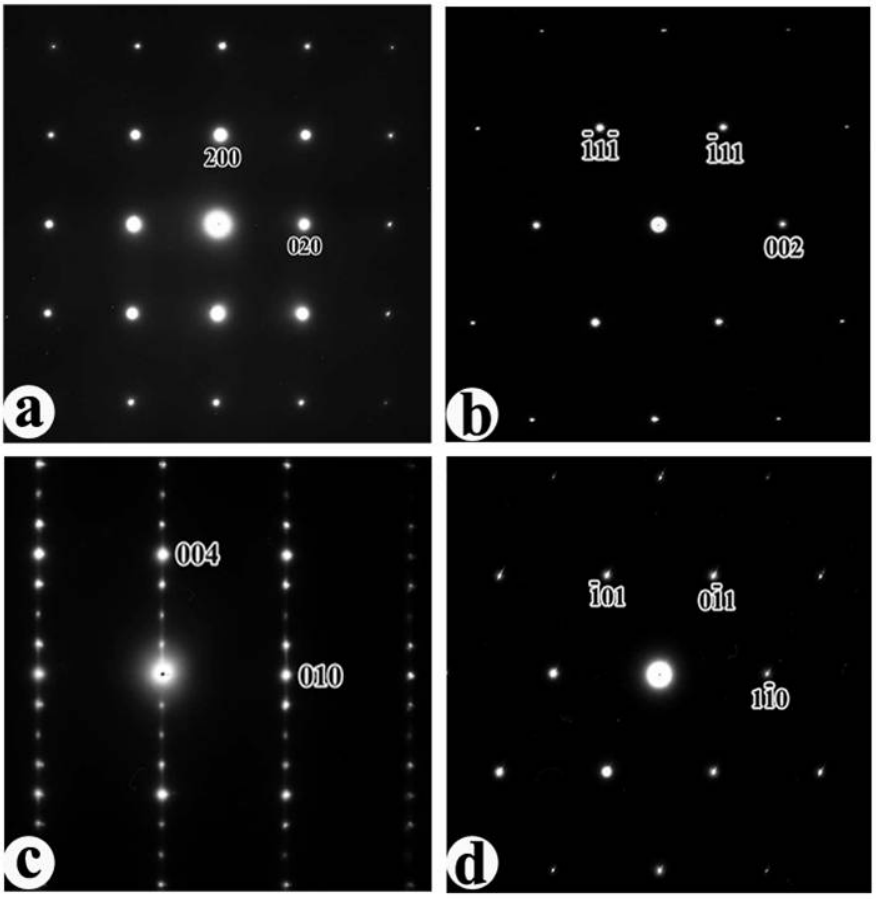

Fig.3.1.3. (a-d) SAED patterns for MoC_{1-x} taken along [0 0 1], [1 1 0], [1 0 0] and [1 1 1] zone-axes, respectively. The host structure is cubic with a lattice parameter of ~ 4.27 Å

The x = 0.3 sample is further subjected for a powder ND study conducted at ambient conditions as shown in Fig.3.1.4. The ND pattern is analyzed by a Rietveld method, and a fairly good structure solution is achieved by employing the *Fm*-3*m* structure model [4-8]. The *R* factors (a quality measure for fitting [25]) remains below 7.4% while the deviation curve between the observed and calculated profiles (see the curve at the bottom in Fig.3.1.4) is reasonably smooth. The solution summarized in Table 3.1.1 indicated reasonable thermal displacement parameters. An analysis of bond distances and angles (Table 3.1.2) indicated the absence of unusual bonding which led us to accept the model structure for the

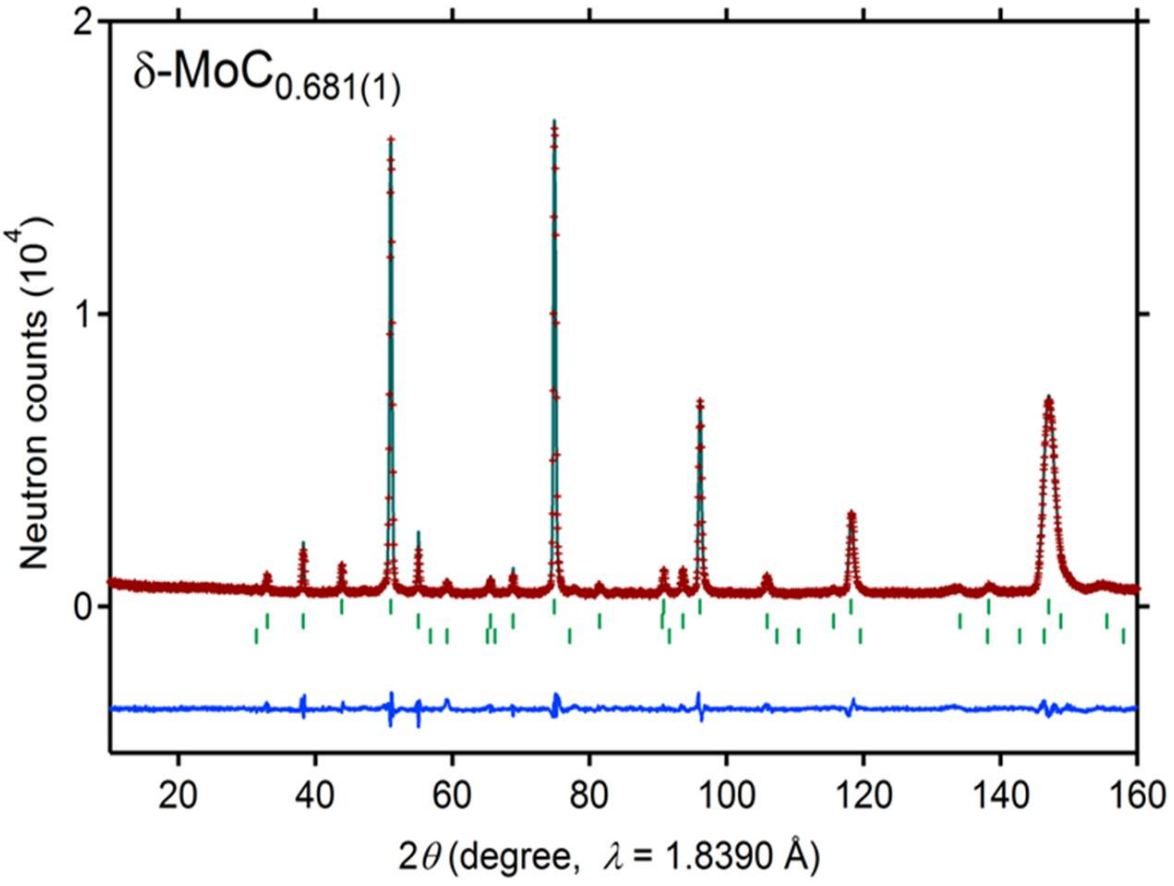

Fig.3.1.4. Powder ND profile for δ-$MoC_{0.681}$. The patterns were analyzed by a Rietveld method. The carbon concentration was determined in the ND profile analysis. Markers and solid lines show the observed and the calculated profiles, respectively, and the difference between those is shown at the bottom of each panel. Bragg positions are marked by small ticks (upper, center, and lower lines for δ-$MoC_{0.681}$, NaCl, and graphite, respectively).

sample under study. A significant consequence of the analysis is the confirmation of the imperfect carbon occupancy of the 4*b* site. In the analysis of the pattern, the site is first

assumed to be fully occupied, although this assumption led to non-acceptable solutions and the site occupancy factors are then unfixed. The refined occupancy factor indicates that the average carbon composition is 0.681(5) per Mo. Since both SAED and ND results did not provide evidence for carbon vacancies ordering, the non-trivial carbon vacancies are likely to be accommodated without forming any additional long range order in the cubic structure. In a previous ND structural study of the hexagonal η-Mo_3C_2 phase [13], multiple phases, sharing the same lattice with slightly different carbon content are found to coexist.

The coexistence is probably indicative of the local segregation because of inhomogeneous carbon distribution in the hexagonal lattice. A similar segregation model is considered in a cubic δ-$MoC_{0.681}$ phase. A similar multiple-phase model is tested in the analysis of the ND pattern for δ-$MoC_{0.681}$. However, refinement quality is not improved thereby suggesting that, unlike the hexagonal η-Mo_3C_2, the degree of segregation in δ-$MoC_{0.681}$ is fairly small. At this point, we performed room temperature SXRD experiments with x = 0.3 sample. To further investigate the local segregation model, I analyzed the sample by switching the X-ray wavelength (0.65297 Å and 0.34226 Å), as shown in Fig.3.1.5a and 3.1.5b. No evidences suggesting multiple carbon concentrations (such as peak splitting) were detected. A Rietveld analysis indicates that segregation is unlikely to occur within the cubic lattice. The total carbon content is thus finally fixed in the Rietveld analysis at 0.681 per Mo, as determined in the ND study. A schematic structural view of δ-$MoC_{0.681}$ based on the final refined structure model by ND is shown in the inset of Fig. 3.1.5b. In this structure, the Mo atoms form a face-centered–cubic sublattice while the carbon atoms randomly fill the octahedral interstitial sites. Interestingly, the interstitial carbon atoms might play a role in donating electrons into the valence or conduction bands [26].

The overall result suggests that the robust carbon vacancies are not produced by an ordered superstructure regarding but to inherent instabilities of the lattice, as suggested by theoretical studies [18]. The more critical synthesis condition may overcome the instabilities leading to a much higher T_c. In this sense, I planned to conduct a synthesis of stoichiometric δ-MoC in a Kawai-type multi-anvil high-pressure apparatus, which is capable of heating a sample under 20 GPa or higher pressures.

Table.3.1.1. Atomic coordinates, isotropic displacement parameters, and crystallographic data of δ-$MoC_{0.681}$.

Formula	$MoC_{0.681}$
Molecular weight	104.138
Temperature	room temperature
Wavelength	1.83900 Å (neutron)
Space group	*Fm*-3*m* (No. 225)
Lattice constants	a = 4.26647(9)Å, V = 77.662(3)Å^3
Z	4
Calculated density	8.907 g/cm^3
R-factors	R_{wp} = 7.363%, R_p = 5.381%, R_B = 1.815%, R_F = 1.348%, S = 2.0813
Refinement Software	RIETAN-FP

Atom	Site	x	y	z	g	B (Å^2)
Mo	4*a*	0	0	0	1	0.730(24)
C	4*b*	0.5	0.5	0.5	0.681(5)	0.503(35)

Table.3.1.2. Selected bond distances and bond angles of δ-$MoC_{0.681}$, calculated from the atomic coordinates determined in the neutron diffraction study.

Atoms	Distance (Å)	Atoms	Angle (°)
Mo-Mo	3.0168(1) [a]	C-Mo-C	180
Mo-C	2.1332(1)	C-Mo-C	90
C-C	3.0168(1)	Mo-C-Mo	180
		Mo-C-Mo	90

[a] The number in parentheses indicates a one standard deviation error.

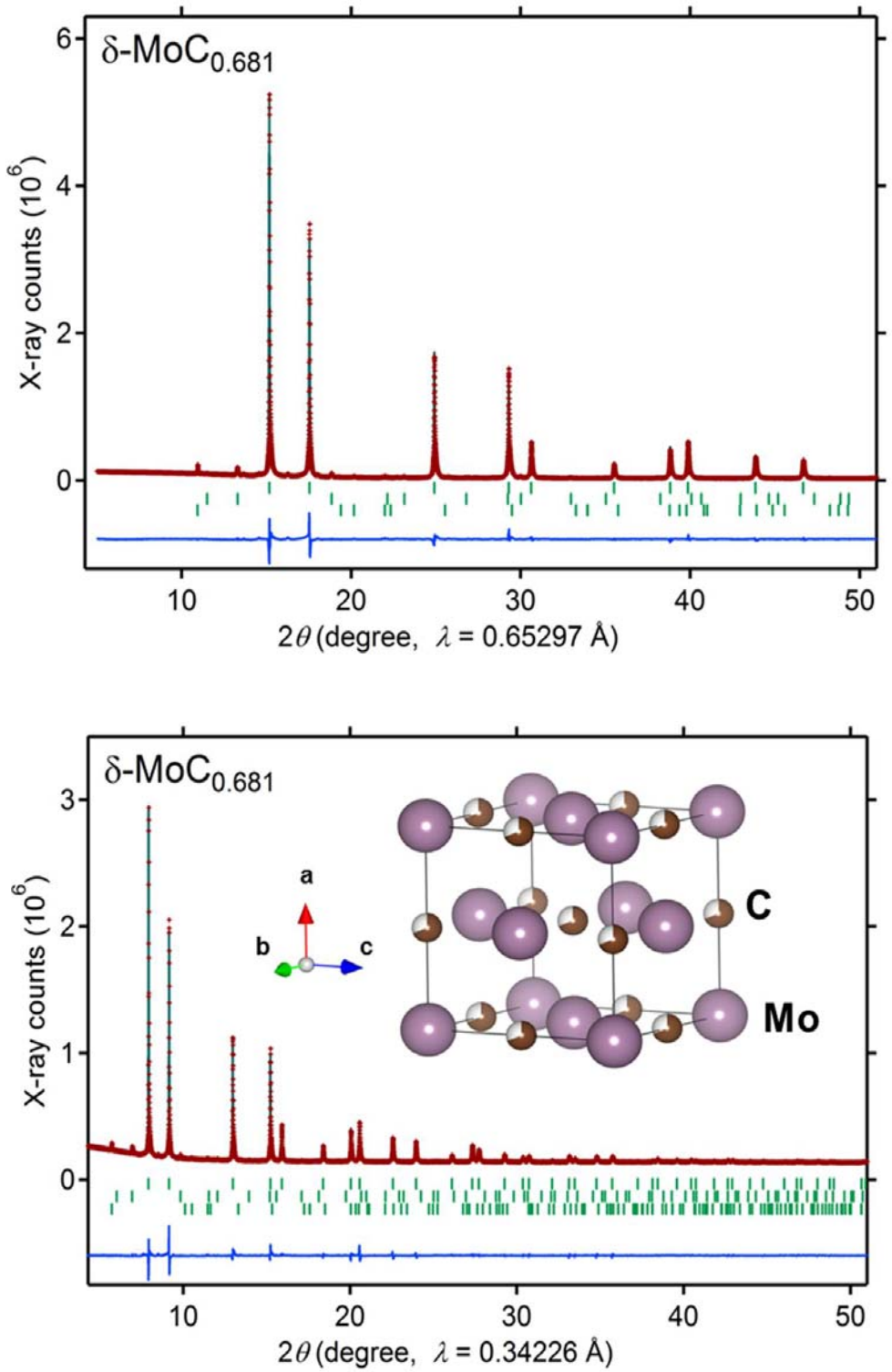

Fig.3.1.5. Powder SXRD profile for δ-$MoC_{0.681}$. (a) λ = 0.65297 Å and (b) λ = 0.34226 Å. The patterns are analyzed by a Rietveld method. The carbon concentration is fixed in this analysis. Markers and solid lines show the observed and the calculated profiles, respectively, and the difference between those is shown at the bottom of each panel. Bragg positions are marked by small ticks (upper, center, and lower lines for δ-$MoC_{0.681}$, NaCl, and graphite, respectively).

3.1.3 Magnetic properties

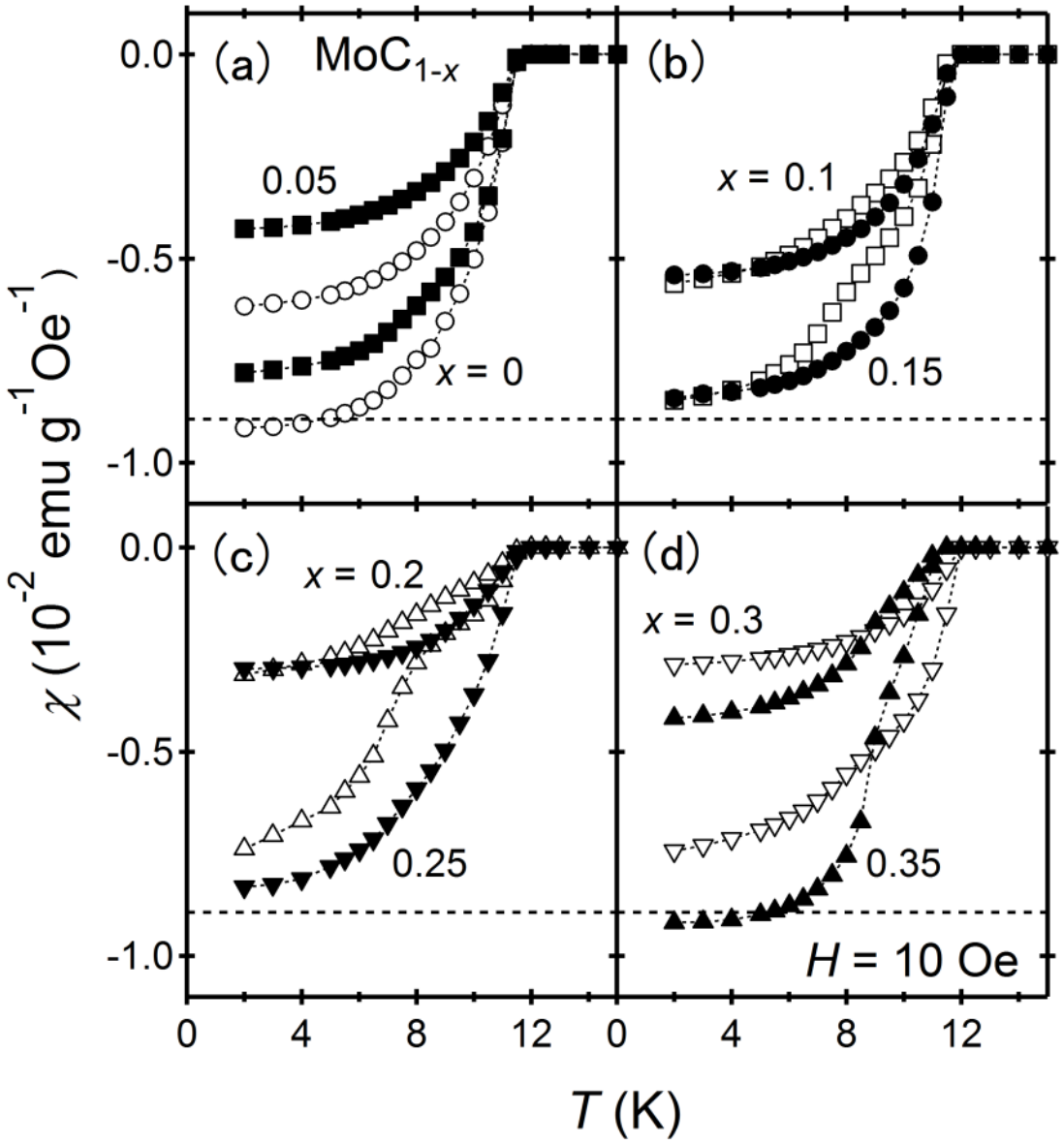

Fig.3.1.6. (a-d) T and x dependence of the magnetic susceptibility for MoC_{1-x} samples. A set of curves for each sample consists of the ZFC and FC curves measured in a magnetic field of 10 Oe. The broken line indicates a full shielding fraction calculated for a superconductor having a density of 8.907 g/cm^3

In order to study effect of the carbon vacancies on SC properties of the prepared materials, magnetic susceptibility measurements are performed by using loosely gathered powders. As shown in Fig.3.1.6a, the $x = 0$ sample showed a clear SC transition at 12K under a magnetic field of 10 Oe. The estimated shielding fraction was ca. 102% (ZFC curve) of the perfect diamagnetism while the estimated Meissner fraction was ca. 48%. Remarkably, T_c

remained almost invariable at 12K with the starting carbon concentration (see Fig. 3.1.6a–3.1.6d). The Meissner fraction, which varied from 32% to 47%, shows a slight systematic dependence with the initial carbon concentration. These results can be explained by the higher sensitivity of the Meissner fraction to uncontrolled parameters involved in the high-pressure synthesis. Since T_c, the lattice parameter, and the Meissner fraction did not show a large dependency among each other, so I have concluded that the true carbon concentration in the cubic structure is almost invariable with the starting compositions. The M vs. H curves below T_c as shown in Fig.3.1.7 clearly showed a typical behavior of a type-II superconductor.

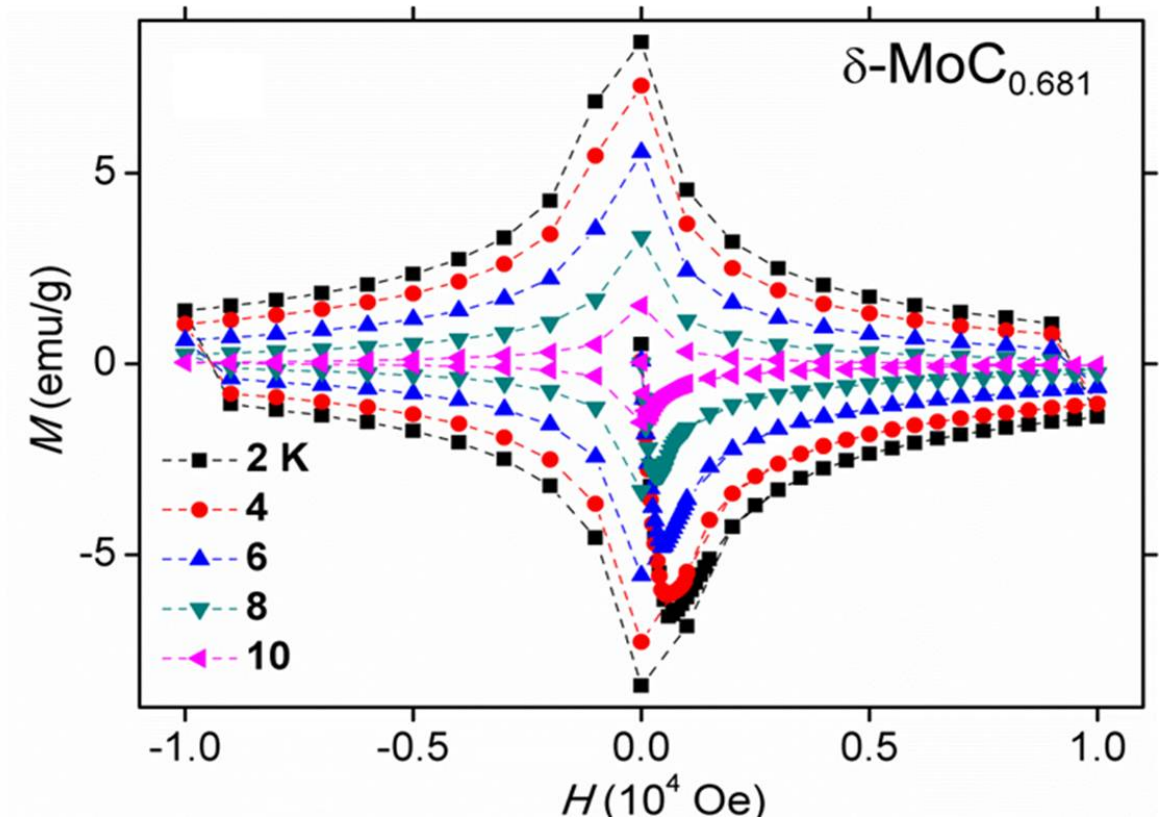

Fig.3.1.7. Isothermal magnetization curves for δ-$MoC_{0.681}$ at various temperatures below T_c.

3.1.4 Transport properties

Fig.3.1.8 shows the resistivity behaviour of a polycrystalline pellet of δ-$MoC_{0.681}$. The temperature dependence of ρ at $H = 0$ showed a sharp drop at 11.8K, indicating the onset of the superconducting transition. A zero resistivity is clearly observed with a transition width of ca. 0.4K as shown in the inset of Fig.3.1.8. The sharp drop remains even at the highest magnetic field of 90 kOe. The magnetic field dependence of the transition implies that the upper critical field (H_{c2}) is much higher than that of η-Mo_3C_2 [13]. Although the

normal-state resistivity of the polycrystalline δ-$MoC_{0.681}$ is fairly low (~95.8 μΩ cm at 300K), the residual resistivity ratio (ρ_{300K}/ρ_{12K}) is not noticeably high (ca. 1.6) thereby suggesting that grain boundaries and perhaps carbon vacancies greatly contribute to the scattering of the charge carriers.

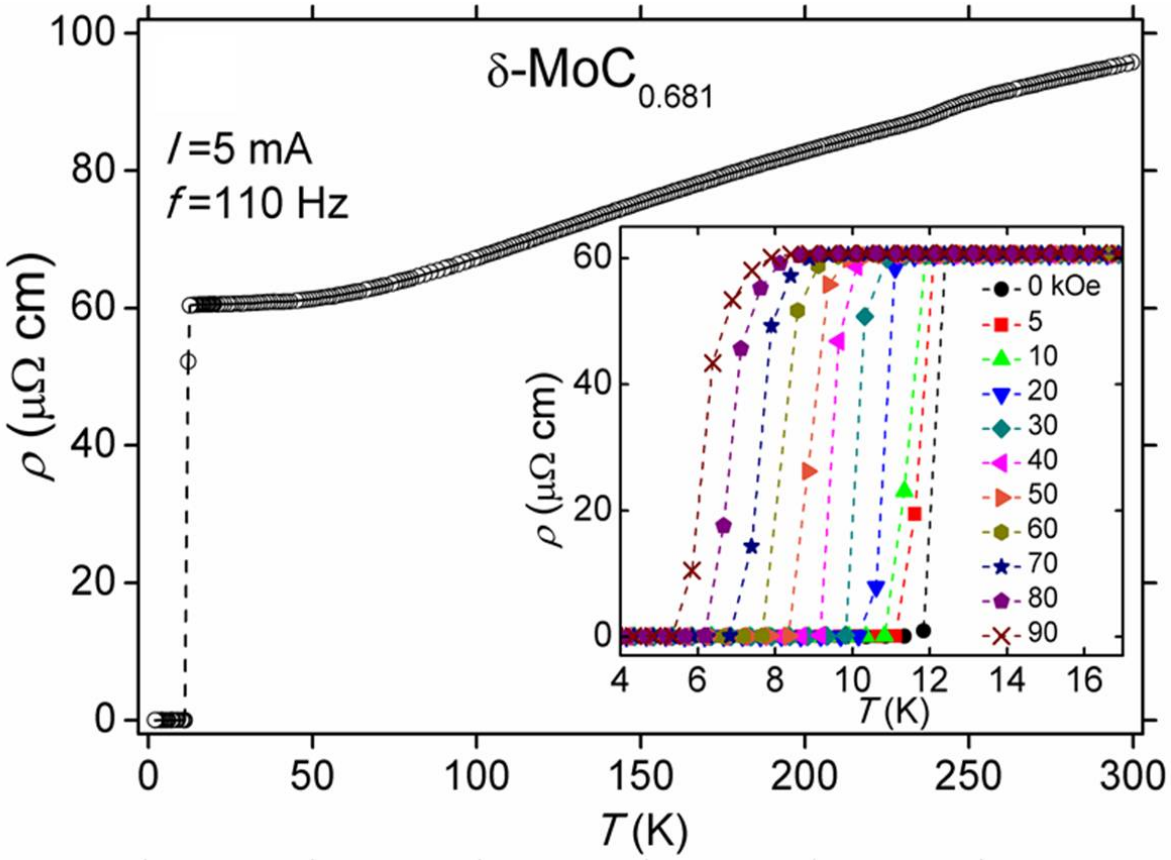

Fig.3.1.8. T dependence of ρ of a polycrystalline dense pellet of δ-$MoC_{0.681}$. Inset shows the applied magnetic field dependence of the superconducting transition

C_p/T vs. T^2 plot in the vicinity of T_c showed a clear jump as shown in Fig.3.1.9, which corresponds to the superconducting transition. The jump shifted toward lower temperatures and became lower with the intensity of applied magnetic field. Although the jump is visible even in the highest magnetic field of 90 kOe, C_p/T roughly approached to 5.0 mJ mol-Mo^{-1} K^{-2} at $T = 0$ under constrained of entropy balance between the superconducting and the normal state. The C_p/T value at $T = 0$ is not far from those of several Mo-based superconductors such as 3.93 mJ mol-Mo^{-1} K^{-2} (η-Mo_3C_2 [13]) and 5.93 mJ mol-Mo^{-1} K^{-2} (Mo_3Al_2C [16]). Assuming that the C_p/T at $T = 0$ corresponds to the Sommerfeld constant γ, $\Delta C_p/\gamma T_c$ is 1.1 (ΔC_p is estimated as shown in the inset to Fig.3.1.9), thereby suggesting that δ-$MoC_{0.681}$ is a weakly coupled superconductor as $\Delta C_p/\gamma T_c$ is close to the theoretical value of 1.43 for a weakly coupled superconductor [32].

3.1.5 Results and discussion

A decrease in T_c is shown in Fig.3.1.10 and the inset to Fig.3.1.8, which represents the effect of the magnetic field and temperature over ρ. This feature is plotted in Fig.3.1.11 with a thermodynamic transition determined in the C_p measurements (shown later). H_{c2} is estimated by analyzing the T_c decrease. To estimate the ground state value $H_{c2}(0)$, the Werthamer-Helfand-Hohenberg (WHH) relation $\mu_0 H_{c2}(T) = -0.693\mu_0 (dH_{c2}/dT)_{T=T_c} T_c$ [27] is applied to the C_p data. The obtained slope $dH_{c2}/dT \approx -1.45 \times 10^4$ Oe/K resulted in $H_{c2}(0)$ of 121 kOe. Alternatively $H_{c2}(T)$ is estimated by using a relation $H_{c2}(T) = H_{c2}(0)(1-t^2)(1+t^2)$ [6], which is effective for a weakly coupled superconductor and in which t refers to the reduced temperature of T/T_c. A $H_{c2}(0)$ value of 112 kOe is obtained which is very close to the WHH estimation. The estimated $H_{c2}(0)$ is compared with the Pauli paramagnetic limit field, H_{Pauli} [28]. Using the relation $\mu_0 H_{Pauli} = 1.24 k_B T_c / \mu_B$, H_{Pauli} is found to be 221 kOe, as this value is approximately twice than the observed $H_{c2}(0)$.

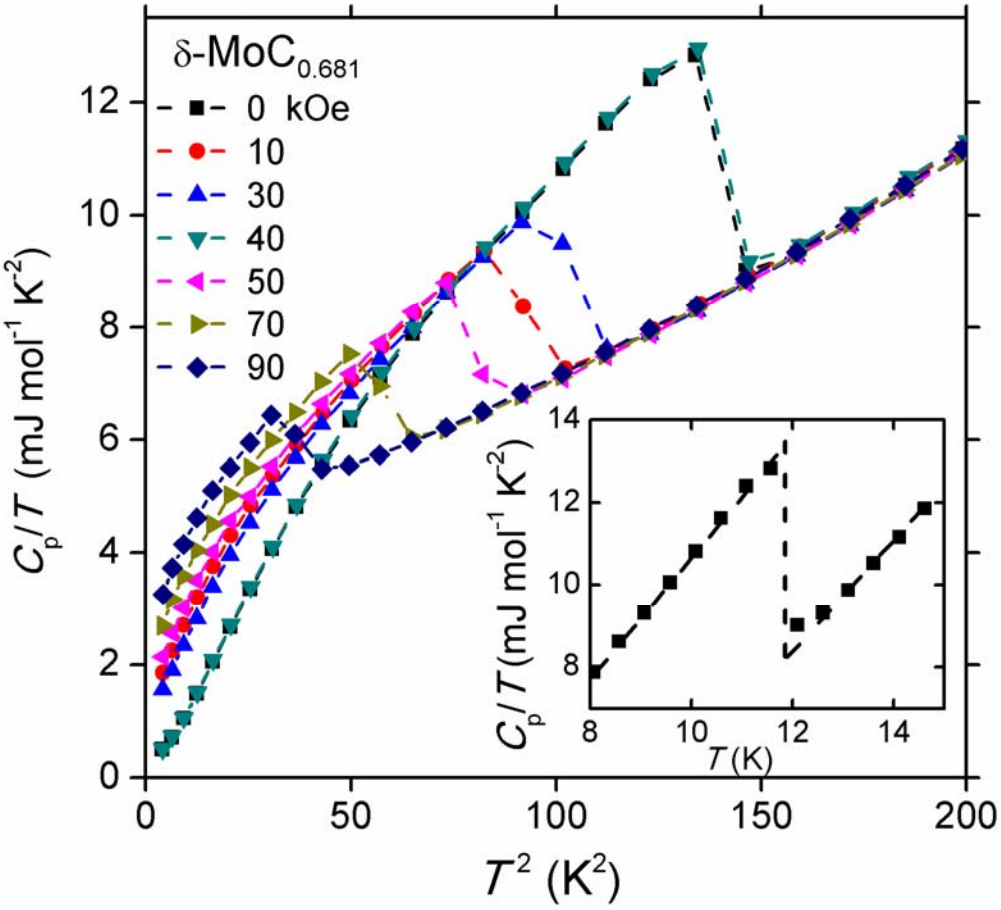

Fig.3.1.9. Applied magnetic field dependence of C_p for δ-$MoC_{0.681}$ below a temperature of 15K. (Inset) C_p/T vs. T curve showing a superconducting jump at T_c.

This results indicates that a pair-breaking effect, due to the Zeeman energy, is substantial in δ-$MoC_{0.681}$. Assuming that H_{c2} is purely orbital, the coherence length ξ_{GL} at T = 0 can be estimated from the single-band Ginzburg-Landau relation $\xi_{GL} = \sqrt{\phi_0 / 2\pi H_{c2}(0)}$, where ϕ_0 is the flux quantum [29], giving $\xi_{GL}(0)$ = 5.22 nm. The obtained $\xi_{GL}(0)$ is comparable to that of $MgCNi_3$ (4.6 nm [30]) and Mo_3Al_2C (4.25 nm [16]); and it is slightly shorter than that of η-Mo_3C_2 (7.6 nm [13]).

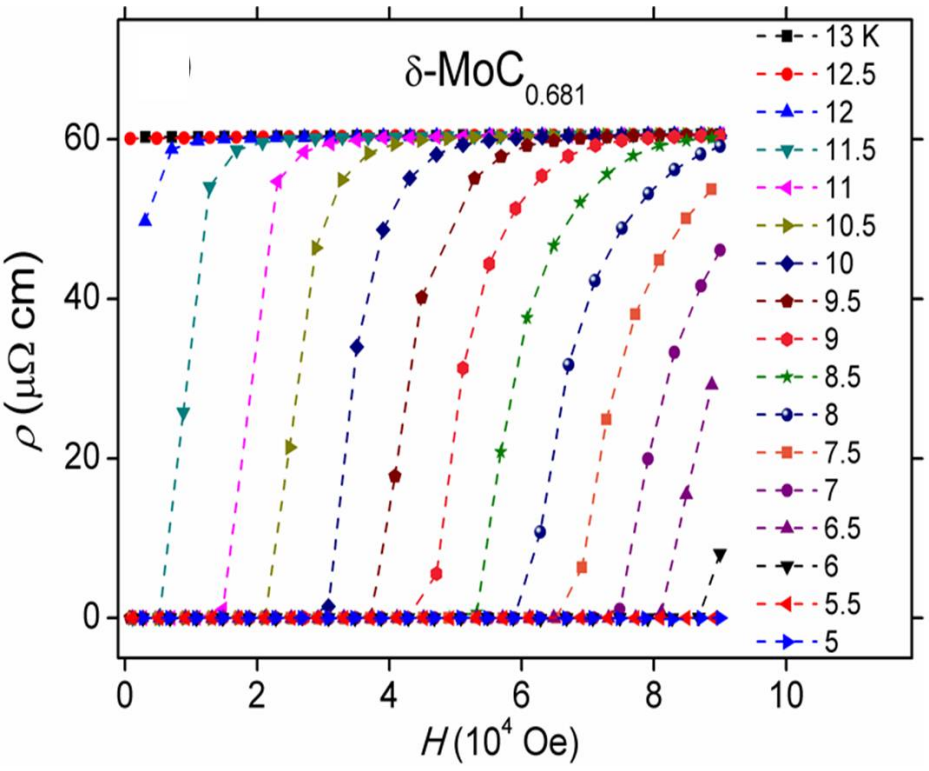

Fig.3.1.10. T variation of the ρ vs. H curves for a polycrystalline dense pellet of δ-$MoC_{0.681}$.

The M vs. H curves below T_c as shown in Fig.3.1.7 clearly shows a typical behavior of a type-II superconductor. In order to analyze the lower critical field (H_{c1}) of the superconductor, the M vs. H curve in weaker fields (e.g., below 900 Oe) is measured as shown in the inset of Fig.3.1.12. In this analysis, a magnetic field showing deviation from the broken line is herein defined as H_{c1}. The H_{c1} is plotted against T as shown in Fig.3.1.12 while a least-squares fit to the data points using $H_{c1}(T) = H_{c1}(0)(1-t^2)$ yielded a ground state value $H_{c1}(0)$ of 310 Oe [31], which is remarkably larger than that of $MgCNi_3$ (100 Oe [30]) and η-Mo_3C_2 (138 Oe) [13]. The $H_{c1}(0)$ leads to a London penetration depth $\lambda(0)$ of 132 nm

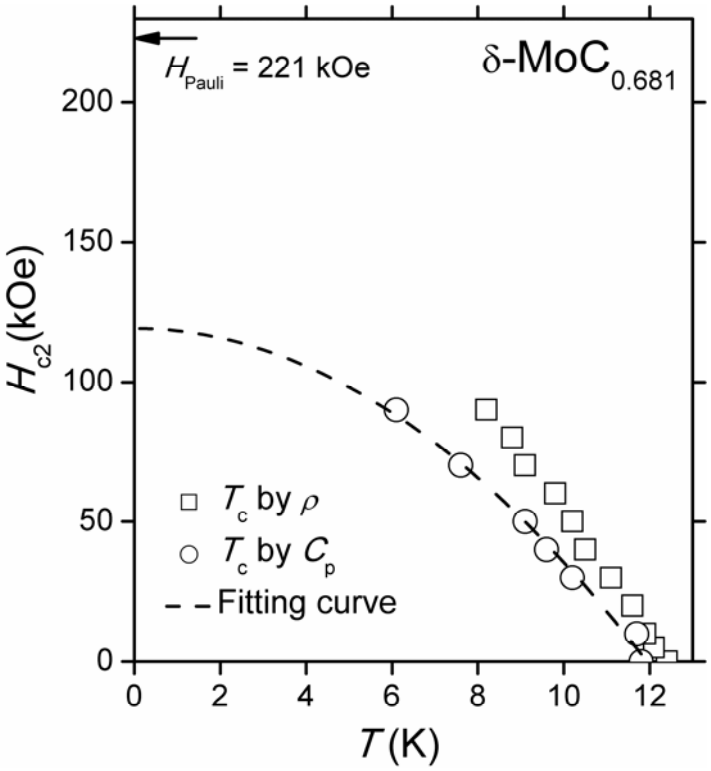

Fig.3.1.11. T dependence of H_{c2} for δ-MoC$_{0.681}$. The broken curve best fits the C_p data by a function (see the text). Pauli's limit for the superconductor is indicated by an arrow.

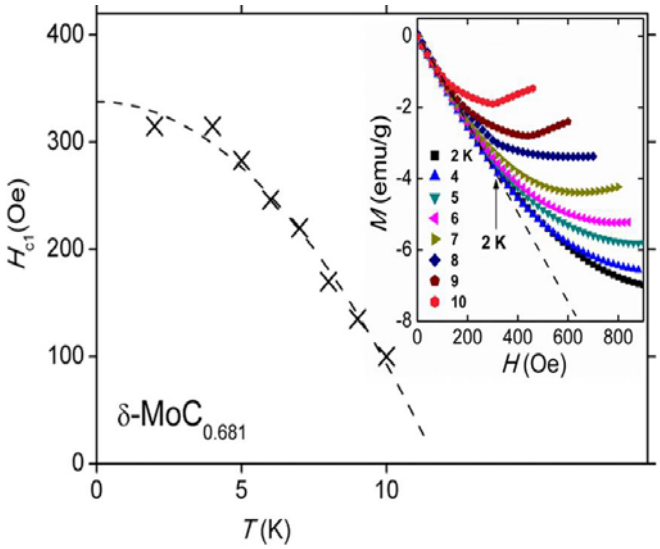

Fig.3.1.12. T dependence of H_{c1} for δ-MoC$_{0.681}$ determined by magnetization measurements as shown in the inset. The broken curve best fits the data by a function (see the text).

throughout the Bardeen-Cooper-Schrieffer formula $H_{c1}(T) = (\phi_0 / 4\pi\lambda^2)\ln(\lambda / \xi_{GL})$. The Ginzburg-Landau parameter $\kappa(0)$ ($\equiv\lambda/\xi_{GL}$) of 25 refers to a type-II superconductor. By

adopting the superconducting parameters to the relation $H_{c2}(0)H_{c1}(0) = H_c(0)[\ln\kappa + 0.08]$, which is valid when κ>>1 [31], a thermodynamically critical field $H_c(0)$ of 1.1 kOe is obtained. The superconducting parameters determined for δ-$MoC_{0.681}$ are summarized in Table 3.1.3 along with a comparison with those for related superconductors. More information about the superconducting gap structure is obtained by analyzing the decrease of C_p below T_c. In this analysis, the phonon contribution needs to be subtracted from C_p. The C_p/T vs. T^2 plot did not however follow an approximated Debye model (e.g., a linear function in the low-temperature limit) and, consequently, an empirical polynomial function is used to subtract the phonon contribution. The specific heat after the substation is herein referred to as C_{el}.

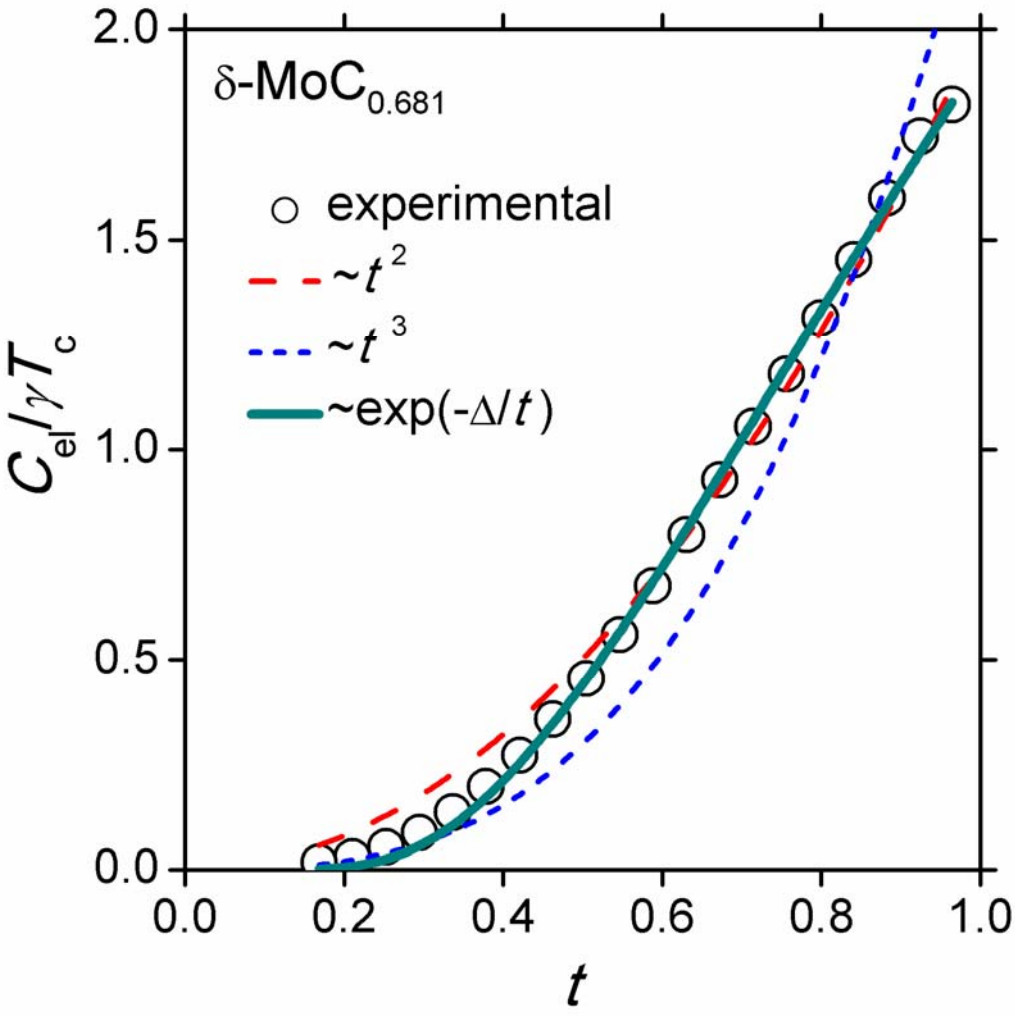

Fig.3.1.13 T dependence of the electronic specific heat C_{el} obtained by subtracting the lattice contribution from C_p. Fit to the data by several models (see text).

Table.3.1.3. Comparison of superconducting parameters of δ-$MoC_{0.681}$ and related compounds.

Parameters	Unit	δ-$MoC_{0.681}$	η-Mo_3C_2 (Ref. 13)	Mo_3Al_2C (Ref. 15,16)	$MgCNi_3$ (Ref. 30)
T_c	K	12	7.4	9.2	7.6
$H_{c1}(0)$	Oe	310	140	47	100
$H_{c2}(0)$	Oe	11.2×10^4	5.7×10^4	18.2×10^4	14.4×10^4
$\xi_{GL}(0)$	nm	5.22	7.6	4.23	4.6
$\lambda(0)$	nm	132	197	375.5	248
$\kappa(0)$		25	26	88.56	54
$\gamma(0)$	mJ mol K^{-2}	5.0	11.8	18.65	30.1
$\Delta C/\gamma T_c$		1.1		2.14	2.1
$2\Delta/k_BT_c$		2.95	2.96	4.02	4.4
λ_{ep}		1.09		0.80	0.77

Next, $C_{el}/\gamma T_c$ is plotted against T as shown in Fig.3.1.13. The γ and T_c employed for these calculations are 5.0 mJ mol-Mo^{-1} K^{-2} and 12K, respectively. The thermal evolution of $C_{el}/\gamma T_c$ below T_c is then analyzed using power law models of $\sim T^2$ and $\sim T^3$, which are expected to appear for gapless SC [16]. However, data is poorly fitted to these models (see broken curves in Fig.3.1.13. An exponential model $\sim\exp(-\Delta/k_BT)$ provided a much better data fit, where Δ corresponds to the magnitude of an isotropic gap. These results indicate that a fully gapped SC is more likely for δ-$MoC_{0.681}$ than a gapless SC. For further analysis of the implied full-gapped state, $2\Delta/k_BT_c$ is calculated, and a value of 2.95, which is slightly smaller than the universal parameter of 3.53, is obtained [33]. Note that if we employed γ of 1.9 mJ mol-Mo^{-1} K^{-2} (estimated by a linear function instead of the polynomial function) in the analysis, a γ results in $2\Delta/k_BT_c$ of 3.05 is obtained indicating that the exponential model can still provide a better fit of experimental data.

The electron-phonon coupling constant, λ_{ep}, is estimated by using the McMillian formula rather than the modified McMillian formula because the δ-$MoC_{0.681}$ is suggested to be a weakly coupled superconductor:

$$\lambda_{ep} = \frac{1.04 + \mu^* \ln(\Theta_D / 1.2T_c)}{(1 - 0.62\mu^*)\ln(\Theta_D / 1.2T_c) - 1.04},$$

where μ^* is a repulsive screened Coulomb pseudopotential and Θ_D is the Debye temperature [32]. By taking μ^* of 0.12 [3], T_c of 12K, and Θ_D of 472K (estimated by fitting to the normal state data in Fig. 3.9 using a linear function), λ_{ep} is calculated to be 0.67, indicating again that δ-$MoC_{0.681}$ is a weakly coupled superconductor [9]. Besides, $N(E_F)$ is calculated to be 0.47 states/eV per atom through the relation $\gamma = \frac{\pi^2}{3} k_B{}^2 N(E_F)(1+\lambda_{ep})$ [34], and this value is much smaller than the theoretical value for a stoichiometric cubic MoC (0.78 states/eV per atom) [35].

3.2 δ-$MoC_{0.746}$ cubic molybdenum carbide phase

Transition metal carbides are the important series of materials with interesting properties. These materials are well known for their high-tech applications and unique properties due to their extreme hardness and high melting temperatures [36-56]. There are many reports on the nonstoichiometric phases that often occur in these crystal systems [57], and due to this; they show some unusual physical properties. It also suggests that the atomic bonding between the metallic and nonmetallic atoms in the transition metal carbides are very strong and is covalent in nature [58]. Transition carbide phase show superconductivity with relatively high critical temperatures and different values of transition temperatures are reported due to the experimental difficulties in preparing a pure phase of these carbides [57]. Among this δ-MoC_{1-x} possess the highest T_c of 14.7K is reported [59-63], and no clear evidence about this phase is reported. Yamaura *et al* [64-65] have clearly reported about the synthesis, structure and physical properties of hexagonal η-Mo_3C_2 phase and reported a transition temperature of 7.4K by using the high-pressure and high temperature (*HPHT*) synthesis. In my previous report, a transition temperature of 12K in cubic δ-$MoC_{0.681}$ phase with the structural properties and physical properties of this phase is reported in detail for the first time using the *HPHT* synthesis method. I also reported that the carbon vacancies in the cubic structure were robust, the vacancies are unlikely to be ordered in long range, and the inherent phonon instability might be responsible for the robust vacancies in this phase. In order to overcome this issue some critical synthesis conditions are necessary. In the previous report, cubic δ-$MoC_{0.681}$ phase is synthesized using the *HPHT* under a pressure of 6 GPa, and so I further tried for a higher pressure to reduce the vacancies using the Kawai-type multi-anvil high-pressure apparatus. In this work, I report the successive synthesis of δ-$MoC_{0.746}$, studied the structure of this phase using the synchrotron x-ray diffraction, and bulk properties

such as electrical transport and magnetic properties are studied in detail.

3.2.1 Experimental:

A Polycrystalline sample of δ-$MoC_{0.746}$ is prepared by mixing fine powders of pure Molybdenum (99.9% ~ 3μm, Konjundo Chemical Lab.) and Carbon (Tokai carbon). A mixture of both powders is pressed into a pellet and placed in a pre-prepared pyrophyllite sample cell and heated to 1800°C under a pressure of 17 GPa in a Kawai-type multi-anvil high-pressure apparatus and quenched to ambient temperature before releasing pressure. The as-prepared compounds are investigated by X-ray diffraction (XRD) under ambient conditions in an RIGAKU system using monochromatic Cu-Kα radiation. θ. A single sample (x = 0.75) is selected for further synchrotron X-ray diffraction (SXRD) studies performed by using a large Debye-Scherrer camera at the BL15XU beamline of SPring-8 (λ = 0.65297 Å) in Japan. Magnetic susceptibility (χ) measurements are performed using a magnetic property measurement system (Quantum Design) in the temperature range 2–16K at an applied magnetic field of 10 Oe, under field-cooling (FC) and zero-field-cooling (ZFC) conditions. The electrical resistivity (ρ) of the polycrystalline pellets is measured by a physical property measurement system (Quantum Design) at temperatures between 2 to 300K. The conventional four-terminal method is used for this purpose; the ac-gauge current and frequency are 5 mA and 110 Hz, respectively. Silver epoxy is used to fix gold wires onto the pellets for the resistivity measurements. Specific heat measurements are also carried out for a piece of sample in the same instrument at temperature between 2 to 300K using a standard thermal relaxation method also by varying the magnetic field.

3.2.2 Structural properties

The polycrystalline pellet quenched under the high-pressure condition is subjected to room temperature XRD and a clear cubic MoC phase is identified. In order to know the exact structure, I have performed room temperature Synchrotron XRD experiments and analyzed the sample by switching the X-ray wavelength to 0.65297 Å as shown in Fig.3.2.1. A Rietveld analysis was carried out and the best solution is attained using a structural model with space group *Fm*-3*m* (No. 225).There were no evidences detected for peak splitting or multiple carbon concentrations. So for each Mo site the total carbon content is fixed at 0.746 in Rietveld analysis. The observed and calculated profiles as shown in the bottom of Fig.3.2.1 were very smooth reasonably, R indexes remained below 6.8%, and this

measure shows a good fitting with the profile. From the refinement, thermal displacement parameters are summarized in Table.3.2.1 and it shows reasonable values with good fitting. To know further, the bond distances and angles are measured and shown in Table.3.2.2, and this indicates the absence of unusual bonding and is comparable with that of the previously reported one. The noticeable thing here is, distance between Mo-Mo is noticed as 3.0493(1) Å that is slightly bigger than Mo-Mo distance in the previously reported phase, of δ-$MoC_{0.681}$ i.e. 3.0168(1) Å. As such the distance between Mo-C and C-C also increased consistenly as 2.1562(1) Å & 3.0168(1) Å. While comparing these bond distances with the lattice parameters, it shows a good comparison and this raise in lattice constants and bond distances from the previous report promote there will be some change in the physical properties of δ-$MoC_{0.746}$ phase.

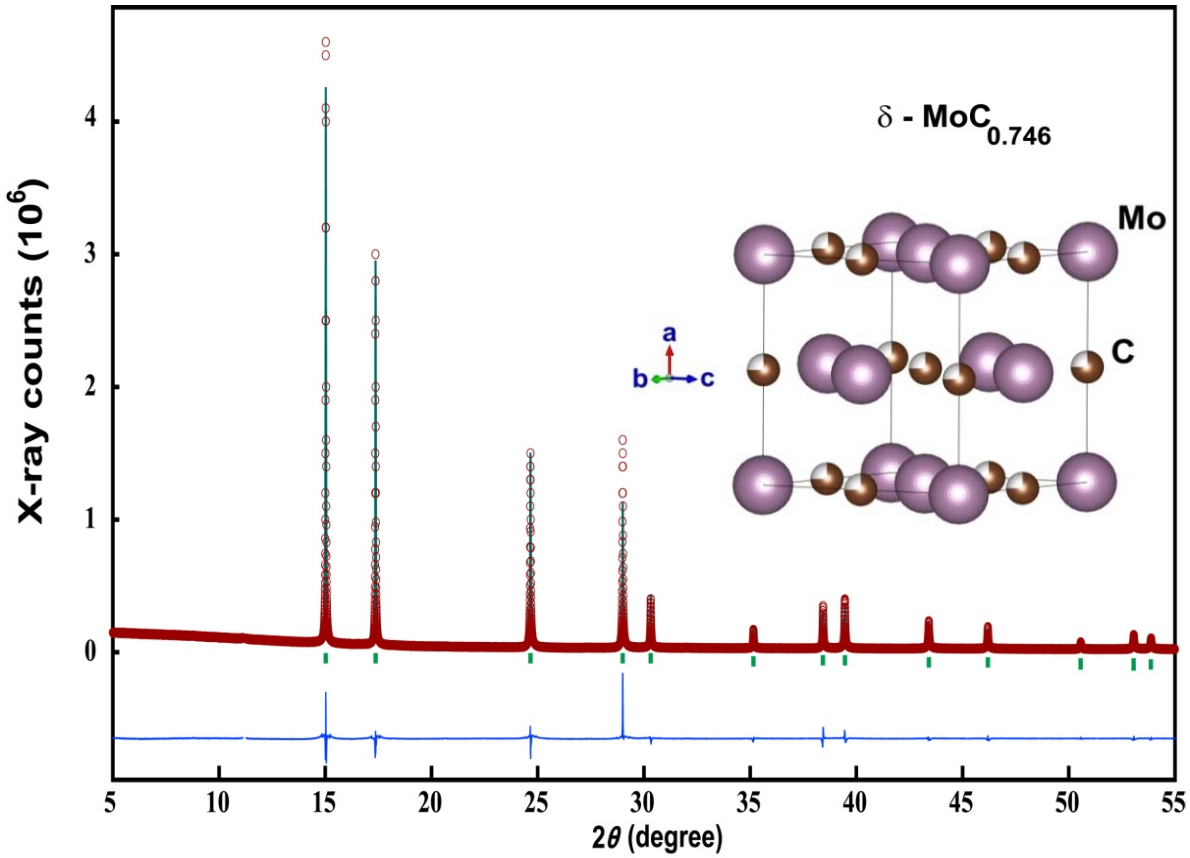

Fig.3.2.1. Powder SXRD profile for δ-$MoC_{0.746}$. λ = 0.65297 Å. The patterns are analyzed by a Rietveld method. Markers and solid lines show the observed and the calculated profiles, respectively, and the difference between those is shown at the bottom of each panel. Small ticks mark Bragg positions.

Table.3.2.1. Atomic coordinates, isotropic displacement parameters, and crystallographic data of δ-$MoC_{0.746}$.

Formula	$MoC_{0.746}$
Molecular weight	104.920
Temperature	room temperature
Wavelength	0.65297 Å (Synchrotron x-ray)
Space group	*Fm*-3*m* (No. 225)
Lattice constants	a = 4.31237(2)Å, V = 80.1951(3)Å^3
Z	4
Calculated density	8.689 g/cm^3
R-factors	R_{wp} = 6.798%, R_p = 4.402%, R_B = 7.480%, R_F = 2.512%, S = 16.9592
Refinement Software	RIETAN-FP

Atom	Site	x	y	z	g	B (Å^2)
Mo	4*a*	0	0	0	1	0.819(3)
C	4*b*	0.5	0.5	0.5	0.7460(1)	0.500(4)

Table.3.2.2. Selected bond distances and bond angles of δ-$MoC_{0.746}$, calculated from the atomic coordinates determined in the neutron diffraction study.

Atoms	Distance (Å)	Atoms	Angle (°)
Mo-Mo	3.0493(1)	C-Mo-C	180
Mo-C	2.1562(1)	C-Mo-C	90
C-C	3.0493(1)	Mo-C-Mo	180
		Mo-C-Mo	90

3.2.3 Magnetic properties

Superconducting properties of the so refined δ-$MoC_{0.746}$ phase is studied in detail. Magnetic susceptibility measurements clearly showed a superconducting transition (T_c) at 14.3K under an applied magnetic field of 10 Oe and the shielding fraction is calculated to be

~ 130 % as shown in Fig.3.2.2. There is an increase in T_c when compared with the previous report (T_c = 12K), and is very comparable with that of the previously reported highest T_c [59-63], among the MoC phase. The sample preparation under extreme high-pressure condition i.e. 17 GPa shows an increase in the bond distance & volume and this might be the reason for the increase in T_c is predicted. In addition, there is an increase in the total carbon content for each Mo site and the vacancies also decreases consistently when compared with the previously reported δ-$MoC_{0.681}$. Due to the limitations in preparing enormous amount of samples under extreme high-pressure conditions, the studies carried are limited and so the isothermal magnetic measurements is omitted.

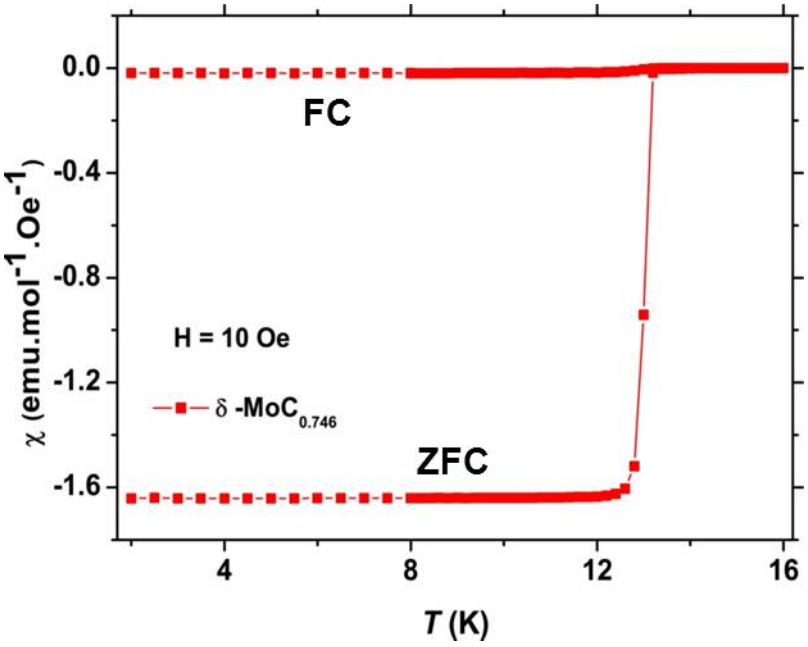

Fig.3.2.2. Temperature dependence of Magnetic susceptibility δ-$MoC_{0.746}$ sample measured in a magnetic field of 10 Oe in ZFC and FC mode.

3.2.4 Transport properties

To compare the superconducting properties of δ-$MoC_{0.746}$ sample transport property measurements are carried out. The temperature dependence of electrical resistivity is measured between 2 to 300K at H = 0 showed a sharp drop at 14.3K indicates the superconducting temperature and clearly shows a zero resistivity with a transition width of ca. 0.4K as shown in Fig.3.2.3. The sharp drop to zero at T_c shows a good sample quality and the normal state resistivity of δ-$MoC_{0.746}$ is low ~ 15.7 mΩ cm at 300K. The resistivity measurement with a T_c of 14.3K is well comparable with that of the superconducting transition from the magnetic susceptibility measurements. The temperature dependence of

specific heat measured between the temperatures of 2 to 300K at $H = 0$ showed a sharp jump at 13.7K as shown in Fig.3.2.4. The inset of Fig.3.2.4 shows the extrapolated view of the jump. By using the normal values and estimating a fit that yields the value $\gamma = 7.48$ mJ mol^{-1} K^{-2} , $\beta = 0.04583$mJ mol^{-1} K^{-4} and ΔC_p is estimated from the jump at T_c as 10.7mJ mol^{-1} K^{-2}, $\Delta C_p/\gamma T_c$ is 1.01 which is smaller than the theoretical value of 1.43 predicted by BCS for a weakly coupled superconductor [20]. From the above values of γ and β we estimated the Debye temperature $\Theta_D \sim 874$K using the expression $\beta = N(12/5)\pi 4R\Theta_D^{-3}$, (where $R = 8.314$ J mol^{-1} K^{-1}).

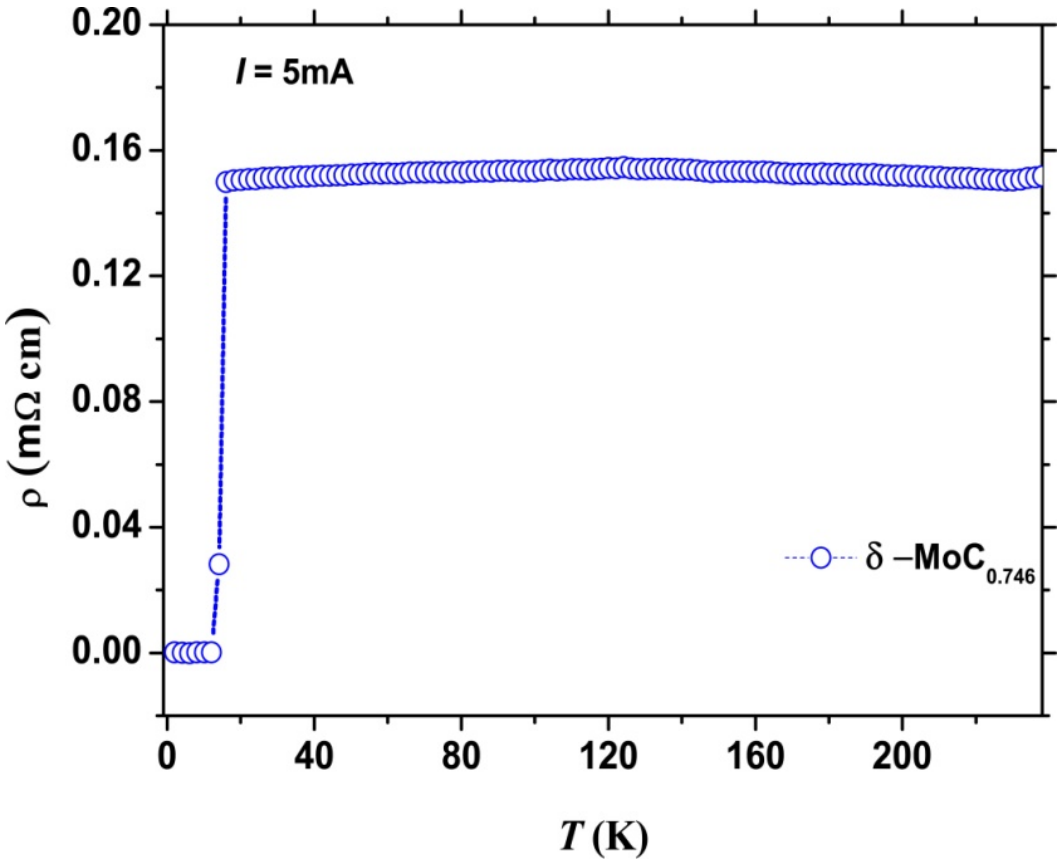

Fig.3.2.3. Temperature dependence of resistivity for δ-$MoC_{0.746}$ sample

Finally, to reconfirm the weak coupling superconductive nature in δ-$MoC_{0.746}$ sample, the electron-phonon coupling constant λ_{ep}, is estimated by using the McMillian formula, because the above studies in δ-$MoC_{0.746}$ suggested being a weakly coupled superconductor and was also comparable with the previous report:

$$\lambda_{ep} = \frac{1.04 + \mu^* \ln(\Theta_D / 1.2T_c)}{(1 - 0.62\mu^*)\ln(\Theta_D / 1.2T_c) - 1.04},$$

Where μ^* is a repulsive screened Coulomb pseudopotential and Θ_D is the Debye temperature

[32]. Considering the value of μ^* as 0.12 given elsewhere [3], the transition temperature (T_c) of δ-$MoC_{0.746}$ as 14.3K, and Θ_D of 874K (estimated by fitting to the normal state data in Fig.3.2.4 using a linear function), λ_{ep} is calculated to be 0.62, indicating again that δ-$MoC_{0.746}$ is a weakly coupled superconductor. Electron density of states at the Fermi energy $N(E_F)$ is calculated using the relation $\gamma = \frac{\pi^2}{3} k_B{}^2 N(E_F)(1+\lambda_{ep})$ [34], to be 0.33 states/eV per atom and this value is much smaller when compared with theoretical value for a stoichiometric cubic MoC (0.78 states/eV per atom) [35].

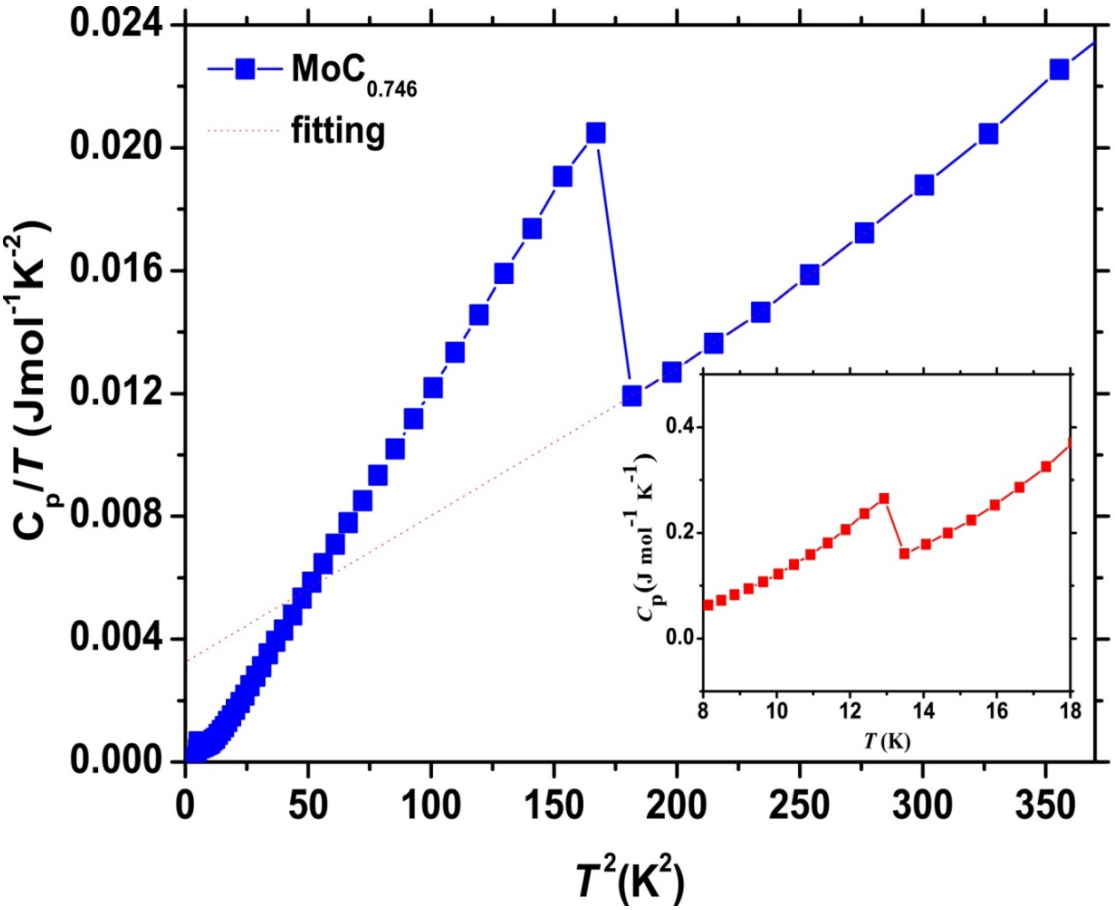

Fig.3.2.4. *T* dependence of the electronic specific heat

3.3 Conclusion

In summary, the superconducting and structural properties of δ-$MoC_{0.681}$ and δ-$MoC_{0.746}$ have been studied using a high-quality polycrystalline sample by synchrotron X-ray and δ-$MoC_{0.681}$ by neutron and electron diffraction methods as well as electromagnetic measurements. The superconducting properties of δ-$MoC_{0.681}$ and δ-$MoC_{0.746}$ are well characterized by a weak coupling model. The carbon vacancies in the host cubic structure are

robust although the material is synthesized under a high-pressure condition of 6 GPa and 17 GPa in the case of δ-$MoC_{0.681}$ and δ-$MoC_{0.746}$. Because the vacancies are unlikely to be ordered in the host structure, a thermodynamically stable structure model with carbon vacancies ordering did not account for the robust carbon vacancies in δ-$MoC_{0.681}$ and δ-$MoC_{0.746}$. Instead, the inherent phonon instability, theoretically predicted for the stoichiometric MoC, might be responsible for the robust carbon vacancies of δ-$MoC_{0.681}$ and δ-$MoC_{0.746}$. Further critical synthesis conditions are necessary to overcome the vacancy issue, thereby allowing the achievement of a much higher T_c, which is expected for the stoichiometric δ-MoC.

References

[1] C. S. Barrett, and T. B. Massalski, *Structure of Metals*, 3rd rev. ed., Pergamon, New York, 1980.

[2] H. Bilz, Z. Phys. **153**, 338–358 (1958).

[3] E. I. Isaev, S. I. Simak, I. A. Abrikosov, R. Ahujia, Y. K. Vekilov, M. I. Katsnelson, A. I. Lichtenstein, and B. Johansson, J. Appl. Phys. **101**, 123519–123536 (2007).

[4] N. S. Athanasiou, Mod. Phys. Lett. **B 11**, 939–947 (1997).

[5] R. H. Willens, E. Buehler, and B. T. Matthias, Phys. Rev. **159**, 327–330 (1967).

[6] L. E. Toth, R. Rudy, J. Johnston, and R. Parker, J. Phys. Chem. Solids. **26**, 517–522 (1965).

[7] A. L. Giorgi, E. G. Szklarz, E. K. Storms, A. L. Bowman, and B. T. Matthias, Phys. Rev. **125**, 837–838 (1962).

[8] E. V. Clougherty, K. H. Lothrop, and J. A. Kafalas, Nature. **191**, 1194 (1961).

[9] E. I. Isaev, R. Ahuja, S. I. Simak, A. I. Lichtenstein, Y. K. Vekilov, B. Johansson, and I. A. Abrikosov, Phys. Rev. B. **72**, 064515–064519 (2005).

[10] G. L. W. Hart, and B. M. Klein, Phys. Rev. B. **61**, 3151–3154 (2000).

[11] H. G. Smith, Phys. Rev. Lett. **29**, 353–354 (1972).

[12] H. G. Smith, and W. Gläzer, Phys. Rev. Lett. **25**, 1611–1613 (1970).

[13] K. Yamaura, Q. Huang, M. Akaishi, and E. Takayama-Muromachi, Phys. Rev. B. **74**, 184510–184515 (2006).

[14] K. Yamaura, Q. Huang, and E. Takayama-Muromachi, Physica C. **468**, 1135–1137

(2008).

[15] E. Bauer, G. Rogl, X.Q. Chen, R. T. Khan, H. Michor, G. Hilscher, E. Royanian, K. Kumagai, D. Z. Li, Y.Y. Li, R. Podloucky, and P. Rogl, Phys. Rev. B. **82**, 064511–064515 (2010).

[16] A. B. Karki, Y. M. Xiong, I. Vekhter, D. Browne, P. W. Adams, and D. P. Young, Phys. Rev. B. **82**, 064512–064518 (2010).

[17] V. Heine and I. Abarenkov, Philos. Mag. **9**, 451–465 (1964).

[18] L. Pintschovius, W. Reichard, and B. Scheerer, J. Phys. C. **11**, 1557–1562 (1978).

[19] M. Klein, J. A. Holy, and W. S. Williams, Phys. Rev. B. **17**, 1546–1556 (1978).

[20] K. S. Upadhyaya, A. K. Singh, A. Pandey, S. N. Pathak, A. K. Singh, and Pramana, J. Phys. **64**, 299–304 (2005).

[21] J. C. Phillips, Phys. Rev. Lett. **26**, 543–546 (1971).

[22] H. Frölich, Phys. Lett. A. **35**, 325–326 (1971).

[23] H. R. Zeller, Phys. Rev. B. **5**, 1813–1817 (1972).

[24] C.-H. Lee, V. Em, M.-K. Moon, K.-P. Hong, J.-K. Cheon, Y.-H. Choi, U.-W. Nam, and K.-N. Kong, Physica B: Cond. Matter. **385–386**, 1016–1018 (2006).

[25] F. Izumi and K. Momma, Solid State Phenom. **130**, 15–20 (2007).

[26] L. E. Toth, *Transition Metal Carbides and Nitrides*, Academic Press, New York, London, 1971.

[27] N. R. Werthamer, E. Helfand, and P. C. Hohenberg, Phys. Rev. **147**, 295–302 (1966).

[28] K. Maki, Phys. Rev. **148**, 362–369 (1966).

[29] E. H. Brandt, Phys. Rev. B. **37**, 2349–2352 (1988).

[30] Z. Q. Mao, M. M. Rosario, K. D. Nelson, K. Wu, I. G. Deac, P. Schiffer, Y. Liu, T. He, K. A. Regan, and R. J. Cava, Phys. Rev. B. **67**, 094502–094506 (2003).

[31] J. P. Carbotte, Rev. Mod. Phys. **62**, 1027–1157 (1990).

[32] E. H. Brandt, Phys. Rev. B. **60**, 11939–11942 (1999).

[33] J. Bardeen, L. N. Cooper, and J. R. Schrieffer, Phys. Rev. **108**, 1175–1204 (1957).

[34] C. Kittel, *Introduction to Solid State Physics*, fourth ed., Wiley, New York, 1966.

[35] W. Weber, Phys. Rev. B. **8**, 5093–5097 (1973).

[36] E. Furimsky, Applied Catalysis A: General. **240**, 1-28 (2003).

[37] C. Kral, W. Lengauer, D. Rafaja, and P. Ettmayer, J. Alloy. Comp. **265**, 215-233 (1998).

[38] A.-M. Alexander, and J.S.J. Hargreaves, Chem. Soc. Rev. **39**, 4388-4401 (2010).

[39] G. Vitale, M.L. Frauwallner, E. Hernandez, C.E. Scott, and P. Pereira-Almao, Applied Catalysis A: General, (2011).

[40] C. C. Yu, S. Ramanathan and S.T. Oyama, Journal of Catalysis. **173**, 1-9 (1998).

[41] S. Wang, X. Wang, Z. Zhang, and Y. Qian, J. Mater. Sci, **38**, 3473- 3478 (2003).

[42] P. Liu, and J. A. Rodriguez, J. Chem. Phys. **120**, 5414 (2004).

[43] J. C. Grossman, A. Mizel, M. Côté, M.L. Cohen, and S.G. Louie, Phys. Rev. B. **60**, 6343-6347 (1999).

[44] J. S. Lee, *Metal Carbides*, in: Encyclopedia of Catalysis, John Wiley & Sons, Inc., 2002.

[45] J. S. Lee, and D. J. Ham, *Metal Nitrides*, in: Encyclopedia of Catalysis, John Wiley & Sons, Inc., 2002.

[46] L. I. Johansson, Surf. Sci. Rep. **21**, 177-250 (1995).

[47] S. T. Oyama, *The chemistry of Transition Metal Carbides and Nitrides*, First ed.,

[48] Blackie Academic & Professional, Glasgow, 1996.

[49] J. G. Chen, Chem. Rev. **96**, 1477-1498 (1996).

[50] S. T. Oyama, J. Sol. Sta. Chem. **96**, 442-445 (1992).

[51] P. Ettmayer, Ann. Rev Mat. Sci. **19**, 145-164 (1989).

[52] L. Volpe, and M. Boudart, J. Sol. Stat. Chem. **59**, 332-347 (1985).

[53] S. T. Oyama, J.C. Schlatter, J.E. Metcalfe III, and J.M. Lambert Jr, Ind. & Eng. Chem. Res. **27**, 1639-1648 (1988).

[54] R. Marchand, F. Tessier, and F. J. DiSalvo, J. Mater. Chem. **9**, 297-304 (1999).

[55] A. G. Cairns, J.G. Gallagher, J.S.J. Hargreaves, D. McKay, E. Morrison, J.L. Rico, and K. Wilson, J. Alloy. & Comp. **479**, 851-854 (2009).

[56] S. T. Oyama, Cat. Today. **15**, 179-200 (1992).

[57] L. E. Toth,V. F. Zackay, M. Wells, J. Olsan, and E. R. Parker, Acta Metallurgica. **13**, 379-385 (1965).

[58] E. I. Isaev, S. I. Simak & I. A. Abrikosov, R. Ahuja, Y. K. Vekilov, M. I. Katsnelson, A.

I. Lichtenstein, and B. Johansson, J. App. Phys. **101**, 123519 (2007).

[59] N. S. Athanasiou, Mod. Phys. Lett. **B 11**, 939–947 (1997).

[60] R.H. Willens, E. Buehler, and B.T. Matthias, Phys. Rev. **159**, 327–330 (1967).

[61] L. E. Toth, R. Rudy, J. Johnston, and R. Parker, J. Phys. Chem. Solids. **26**, 517–522 (1965).

[62] A. L. Giorgi, E. G. Szklarz, E. K. Storms, A. L. Bowman, and B. T. Matthias, Phys. Rev. **125**, 837–838 (1962).

[63] E. V. Clougherty, K. H. Lothrop, and J. A. Kafalas, Nature. **191**, 1194 (1961).

[64] K. Yamaura, Q. Huang, M. Akaishi, and E. Takayama-Muromachi, Phys. Rev. B. **74**, 184510–184515 (2006).

[65] K. Yamaura, Q. Huang, and E. Takayama-Muromachi, Physica C. **468**, 1135–1137 (2008).

[66] E. H. Brandt, Phys. Rev. B. **60**, 11939–11942 (1999).

Chapter 4 Crystal structure and superconducting nature in BiS_2 layered materials

4.1 Superconducting nature of BiS_2 layered based $Bi_4O_4S_3$

In this chapter I would give a detailed discuss about the superconducting nature in BiS_2 layered chalcogenide systems. Very recently, several independent research groups in Japan, China, and India have reported that bismuth oxy-sulfide $Bi_4O_4S_3$ shows exotic bulk superconductivity (SC) in the temperature range 4.4–8.6K [1-3]. The BiS_2 layer (square planar) has been claimed to be the main factor inducing SC in $Bi_4O_4S_3$ [4-5]. Although the observed superconducting transition temperatures (T_c) is lower than that of other high-T_c materials, BiS_2 layered compounds may be a potential prospect for many applications in the field of physics, because high-T_c SC is observed only in a layered structure. In addition, Hall coefficient measurements suggest multiband SC in $Bi_4O_4S_3$, as in the case of Fe-based superconductors [5]. Hence, further investigation of the SC of $Bi_4O_4S_3$ may facilitate greater understanding of the essential physics related to high-T_c SC.

Characterization of a polycrystalline sample of $Bi_4O_4S_3$ indicated that the lower and upper critical fields (H_{c1} and H_{c2}) are approximately 15 Oe and 31 kOe [3], respectively, but a much smaller H_{c1} of ~7.0 Oe has been reported in another study [1]. However, regardless of the small variations in the superconducting properties of $Bi_4O_4S_3$, ongoing studies reveal a large superconducting shielding fraction and zero resistivity. $Bi_4O_4S_3$ crystallizes in a tetragonal structure with the *I*4/*mmm* space group (at room temperature). There is a slight discrepancy in the lattice parameters reported for this compound: a = 3.9592(1) Å and c = 41.241(1) Å [1]; a = 3.978 Å and c = 41.07 Å [2]; and a = 3.9697(2) Å and c = 41.3520(1) Å [3]. Because the abovementioned difference between the values of a and c is less than 0.5% and 0.7%, respectively, it is difficult to establish a reasonable correlation among the lattice parameters and the reported superconducting properties.

In order to reveal the comprehensive SC properties of $Bi_4O_4S_3$, we attempted to grow a high-quality single crystal of $Bi_4O_4S_3$. We adopted a high-pressure (HP) method because the extremely low melting points of Bi (272°C; boiling point: 1564°C) and S (115.2°C; boiling point: 444.7°C) render crystal growth by the conventional methods at ambient pressure (AP) difficult. Although a high-quality single crystal has not yet been grown, I surprisingly found the polycrystalline $Bi_4O_4S_3$ known till date does show most likely

impurity driven SC, in sharp contrast to the observations made in ongoing studies. Although the compound turns to be SC with zero resistivity on cooling to 1.5K, SC has only 0.3 % shielding fraction at most in magnetization (100% is expected for an ideal bulk SC), indicating that the SC unlikely reflects a bulk nature of the BiS_2 layered phase. An electron probe microanalyzer (EPMA) suggested a Bi-rich and S-poor compound, which is possibly amorphous–like, might be responsible for the observed SC.

I found that similar superconducting impurity might complicate the ongoing studies for SC of $Bi_4O_4S_3$ compound prepared by normal process because its full shielding fraction was dramatically decreased to less than 1/14 of that of the pellet even upon gentle grinding. The London penetration depth (λ_L) and the relative sample size unlikely accounted for the remarkable reduction. This was supported by the fact that even a much weaker applied magnetic field of 1 Oe ($<<H_{c1}$) did not improve the shrunk shielding fraction. Instead, mechanical break of a superconducting link thinly spread throughout the grain boundaries and at the surface in a synthesized pellet more reasonably accounted for the dramatic decrease. In the present paper, I report the results of more detailed measurements of $Bi_4O_4S_3$ compounds, which were synthesized using the HP and normal process, under various conditions using both bulk pellet and powder forms.

4.1.1. Experimental

Polycrystalline $Bi_4O_4S_3$ is prepared from fine Bi_2O_3 (99.99%; Soekawa Chemical Co., Tokyo), Bi_2S_3 (99.9%; Kojundo Chemical Lab. Co., Sakado), and S (99.99%; Kojundo Chemical Lab. Co.) powders. The abovementioned powders are mixed in a stoichiometric molecular ratio and placed in a cubic multianvil HP apparatus. Then, they are heated at a specific temperature between 500 and 900°C for 30 min at an elevated pressure of 3 GPa and quenched to room temperature before releasing the pressure. The temperature is monitored by a W:Re5-W:Re26 thermocouple during heating. The mixture is sealed in a Pt capsule and separated from Pt by a hexagonal boron nitride inner cell. The inner cell did not react with the mixture components, as is evident from its unchanged color (white) after heating. For reference, Bi powder (99.9%; Kojundo Chemical Lab. Co.) is heated under the same conditions at 700°C for 30 min. For comparison, polycrystalline $Bi_4O_4S_3$ is prepared by the normal method reported previously [1-3]. The stoichiometric mixture is pressed into a pellet and heated at 450°C for 10 h in an evacuated quartz tube.

The as-prepared compounds all are investigated by X-ray diffraction (XRD) under ambient conditions in an X'Pert Pro system (PANalytical) using monochromatic Cu-Kα radiation. Selected compounds are subjected for XRD Rietveld analysis using RIETAN-FP software [6], and EPMA in JXA-8500F from JEOL. The XRD data for structure refinement are recorded in a RIGAKU X-ray diffractometer at room temperature ranging from 10–120° in 2θ at a step interval of 0.03° using Cu-Ka radiation. The current and voltage to generate the X-ray is 40 mA and 40 kV, respectively. Magnetic susceptibility (χ) measurements are performed using a magnetic property measurement system (MPMS, Quantum Design) in the temperature range 2–300K and at an applied magnetic field of 1 Oe or 10 Oe or 10 kOe, under field-cooling (FC) and zero-field-cooling (ZFC) conditions. The electrical resistivity (ρ) of the polycrystalline pellets is measured by a physical property measurement system (PPMS, Quantum Design) at temperatures between 2 to 300K. The conventional four-terminal method is used for this purpose; the ac-gauge current and frequency are 1 or 2 mA and 110 Hz, respectively. Silver epoxy is used to fix gold wires onto the pellets for the ρ measurements. Additional measurements for χ and ρ are conducted down to 1.6K and 1.4K in a MPMS VSM (Quantum Design) and a ^{3}He probe in PPMS, respectively, for a piece of a selected sample pellet.

4.1.2 Structural properties

All the major XRD peaks for the sample prepared at 700°C are assigned by assuming a tetragonal unit cell with the *I*4/*mmm* space group (Fig.4.1.1), as accomplished in other ongoing studies [1-3]. The lattice parameters a = 3.9592(1) Å and c = 41.241(1) Å are comparable with the previously reported values. When the heating temperature is increased to 900°C, a different XRD profile is observed, indicating the transformation of the tetragonal phase into an unidentified phase. On the other hand, the compounds synthesized at temperatures lower than 700°C contained a small amount of the tetragonal phase and Bi metal and multiple impurities. In the present study, 700°C is identified as the near-optimal temperature for synthesizing polycrystalline $Bi_4O_4S_3$ at 3 GPa, while 500–510°C is the optimal temperature range at AP [1-3]. Interestingly, the same XRD profile is obtained even after a week for the powder synthesized at 3 GPa, suggesting that $Bi_4O_4S_3$ synthesized by the HP method is chemically stable under ambient conditions, as is the powder synthesized by the normal process [1-3]. To refine the structure parameters of the HP compound $Bi_4O_4S_3$, Rietveld analysis is conducted, and the results are summarized in Table 4.1.1 and Fig.4.1.2a.

The *R* factors for the refinements imply that the structure model abovementioned is indeed reasonable for the HP compound $Bi_4O_4S_3$. Meanwhile, the results indicate that small amount of impurities are mixed in the compound.

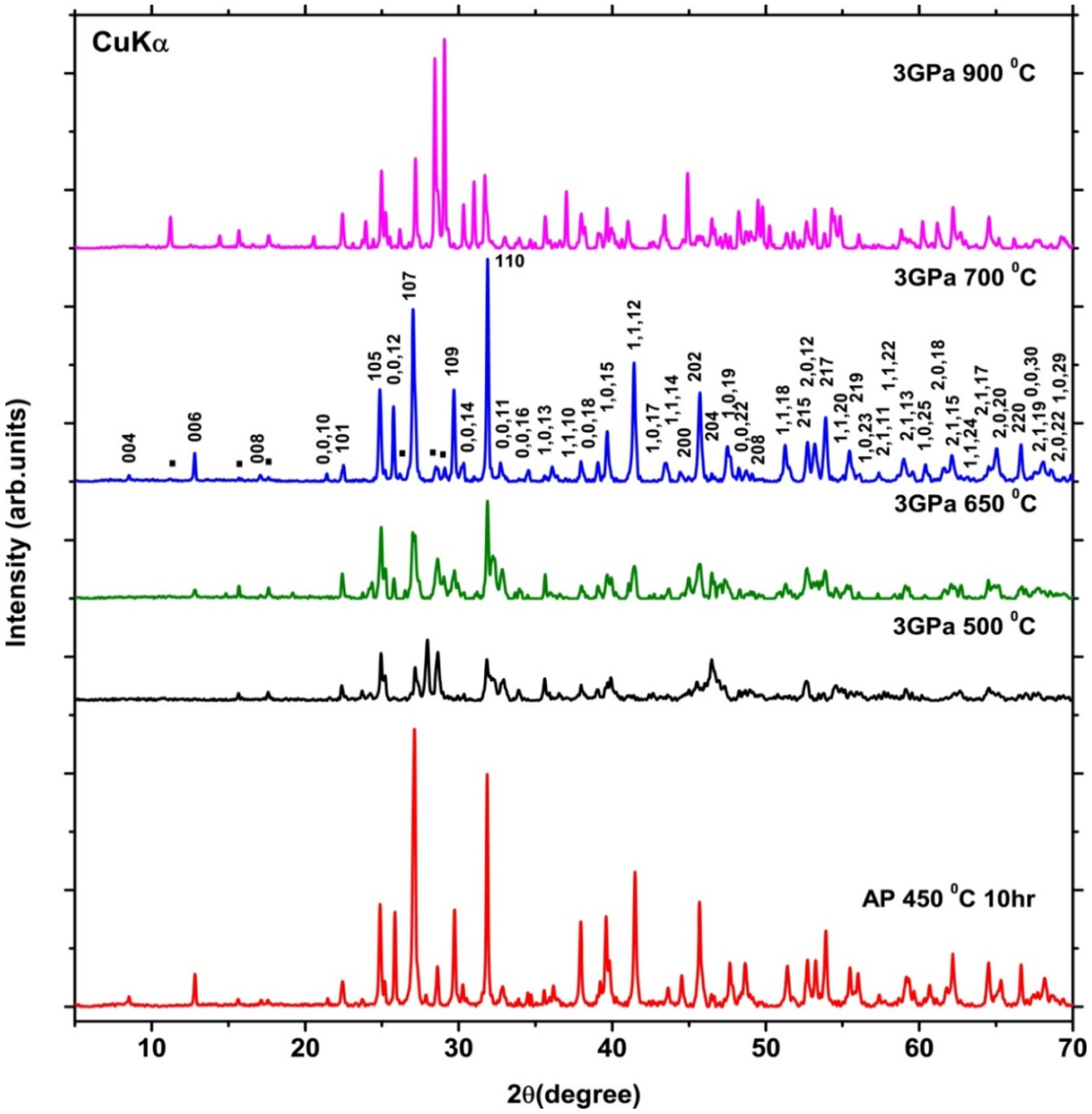

Fig.4.1.1. Powder XRD patterns from a series of $Bi_4O_4S_3$ samples prepared by the HP method. The heating temperatures used for each powder sample are indicated in the figure. The reference pattern for $Bi_4O_4S_3$ sample prepared under AP at 450ºC is shown at the bottom. Characteristic peaks for the tetragonal $Bi_4O_4S_3$ phase are labeled by Miller indices in the pattern for 700ºC as a representative. Solid squares indicate the peaks due to impurities. For clarity, commas are used to separate the numbers in some indices.

Table 4.1.1. Structure and isotropic displacement parameters of $Bi_4O_4S_3$ sample prepared by the HP method.[a]

Atom	site	*g*	*x*	*y*	*z*	B_{iso} (Å^2)
Bi1	4*e*	1	0	0	0.05785(5)	0.5(fixed)
Bi2	4*e*	1	0	0	0.20746(6)	0.5(fixed)
Bi3	4*e*	1	0	0	0.38224(5)	0.5(fixed)
S1	4*e*	1	0	0	0.1444(3)	0.5(fixed)
S2	4*e*	1	0	0	0.2863(3)	0.5(fixed)
S3	2*b*	0.5	0	0	0.5	0.5(fixed)
O1	8*g*	1	0	0.5	0.0912(5)	0.5(fixed)
O2	16*n*	0.25	0	0.27101(fixed)	0.47051(fixed)	0.5(fixed)

[a] Note: Space group *I4/mmm* (No. 139); Chemical formula sum: $Bi_6O_6S_{4.5}$ (Z = 2); a = 3.9252(3) Å, c = 41.088(2) Å, V = 633.05(7) Å^3; d_{cal} = 7.839 g cm^{-3}; R_{wp} = 10.298 %, R_p = 8.002 %. S = 1.967.

Unfortunately, we are unable to identify the impurities in this study. In refinement, the S3 and O2 sites are assumed to be partially occupied and fixed to the $Bi_4O_4S_3$ composition [3]. Note that O2 coordinate parameters *y* and *z* is unable to be refined because only a quarter of the O2 site is occupied; hence the parameters *y* and *z* of O2 are fixed to those obtained in a preliminary refinement with assumption that O2 occupancy factor is 0.5. I also tested a similar structure model proposed in Ref. [1], where the site occupancies of S3 and O2 are fixed to be 1 and 0.5, respectively. The alternative model, however, did not help to improve the refinement quality. Perhaps, neutron diffraction study can refine the structure parameters further. Figs.4.1.2b and 4.1.2c show a comparison of the coordination environment of Bi in the BiS_2 layer between $Bi_4O_4S_3$ phases prepared by the HP method and a normal method. A significant difference is not obvious; however length of the S1–Bi2 bond, which is perpendicular to the BiS_2 layer, is approximately 4% shorter in the HP phase than that in the AP phase (2.66 Å and 2.77 Å). Note that interlayer distance between the BiS_2 layers is

3.19(1) Å for the HP prepared $Bi_4O_4S_3$ and 3.24(1) for the normally prepared $Bi_4O_4S_3$ Ref [1], indicating a trivial change.

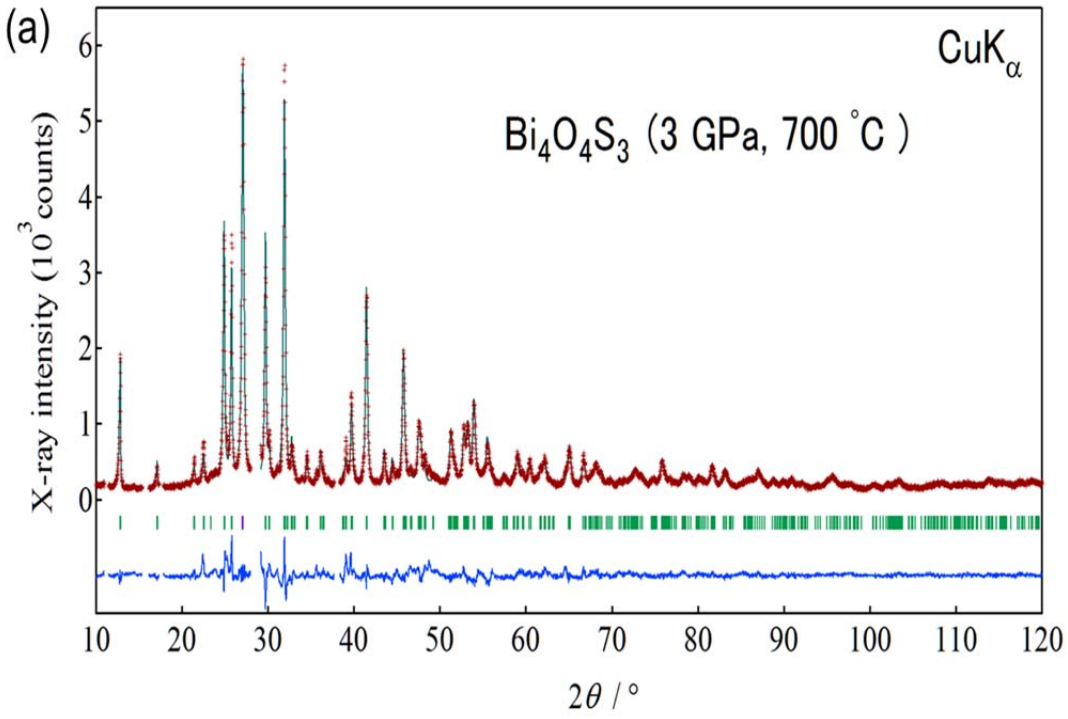

Fig.4.1.2. (a) Rietveld analysis of the XRD pattern of $Bi_4O_4S_3$ sample prepared by the HP method. Markers and solid lines show the observed and calculated profiles, respectively, and the difference is shown at the bottom. The Bragg reflections are denoted by tick marks.

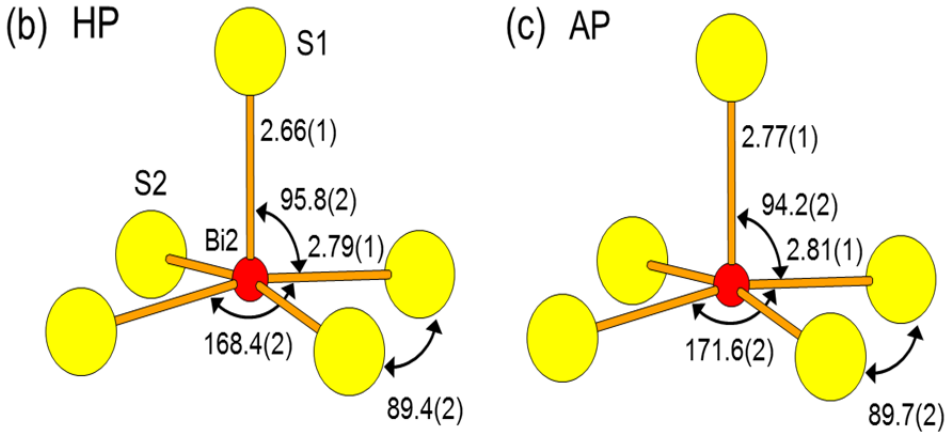

Fig.4.1.2. (b) Local structure coordination of Bi in the BiS_2 layer, drawn based on the present refinement results. The numbers inside are bond distances in Å and angles in degree. (c) Corresponding local structure view for $Bi_4O_4S_3$ synthesized by a normal method for a comparison. The structure data are taken from Ref. [1].

4.1.3 Magnetic properties

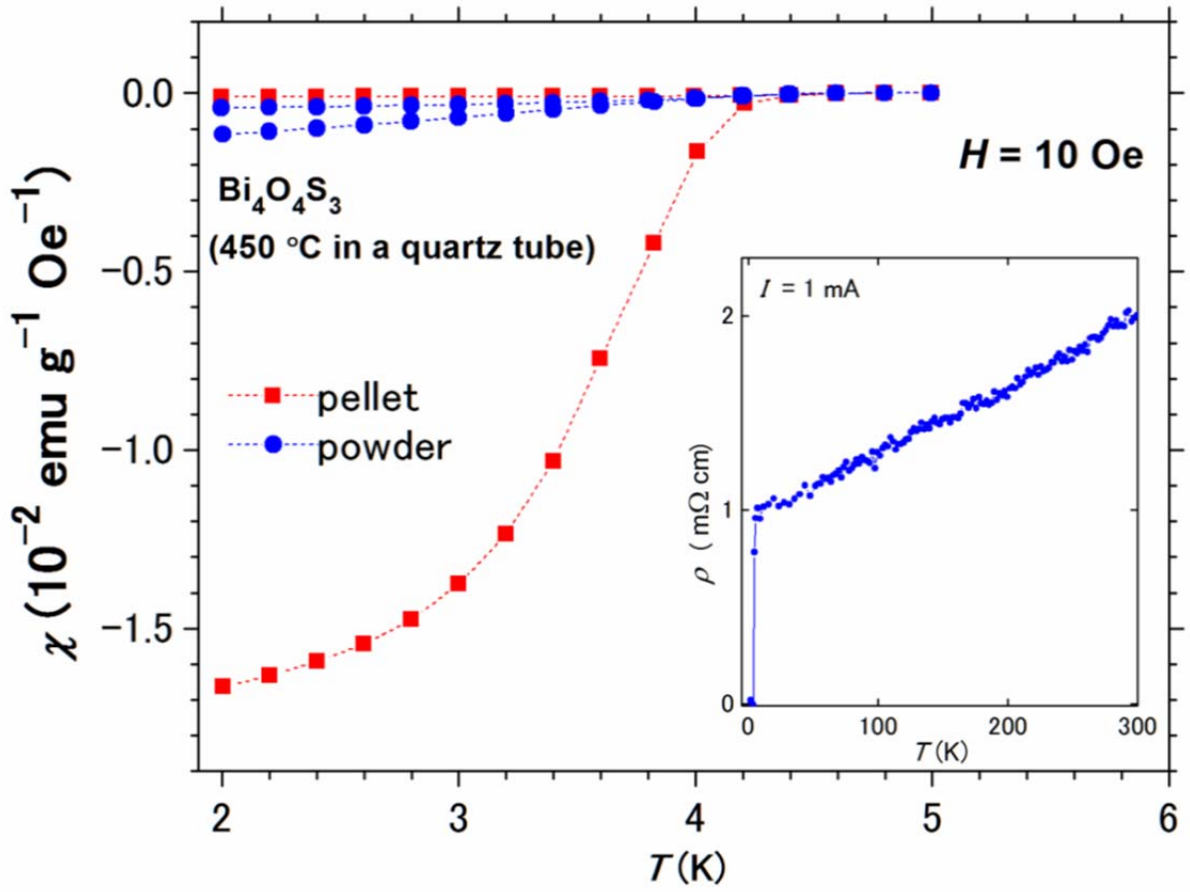

Fig.4.1.3. T dependence of χ for $Bi_4O_4S_3$ prepared under AP. For comparison, measurements were performed on an as-made pellet and gently ground powder. The largest shielding fraction of approximately 126% was observed for the pellet. Insets show the T dependence of ρ for the as-made pellet of $Bi_4O_4S_3$ (AP).

Superconducting properties of $Bi_4O_4S_3$ prepared by the normal method is studied for reference. Magnetic measurements clearly showed a superconducting transition with a notable shielding fraction (~129%, see the ZFC curve in Fig.4.1.3) (the density of the compound is 6.11 g/cm^3, which was measured), as reported in the ongoing studies [1-3]. The slight overestimation of the fraction is probably due to the demagnetizing effect, because the measurement is conducted on a sintered pellet. Meantime, ρ vs. T curve for the polycrystalline $Bi_4O_4S_3$ pellet (inset to Fig.4.1.3) shows a metallic character in the normal state and a sharp drop to zero, as reported previously [1-3]. Thereafter, the pellet is gently ground to an amount of loose powder using an agate mortar and pestle and re-subjected to magnetic measurements.

Noticeably, the shielding fraction decreased to less than 1/14 of that of the pellet. To our best knowledge, the radical decrease in the shielding fraction are not mentioned in so-far literatures [1-3]. Note that chemical and mechanical instabilities of $Bi_4O_4S_3$ are unlikely responsible for the radical decrease because XRD pattern is essentially unchanged over the measurements. The radical decrease seemingly indicated that a superconducting link is physically destroyed by grinding. I would discuss a possible origin of the radical decrease later. Fig.4.1.4 shows the χ–T data measured under a weak magnetic field of 10 Oe for the compounds synthesized under HP conditions in a variety of heating temperatures. The powders used in the XRD measurements are reused in the magnetic susceptibility measurements. The desired amount of each loose powder sample is set in a sample holder and subjected to the χ–T measurements. The sample prepared at 650°C showed a notable diamagnetic transition, presumably a superconducting transition, at 4K. However, the superconducting shielding fraction is less than 2.2% at the low-temperature limit (the density of the compound is assumed to be 7.84 g/cm^3, which corresponded to the calculated density). It is important to note that identical measurements on a pellet (instead of the powder) revealed a comparable shielding fraction, being in stark contrast to the full shielding fraction reported for the compounds prepared by the normal process in other ongoing studies. [1-3].

Because the compound prepared at 650°C contained a small amount of $Bi_4O_4S_3$, I investigated the rest of the compounds in the same manner in order to confirm the reported SC for $Bi_4O_4S_3$. Surprisingly, the near-single-phase $Bi_4O_4S_3$ prepared at 700°C showed negligible anomaly in the χ–T curves, similar to the reference material of Bi and the compound prepared at 900°C. Thus, the magnetic data suggested the absence of the bulk SC in $Bi_4O_4S_3$ synthesized at 3 GPa. Unfortunately, a systematic correlation between the superconducting properties and the synthesis conditions is hardly established and the superconducting volume fraction was just 2.2% at the best in the HP synthesized samples, it is therefore highly challenging to identify the phase responsible for the observed SC in the HP synthesized samples. The inset of Fig.4.1.4 shows the χ–T curves measured under a much stronger magnetic field of 10 kOe for the near-single-phase $Bi_4O_4S_3$ (synthesized at 700°C). The curves are almost temperature-independent, and a small Curie–Weiss-like upturn, which is indicative of an impurity contribution, is found in the low-temperature limit. The upturn part is much smaller than that reported in previous studies on $Bi_4O_4S_3$, [2] indicating the improved quality of the present compound. Further, the temperature-independent χ_0 is comparable to that determined in the ongoing study (0.736×10^{-3} emu mol^{-1} Oe^{-1}). [2].

because $Bi_4O_4S_3$ is metallic in nature, the aforementioned similarity in χ_0 implied that the density of states at the Fermi level is comparable in the two cases.

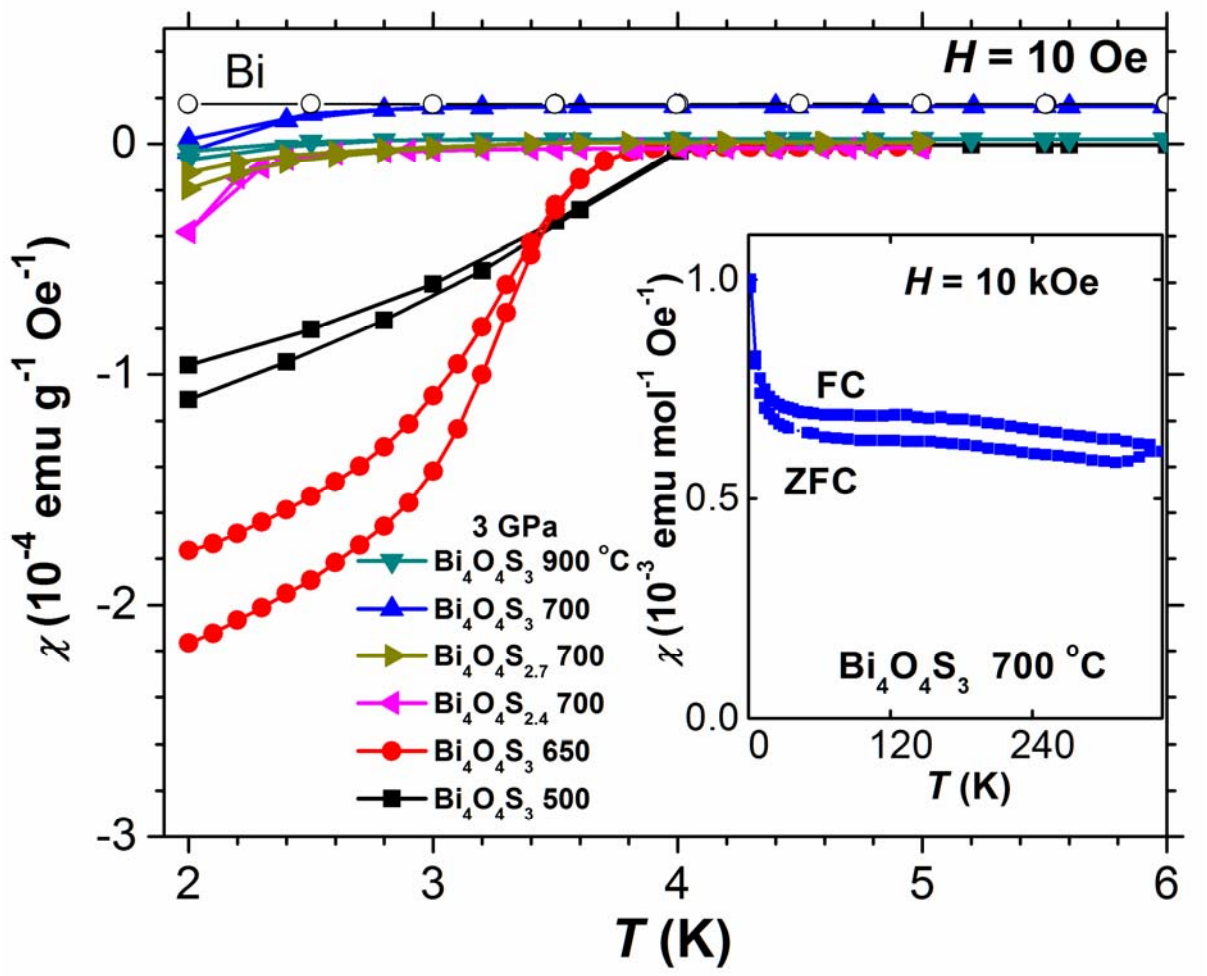

Fig.4.1.4. *T* dependence of χ for the compounds prepared under various heating conditions at 3 GPa. The set of curves for each compound includes the ZFC and FC curves measured under a magnetic field of 10 Oe. The data for the reference materials Bi (annealed at 700°C and 3 GPa) are plotted as well. The largest shielding fraction calculated using a material density of 7.84 g/cm^3 is 2.2% at most. Inset shows the *T* dependence of χ for the single-phase polycrystalline $Bi_4O_4S_3$ under a large magnetic field of 10 kOe.

4.1.4 Transport properties

For further characterization, the ρ–*T* curve of the near-single-phase $Bi_4O_4S_3$ (synthesized at 700°C) is measured (Fig. 4.1.5) down to 1.4K. The data revealed that the compound shows metallic behavior over the measured temperature range; the room-

temperature ρ was approximately 0.8 mΩ-cm. This feature is qualitatively and quantitatively similar to that observed for $Bi_4O_4S_3$ in the ongoing studies.

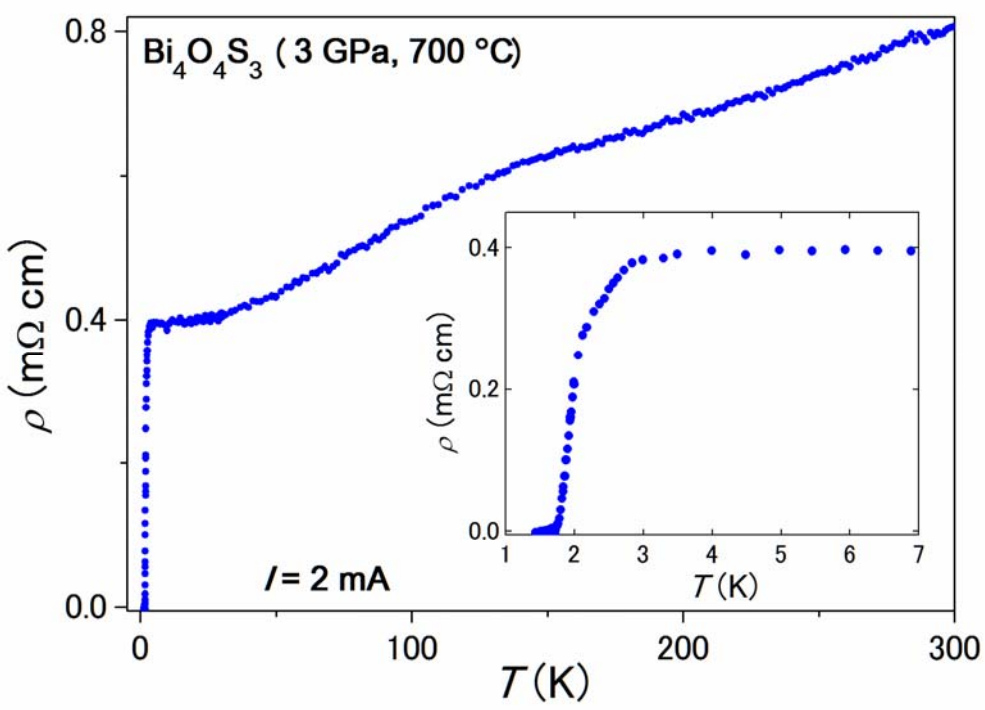

Fig.4.1.5. T dependence of ρ for polycrystalline pellet of $Bi_4O_4S_3$ (HP). Inset shows an enlarged view of the low-temperature part (<7K).

4.1.5 Results and discussion

A broad drop, which was indicative of a superconducting transition, is observed at temperatures below 4K (see inset of Fig.4.1.5); and zero resistivity is confirmed at a temperature of 1.6K. In order to confirm the superconducting shielding fraction at the zero resistivity temperature, the measured pellet is again studied by χ measurements and the superconducting shielding fraction is confirmed smaller than 0.3 % even at 1.6K (Fig.4.1.6). Note that the χ measurements are conducted on the same pellet used for the ρ–T measurements (the pellet was not ground). The remarkably small superconducting shielding fraction is thus in sharp contrast to the bulk SC observed for $Bi_4O_4S_3$ in the ongoing studies [1-3]. The zero resistivity observed and the trivial superconducting volume fraction (<0.3%) in the χ–T curve provide an evidence for impurity driven SC of the $Bi_4O_4S_3$ compound synthesized by the HP method at temperatures exceeding 1.6K. The observed small volume SC (<0.3%) showing zero resistivity is likely caused by a trivial superconducting link, which

is thinly spread out throughout the grain boundaries and at the surface in a synthesized pellet. Unidentified amorphous like thin impurities or altered surface of particles of $Bi_4O_4S_3$ are possible cause of the impurity driven SC observed for the HP prepared pellet. We investigated the possible impurities.

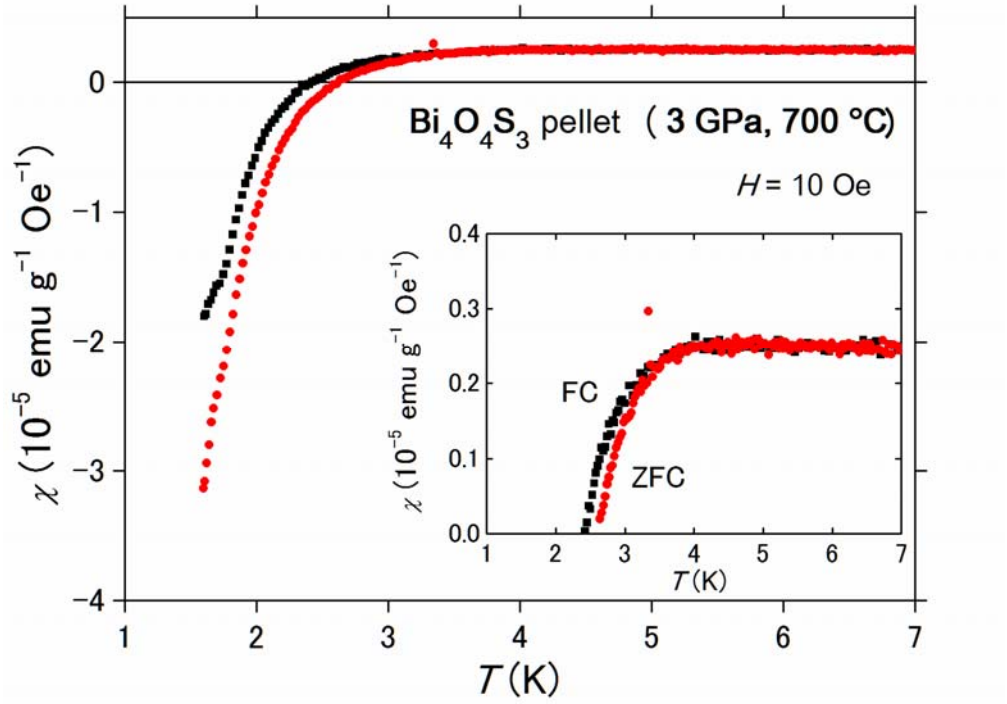

Fig.4.1.6. T dependence of χ for gently ground powder of $Bi_4O_4S_3$ prepared under high-pressure conditions of 3 GPa and 700 °C. The ZFC and FC curves are measured under a magnetic field of 10 Oe. Note that the shielding fraction, calculated using a material density of 7.84 g/cm^3, is 0.3% at most at the lowest temperature, where zero resistivity is confirmed before grinding. Inset shows an enlarged view of the plots.

As the present results appeared to belie the claim for the discovery of bulk SC in $Bi_4O_4S_3$ [1-3], I attempted to identify any possible contribution by the non-stoichiometry of $Bi_4O_4S_3$ to the superconducting properties. Hence, starting mixtures with S-deficient compositions (10 and 20 at%) are tested under the optimized synthesis conditions. However, there are no detectable changes in the lattice parameters and magnetic properties (see Fig.4.1.4), indicating that defect structures are not formed in $Bi_4O_4S_3$. Similar results are obtained for O-deficient starting compositions and S-rich starting compositions. Since the sample is chemically stable, as mentioned earlier in the text, decomposition between the time of synthesis and the time of measurement is unlikely to be cause for the absence of bulk SC. Hence, a possible factor that could account for the impurity driven SC in the present

compound is the undetected difference: for instance, $Bi_4O_4S_3$ prepared at 3 GPa may not be identical to that prepared by the normal process. Local coordination of the structure may be slightly altered in the former case.

To identify the superconducting impurity, polished surfaces of the $Bi_4O_4S_3$ compounds synthesized by the HP method and the normal method are investigated by EPMA. Figs. 4.1.7a and 4.1.7b show composition images (indicated by CP) and elements mapping (S, O, and Bi) at the same magnification. The pellet synthesized by the HP method is much denser than the other, reflecting the measured densities of ~6.94 g/cm^3 (89% of the calculated density for $Bi_4O_4S_3$) and ~6.11 g/cm^3 (78%) for the pellets synthesized by the HP process and the normal process, respectively. Besides, EPMA results indicated that the bright part is relatively more sulfur-deficient and Bi-rich than $Bi_4O_4S_3$. Note that the bright part does not correspond to electric charging in the insulating state because it is a composition image. Since the bright parts are confirmed to exist throughout the grain boundaries and at the surface of $Bi_4O_4S_3$ prepared by the normal method, it is reasonable to attribute the superconducting impurity to the bright parts. I thus attempted to identify the parts by XRD and EPMA; however the studies are unsuccessful probably because the parts are either amorphous-like or thinly spread out. Perhaps, the extremely low melting points of starting materials (Bi melting point: 272°C and S melting point: 115.2°C) may play a key role of forming the bright parts in the heating process; partially melted phases may be somewhat included in the chemical reaction paths to form the bright parts.

The present EPMA and XRD data indicated that the various forms of impurities could play a fundamental role of the zero resistivity observed for the HP and normal process prepared samples. Under the synthesis conditions adopted in the ongoing studies, superconducting impurity might form a link unexpectedly in the $Bi_4O_4S_3$ pellet. This link could be responsible for zero resistivity as well as the full superconducting volume fraction, as is evidenced by the dramatic decrease in the shielding fraction even upon gentle grinding. The impurity driven SC in the HP synthesized $Bi_4O_4S_3$ compound was presumably because the trivial amount of superconducting impurity (as evidenced by the shielding fraction of the pellet smaller than 0.3%) forms a comparable link. Recent specific heat measurements on a full superconducting compound showed only a negligible anomaly at T_c, which seemed to support the idea of the impurity driven SC [7]. Although I was unsuccessful of identifying the superconducting impurity, so I at least could conclude that the impurity drove SC with zero

resistivity above 1.6K for the layered oxysulfide $Bi_4O_4S_3$ compound synthesized by the HP method. It is likely that similar superconducting impurity complicates the ongoing studies for SC of $Bi_4O_4S_3$ prepared by normal process because its shielding fraction is dramatically decreased to less than 1/14 of that of the pellet even upon gentle grinding.

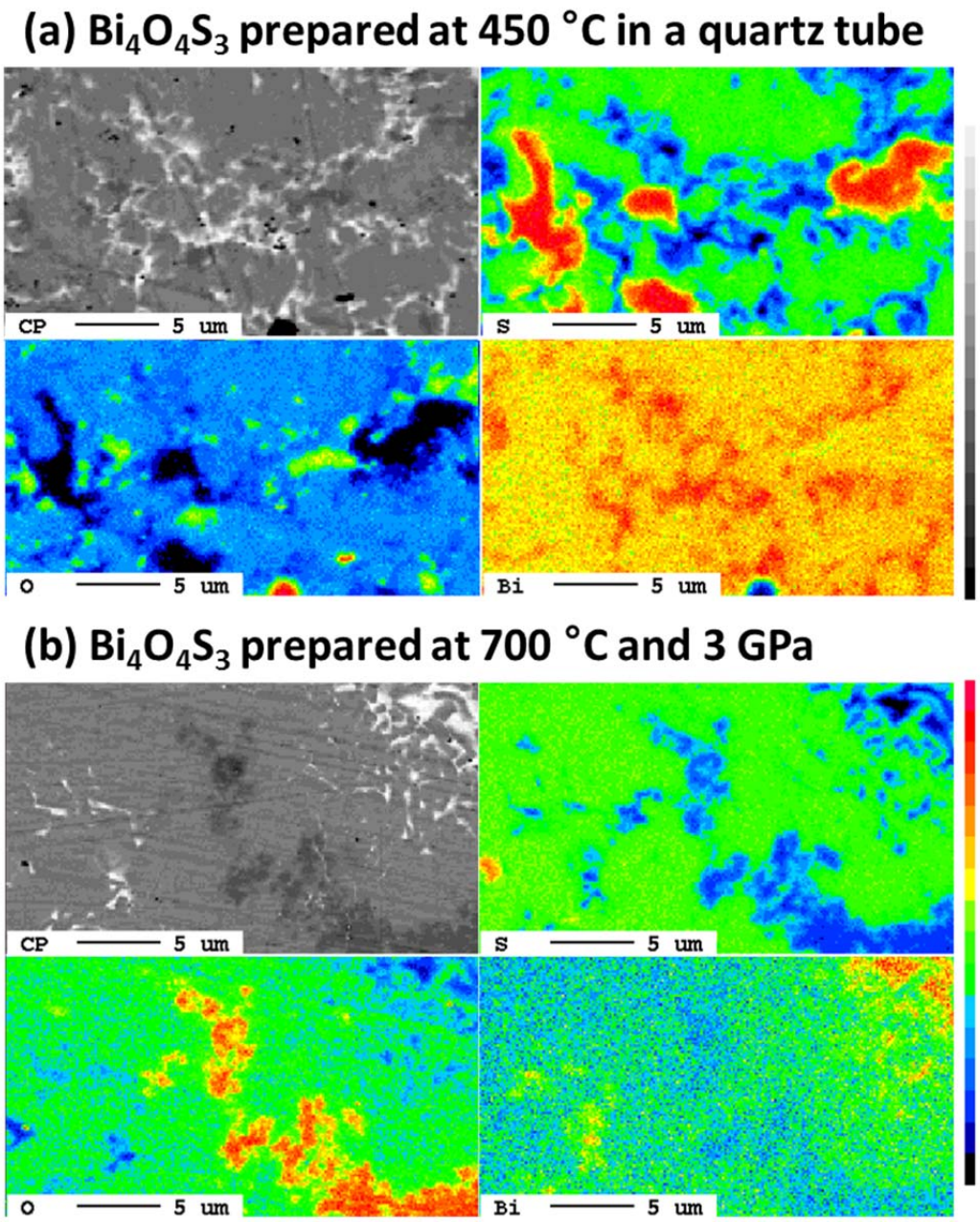

Fig.4.1.7. Comparison of composition image and elemental maps of S, O, and Bi in EMPA for the polished surfaces of $Bi_4O_4S_3$ synthesized under (a) AP and (b) HP conditions.

I investigated the superconducting parameters, which are reported for $Bi_4O_4S_3$ in the ongoing studies. Magnetic measurements in Ref. [3], found that H_{c1} at 2K is ~15 Oe and

the lower critical field (H_{c2}) at 0K is 31 kOe. The coherence length (ξ_{GL}) at T = 0 is then estimated to be ~10 nm, which is nearly comparable with that of MgB_2 and much longer than those of Fe-based and cuprates superconductors (typically few nm) [8].

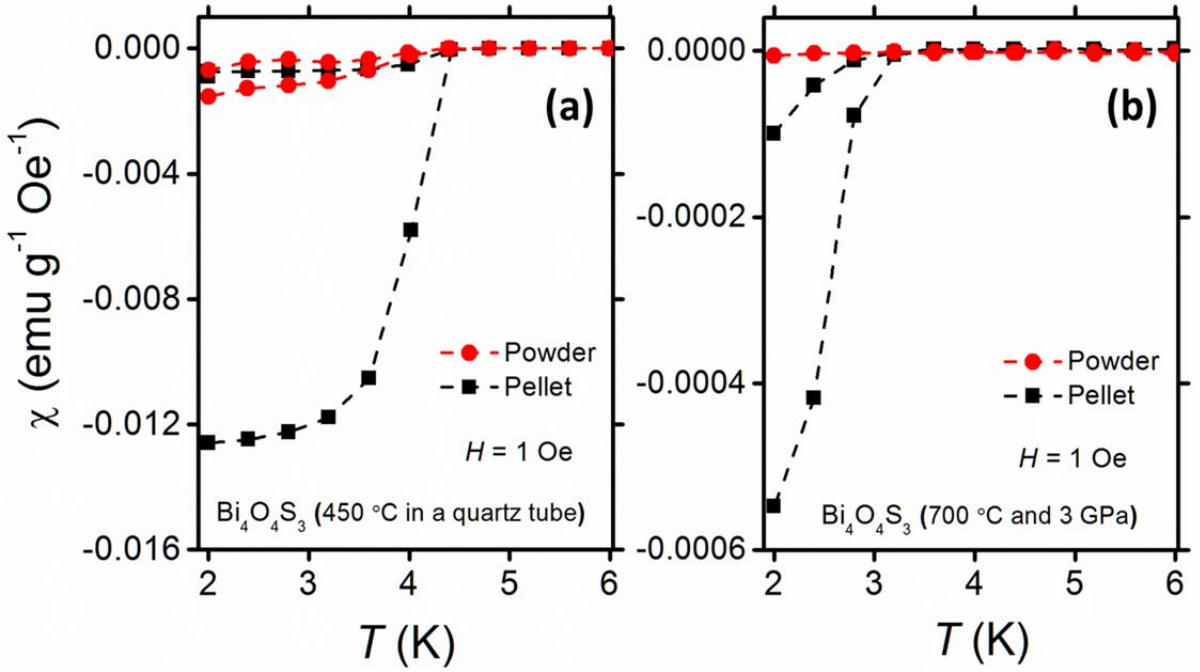

Fig.4.1.8. T dependence of χ for $Bi_4O_4S_3$ prepared under (a) AP and (b) HP conditions measured in an applied magnetic field of 1 Oe. For comparison, measurements are performed on an as-made pellet and gently ground powder.

According to the parameters, I roughly estimated the λ_L to be ~580 nm throughout the Bardeen-Cooper-Schrieffer formula $H_{c1}(T) = (\phi_0 / 4\pi\lambda_L^2)\ln(\lambda_L / \xi_{GL})$, where ϕ_0 is the flux quantum [9]. The λ_L was compared with the size of sample (pellet), which is used to measure the magnetic properties in this study. The HP prepared pellet has the minimum scale dimension of ~1 mm, which is much larger than λ_L; thus the sample scale unlikely impacted on the magnetic measurements. The ground sample for the normally prepared sample has averaged dimensions of powders of few 10 μm (confirmed in optical microscopy). Although it was still much larger than λ_L, I repeated the same magnetic measurements in a magnetic field of 1 Oe (<< H_{c1}) to test a possible impact from the sample scale approaching to the λ_L (Figs.4.1.8a and 4.1.8b). The results, however, showed any notable improvement of the superconducting shielding fraction of the ground sample of the normally prepared sample. Thus, the relative sample scale to the λ_L hardly accounted for the

unusually smaller superconducting shielding fraction of the powder form.

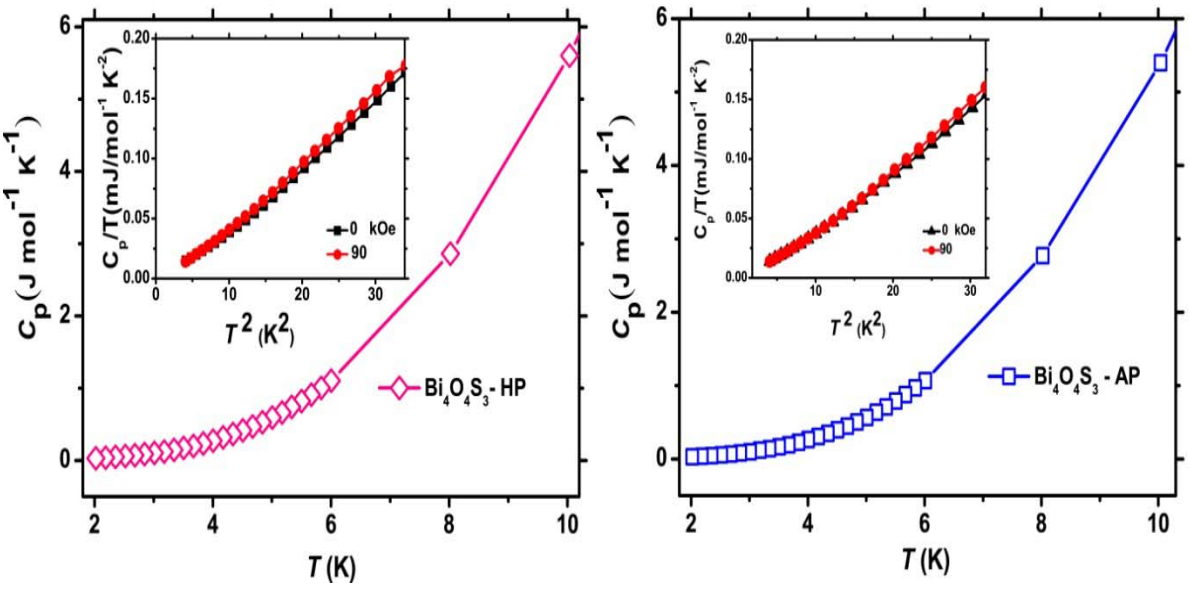

Fig.4.1.9. *T* dependence of specific heat for $Bi_4O_4S_3$ prepared under (a) HP and (b) AP conditions

Temperature dependence of specific heat is measured to know the exact superconducting nature of $Bi_4O_4S_3$ samples prepared under high pressure (HP) and ambient pressure (AP) conditions as show in Fig.4.1.9. From the figure we can clearly note that the specific heat value gradually decreases and goes towards zero in the low temperature part and there was no jump noted at the T_c range of 4.5K. The inset of Fig.4.1.9 shows the extrapolated view of the C_p/T vs. T curve at the T_c range. This result clearly indicates an insulating like behavior from both the HP and AP phases. We hope that the parent tetragonal phase shows insulating like behavior and the small anomaly that is noted from the susceptibility and resistivity measurements may be due to the impurity contribution throughout the grain boundaries. From the above results we clearly state that the materials prepared under high pressure and ambient pressure conditions are not bulk superconductors.

4.2 Superconducting nature of BiS_2 layered based $LaO_{1-x}F_xBiS_2$

Crystals that have layered type structures are widely studied and attracts researchers due to their unique superconducting properties. So far, low-dimensional high T_c superconducting materials with layered structures of cuprates and iron-based materials have been reported [11-15]. Whereas layers of CuO_2 plane and Fe-Z (Z-As, Te, Fe, Se, & P) plane

forms, superconducting layer and some different spacer layers were introduced which leads to the formation of new different layer type materials and its interesting properties are studied extensively. Very recently, new BiS_2 layered structure type superconducting nature was reported in $Bi_4O_4S_3$ material with T_c of 4.5K [1]. Several other groups also reported regarding the superconducting nature in BiS_2 layered $Bi_4O_4S_3$ [2-4]. Out of it, some claimed $Bi_4O_4S_3$ material with BiS_2 layer shows bulk superconducting nature and as I reported previously the impurity throughout grain boundaries formed a superconducting link that contributed the superconducting nature in $Bi_4O_4S_3$ material. The formation of new superconductor with BiS_2 layer has opened new route and gives opportunity to investigate various related materials in the field of unconventional superconductors. Soon after the discovery of $Bi_4O_4S_3$, another BiS_2 layered superconducting material $La(O,F)_{0.5}BiS_2$ is reported with T_c of 10.6K [16], and continuously several other rare earth $Ln(O,F)_{0.5}BiS_2$ (Where Ln = Pr, Nd & Ce) with superconducting transition ranging between 2.7 - 5.6K respectively are also reported [17-19]. Apart from the superconducting BiS_2 layered materials, layered oxysulfide $Yb(O,F)_{0.5}BiS_2$ and $SrFBiS_2$ compounds showing antiferromagnetic and semiconducting like behavior are also reported [20-21], where $SrFBiS_2$ shows a close resemblance with the parent material $LaOBiS_2$ which also shows semiconducting property [21]. So far, a clear detailed study about $LaOBiS_2$ and its properties are lacking experimentally. In $Bi_4O_4S_3$ and $Ln(O,F)_{0.5}BiS_2$ materials, BiS_2 superconducting layer and a spacer layer (Bi_2O_2 & LaO) stacking resembles like the layered high T_c cuprates and iron-based superconducting materials. However, so far a clear picture of superconducting nature in BiS_2 layered materials are lacking and further studies are needed to know the exact nature of these materials.

In this work, I report the successive synthesis of nearly pure phase $LaOBiS_2$ and substitution of fluorine for oxygen using the high pressure and high temperature technique and detailed systematic investigations on the structure and bulk properties such as electrical transport and magnetic properties were studied in detail.

4.2.1 Experimental

Polycrystalline samples of $LaO_{1-x}F_xBiS_2$ with x = 0, 0.1, 0.2, 0.3, 0.4, 0.5, 0.6, 0.7, 0.8, 0.9, 1.0) is prepared using fine powders of La (99.99%; rare metallic.co Ltd), La_2O_3 (99.99%; rare metallic.co Ltd), LaF_3 (99.99%; rare metallic.co Ltd), Bi_2S_3 (99.9%; Kojundo Chemical Lab. Co., Sakado), and S (99.99%; Kojundo Chemical Lab. Co.) powders. The above-mentioned powders are mixed in a stoichiometric molecular ratio and placed in a cubic

multi-anvil HP apparatus. Then, they are heated at a specific temperature between 850 and 890°C for 30 min at an elevated pressure of 2 GPa and quenched to room temperature before releasing the pressure. The temperature is monitored by a W:Re5-W:Re26 thermocouple during heating. The as-prepared compounds are investigated by X-ray diffraction (XRD) under ambient conditions in an X'Pert Pro system (PANalytical) using monochromatic Cu-Kα radiation. Selected compounds are subjected for XRD Rietveld analysis using RIETAN-FP software [6]. The XRD data for structure refinement were recorded in a RIGAKU X-ray diffractometer at room temperature ranging from 10–120° in 2θ at a step interval of 0.03° using Cu-Kα radiation. The current and voltage to generate the X-ray was 40 mA and 40 kV, respectively. Magnetic susceptibility (χ) measurements are performed using a magnetic property measurement system (MPMS, Quantum Design) in the temperature range 2–10K and at an applied magnetic field of 10 Oe, under field-cooling (FC) and zero-field-cooling (ZFC) conditions. The electrical resistivity (ρ) of the polycrystalline pellets is measured by a physical property measurement system (PPMS, Quantum Design) at temperatures between 2 to 300K. The conventional four-terminal method is used for this purpose; the ac-gauge current and frequency are 5 mA and 110 Hz, respectively. Silver epoxy is used to fix gold wires onto the pellets for the ρ measurements.

4.2.2 Structural properties

X-ray diffraction pattern of a series of $LaO_{1-x}F_xBiS_2$ samples by substituting different ratios of fluorine for oxygen is measured under the ambient conditions are shown in Fig.4.2.1. For $LaOBiS_2$ the Bragg reflections are indexed very well clearly indicating that the compound crystallizes in ZrCuSiAs type tetragonal unit cell with *P4/nmm* space group. Lattice parameters *a, c* & *V* are calculated from the 2θ values of selected Bragg reflections and Miller indices for a series of $LaO_{1-x}F_xBiS_2$ samples and plotted against the concentration of *x* as shown in Fig.4.2.2 (a) and 4.2.2 (b). From the comparison of lattice parameters against concentration of *x*, lattice constant *a* increases gradually and lattice constant *c* decreases by increasing the substitution of F, also the volume gradually decreases likewise. While extrapolating the 2θ values from 25 to 27 as shown in Fig.4.2.2 (c), peak positions (102) and (004) starts shifting slightly by substituting and increasing the concentration of F. This clear shift in peaks corresponds to the shrinkage in lattice by increasing F, and this result clearly indicates that substituting F for O is successful, because the ionic radius of F is smaller than O, and this result shows a strong comparison with the previous reports. In addition,

substitution of $F_{0.9}$ for O structure showed distortion of the phase and fully substitution of F changed to some unidentified structure.

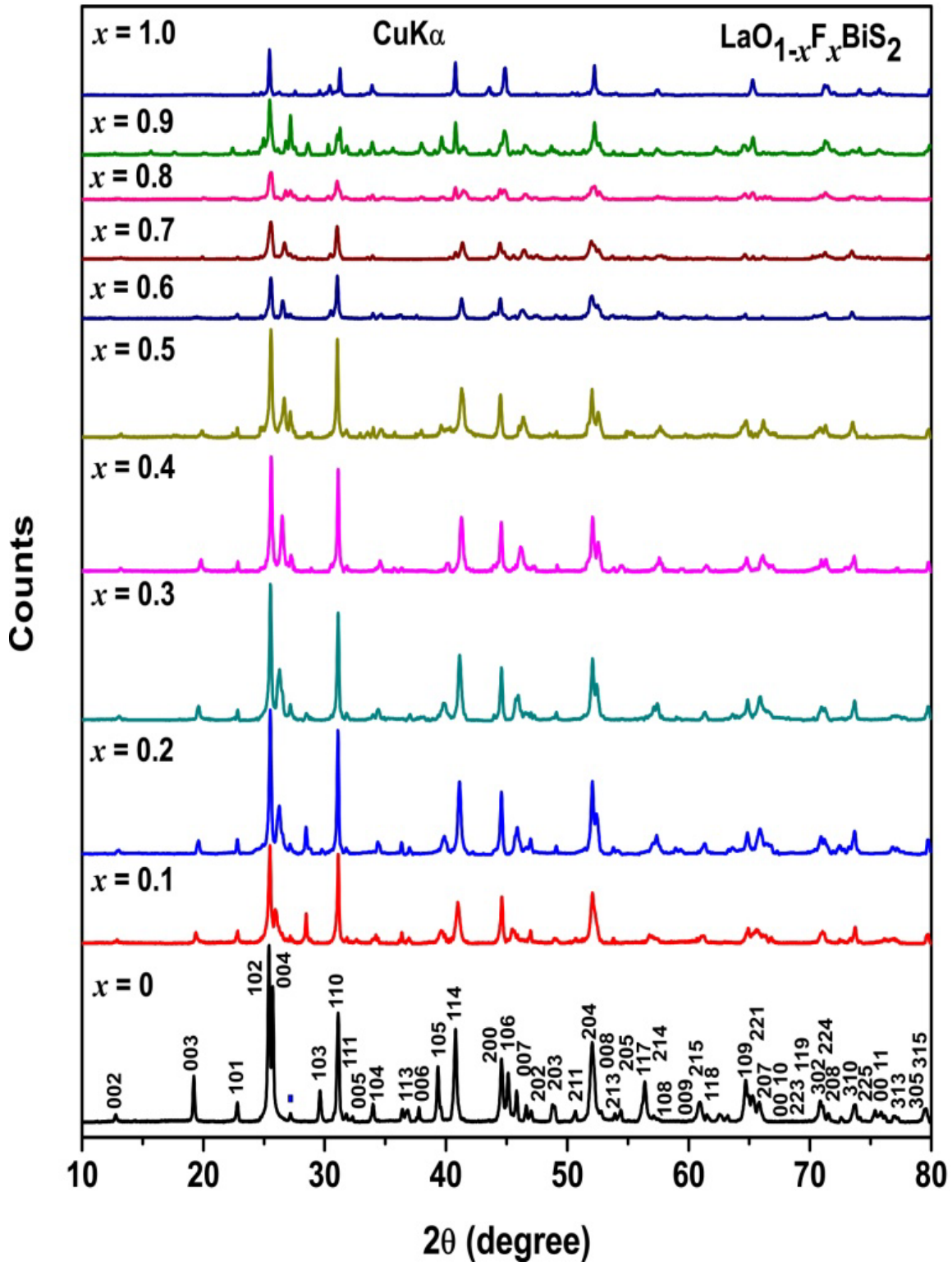

Fig.4.2.1. Powder XRD patterns for a series of $LaO_{1-x}F_xBiS_2$ samples prepared by the HP method. Solid squares indicate the peaks due to impurities.

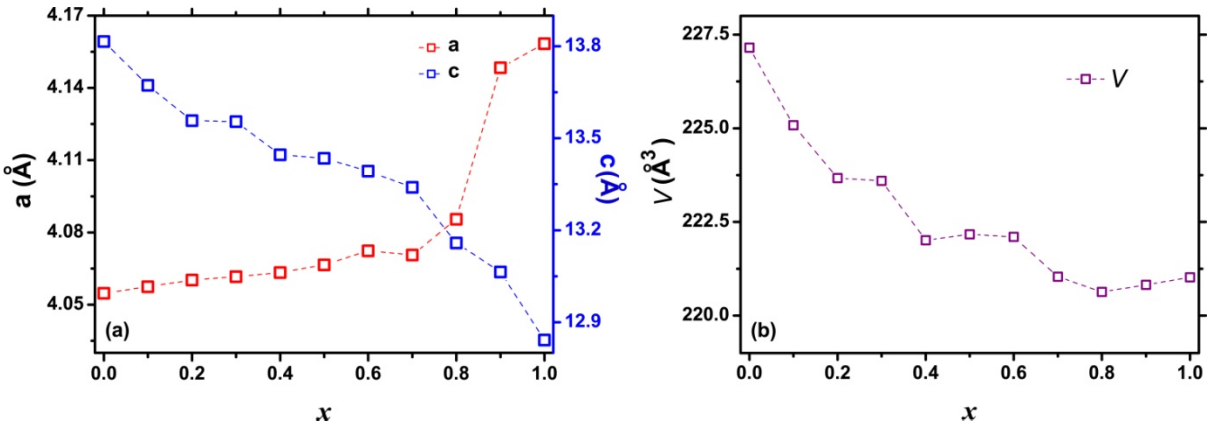

Fig.4.2.2. (a) & (b) comparison of Lattice parameters *a*, *c* and *V* for $LaO_{1-x}F_xBiS_2$

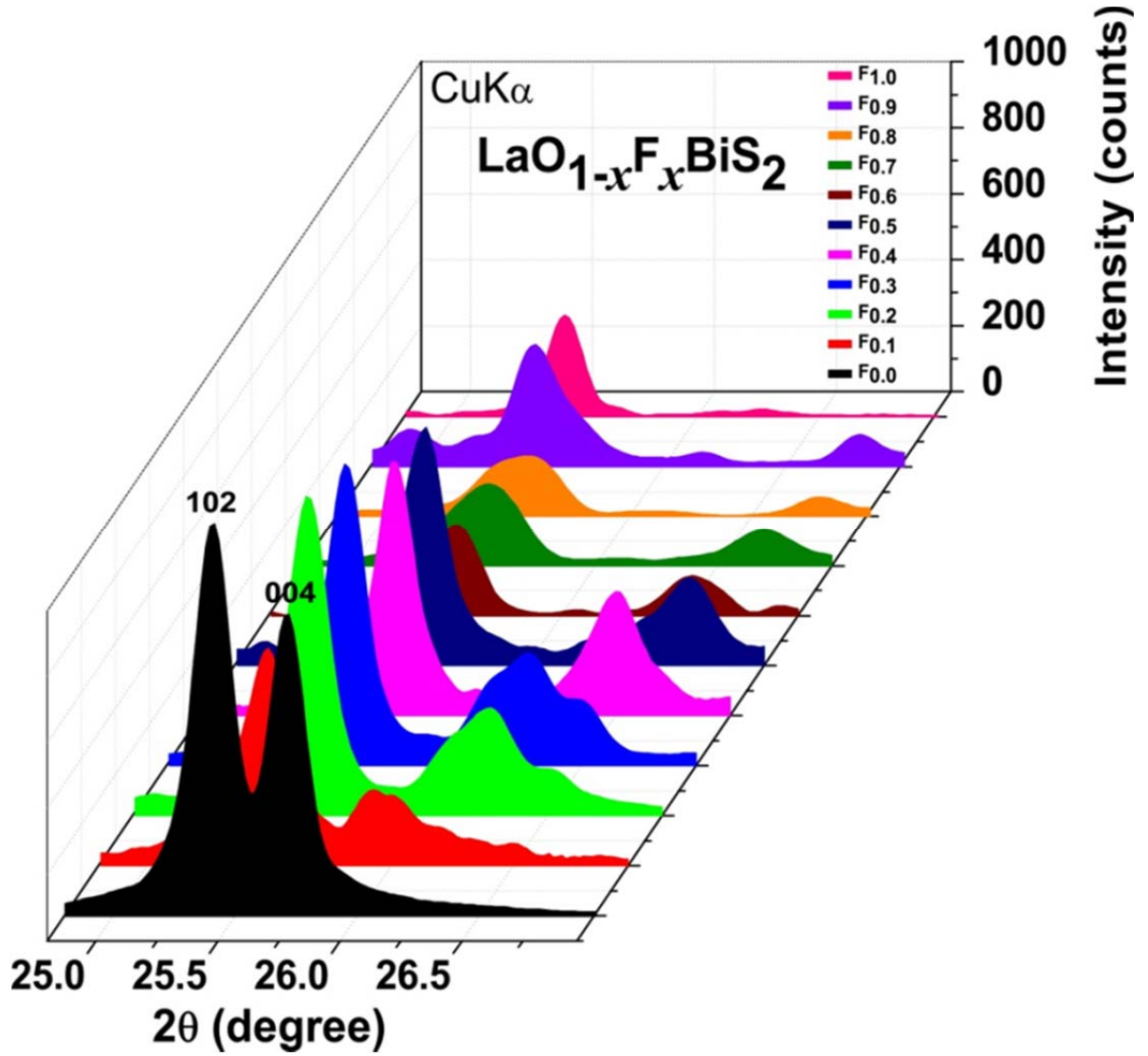

Fig.4.2.2. (c) extrapolation of 102 and 004 peak showing shifting of peaks by substitution of Fluorine.

In order to know the structure parameters in detail Rietveld analysis is carried out for $LaOBiS_2$ sample measured by conventional X-ray powder diffraction method, and the results are summarized in Table 4.2.1 and Fig.4.2.3 (a). The observed and calculated profiles are averagely very smooth as shown in the bottom of Fig.4.2.3 (a) and this shows a good fitting. The reliable factors for the refinements imply that the structure model above mentioned is indeed reasonable for the HP synthesized compound $LaOBiS_2$ and the atomic coordinates are shown in Table.4.2.2. The Bragg reflections are denoted by tick marks. Schematic view of the crystal structure predicted from the refinement data is shown in the inset of Fig.4.2.3 (a). It shows a layered structure with BiS_2 sequence and LaO spacer layers. From the refinement, I also found that there is a negligible amount of impurity contribution and is suspected as La_3S_4, and there is no evidence for separate layer of this phase in the system.

To know more about $LaOBiS_2$ phase I measured the bond distance and bond angles and shown in Table.4.2.3. Local structure coordination drawn based on the present refinement results are shown in Fig.4.2.3 (b) the numbers inside are bond distances in Å and angles in degree. Fig.4.2.3 (c) corresponds to the local structure coordination for $LaOBiS_2$ synthesized by a normal method taken for a comparison for reference [16]. A decrease in the bond angle and bond distances for the sample prepared under high-pressure are noticed when compared with reference sample [16]. This shows that sample prepared under high-pressure conditions showed a compression in the crystal structure. The distance between two BiS_2 layers drastically decreased more than 7- 8% when compared with the normal method synthesized sample [16]. For example, the distance between two BiS_2 layers was 3.5280 Å for the high-pressure prepared sample and 3.6180 Å in the case of reference sample [16]. From this change in the bond angle and bond distances there might be some interesting properties in this crystal system. As the samples prepared under high pressure is denser than samples prepared under normal conditions exact intrinsic properties can be explored. The physical property measurements are carried out for the $LaO_{1-x}F_xBiS_2$ samples to know whether the high-pressure has some effect on the properties.

Table 4.2.1. Crystallographic Data obtained from Conventional X-ray powder diffraction for $LaOBiS_2$

Empirical formula	$LaOBiS_2$
Formula Weight (g/mol)	428.015
Crystal system	Tetragonal
Space group	P 4/nmm (No.129)
Unit-cell dimensions	
$\boldsymbol{a}$ (Å)	4.0623(2)
$\boldsymbol{c}$ (Å)	13.8515(8)
$\boldsymbol{V}$ ($Å^3$)	228.58(3)
Z	2
Density (g/cm^3)	6.2183

Table 4.2.2. Atomic coordinates of $LaOBiS_2$

Atom	Site	*x*	*y*	*z*	*B* ($Å^2$)
La	2c	0.5	0.0	0.08980(4)	0.530(2)
Bi	2c	0.5	0.0	0.63142(4)	1.087(2)
S1	2c	0.5	0.0	0.37662(4)	1.0
S2	2c	0.5	0.0	0.80633(4)	1.0
O	2a	0.0	0.0	0.0	1.0

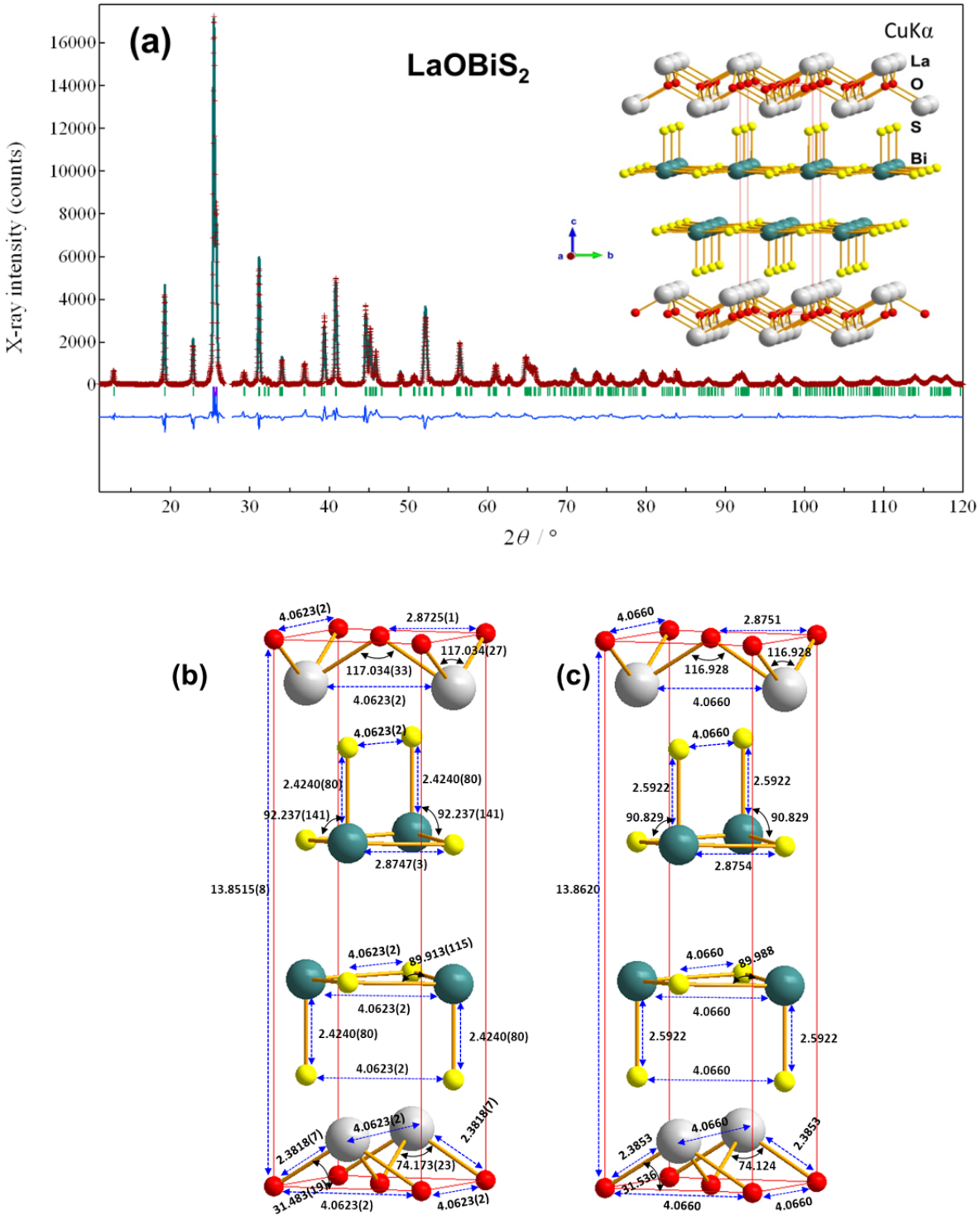

Fig.4.2.3. (a) Rietveld analysis of the XRD pattern of $LaOBiS_2$ sample prepared by the HP method. Markers and solid lines show observed and calculated profiles, respectively, and the bond distances in Å and angles in degree.(b) Local structure coordination drawn based on the present refinement results (c) Corresponding local structure coordination for $LaOBiS_2$ synthesized by a normal method for a comparison. The structure data are taken from Ref. 16.

Table 4.2.3. Selected Bond Distances and Bond Angles of $LaOBiS_2$

Bonds	Bond distance(Å)	Bonds	Bond angle($Å^3$)
La La	4.0623(2) x 2	O La O	117.034(27)
La O	2.3818(7) x 12	La O La	117.034(23)
Bi Bi	4.0623(2) x 2	O La O	74.173(23)
Bi S1	2.8747(3) x 8	O O La	31.483(19)
Bi S2	2.424(80) x 4	La O O	58.517(19)
S1 S1	4.0623(2) x 2	S2 Bi S1	92.237(14)
S2 S2	4.0623(2) x 2	S2 Bi S2	89.913(11)
O O	2.8725(1) x 8		
O O	4.0623(2) x 8		
O O	13.851(8) x 4		

4.2.3 Magnetic properties

Temperature dependent magnetic susceptibility of the sample is measured under an applied magnetic field of 10 Oe for all the $LaO_{1-x}F_xBiS_2$ samples as shown in Fig.4.2.4 (a). The samples showed a superconducting transition (T_c) at 8.2K and it gradually decreases and showed a sharp drop for all the samples (ZFC curve). The notable character here is, even after increasing the substitution of F for O there is no change in the transition temperature. This clearly states that the substitution of fluorine for oxygen in $LaOBiS_2$ sample has no influence on the transition of the sample. While previous reports states that by substituting fluorine for oxygen property changed from semiconducting to superconducting transition in the $LaO_{1-x}F_xBiS_2$ sample. The extrapolated view of the dropping around T_c at 8.2K is shown in Fig.4.2.4 (b) for selected samples. In addition, the shielding fraction is calculated for all the samples from the calculated density of 6.2183 g/cm^3 and plotted with the volume percentage versus concentration of x in $LaO_{1-x}F_xBiS_2$ as shown in the inset of Fig.4.2.4 (a). The highest shielding fraction is noticed in the sample of x = 0.2. The results clearly stated that samples prepared under high-pressure conditions have no intrinsic superconducting properties, while the previous report states superconducting nature. I hope that the superconducting nature in these samples may be due to some impurities that formed along the grain boundaries of the

crystal system. To get rid of the confusion why these samples show superconducting nature temperature dependent resistivity measurements should be carried out.

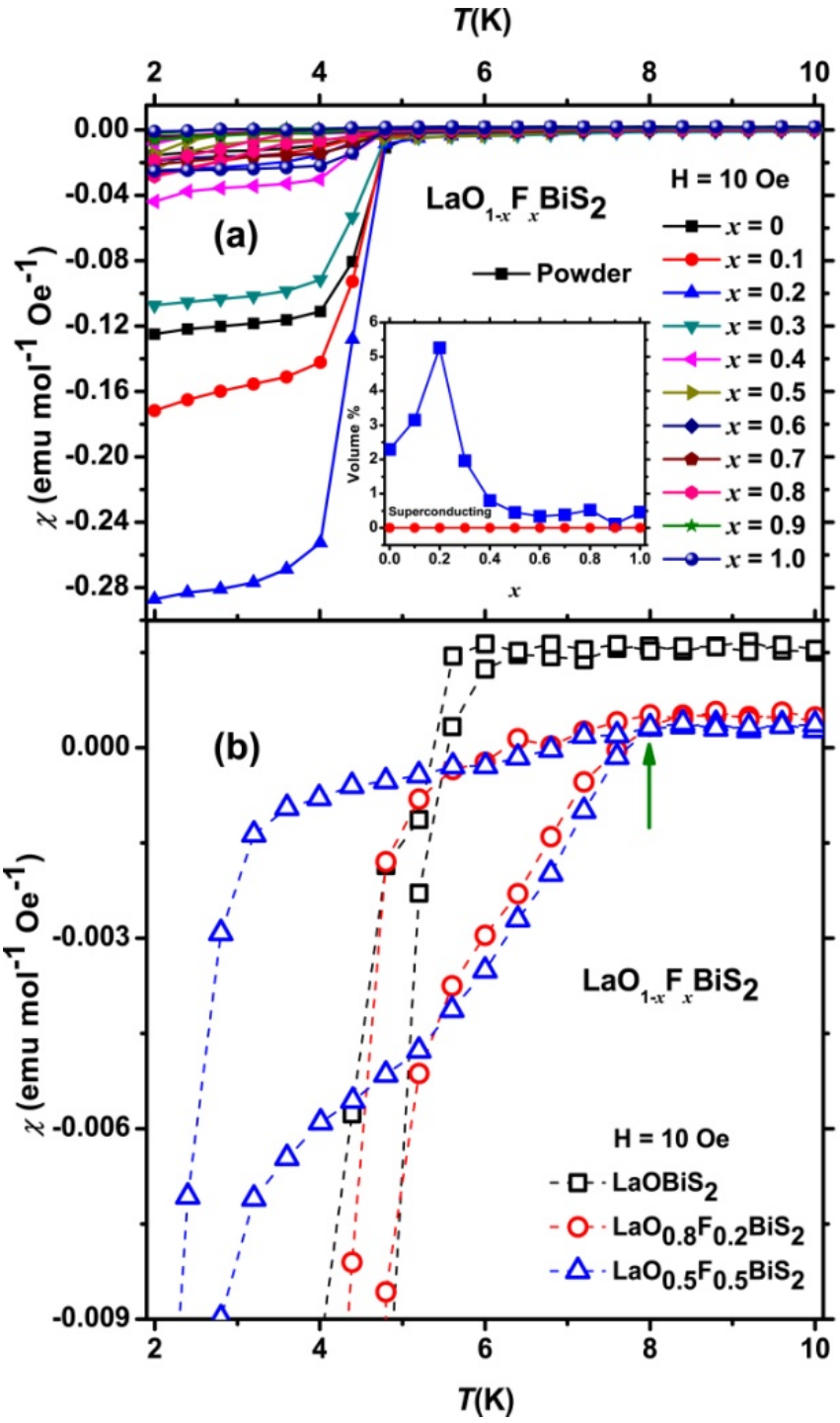

Fig.4.2.4 (a) T dependence of χ for $LaO_{1-x}F_xBiS_2$ samples. The set of curves for each compound includes the ZFC and FC curves measured under a magnetic field of 10 Oe. Inset of (a) shows the superconducting shielding fraction calculated for $LaO_{1-x}F_xBiS_2$ samples. (b) shows the enlarged view for the selected samples of $LaO_{1-x}F_xBiS_2$ and arrow indicates the temperature at which it starts to drop.

4.2.4 Transport properties

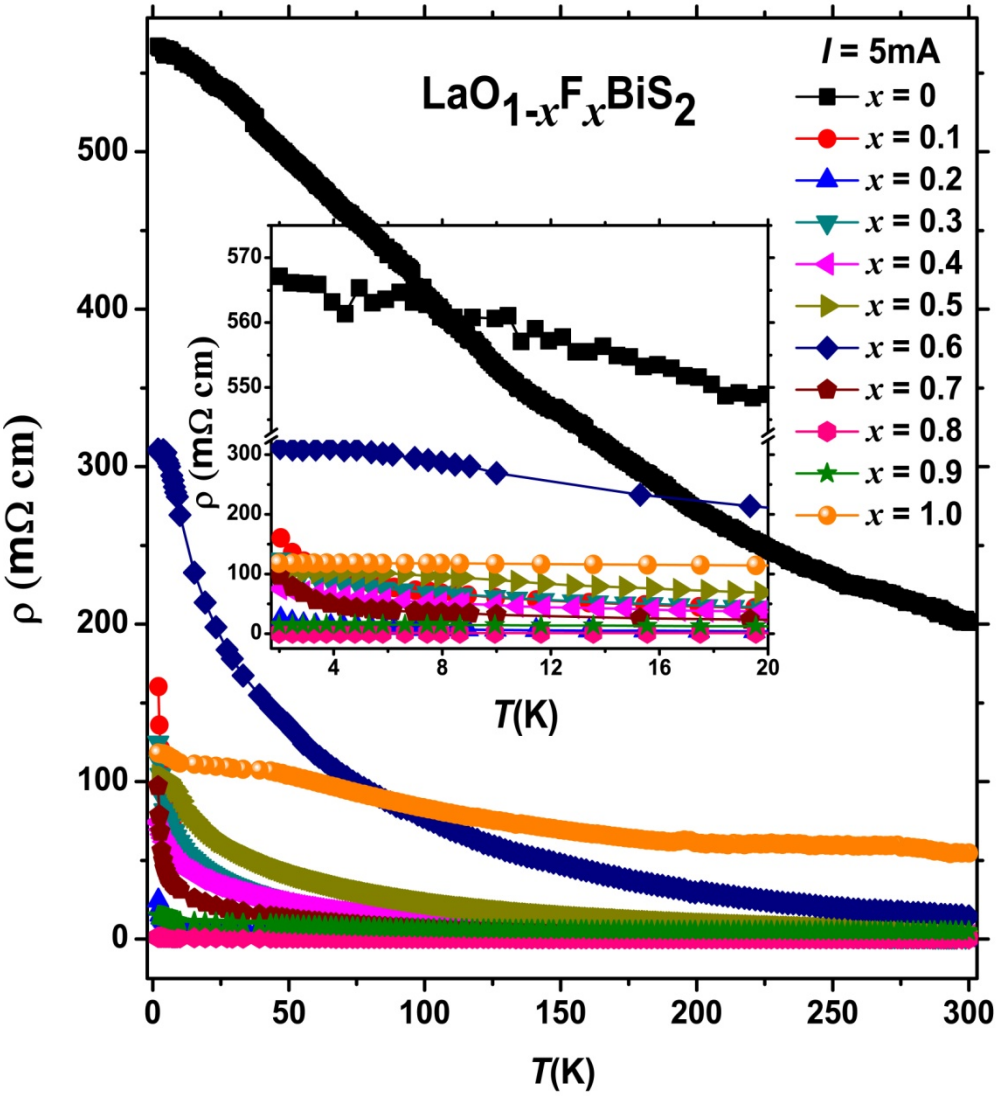

Fig.4.2.5. *T* dependence of ρ for polycrystalline pellet of $LaO_{1-x}F_xBiS_2$. Inset shows an enlarged view of the low-temperature part (<20 K).

Superconducting nature in $LaO_{1-x}F_xBiS_2$ phase is further confirmed by characterized the samples using temperature dependence resistivity (ρ) ranging from 2 to 300K as shown in Fig.4.2.5. While decreasing the temperature down from room temperature it shows the small resistivity value and going to lower temperatures it starts gradually increasing. The data revealed that the compound showed a semiconducting like behavior and the resistivity (ρ) at room temperature for the parent material $LaOBiS_2$ is around 221 mΩ-cm and at 2K, the resistivity is very high showing a value of 568 mΩ-cm. This clearly states that the parent material is a semiconductor and the results are very comparable with the previous

reports. The substitution of fluorine for oxygen made a decrease in the resistivity value and is decreased while substituting further, but no superconductive drop is noticed until the temperature of 2K. For a comparison the extrapolated view of resistivity for all $LaO_{1-x}F_xBiS_2$ samples below 20K is shown in the inset of Fig.4.2.5. The resistivity data for $LaO_{1-x}F_xBiS_2$ phases clearly prove that there is no superconducting nature in the sample and the small superconducting like anomaly that we can see from the susceptibility measurements might be due to some impurities that has been formed along the grain boundaries while crystal formation.

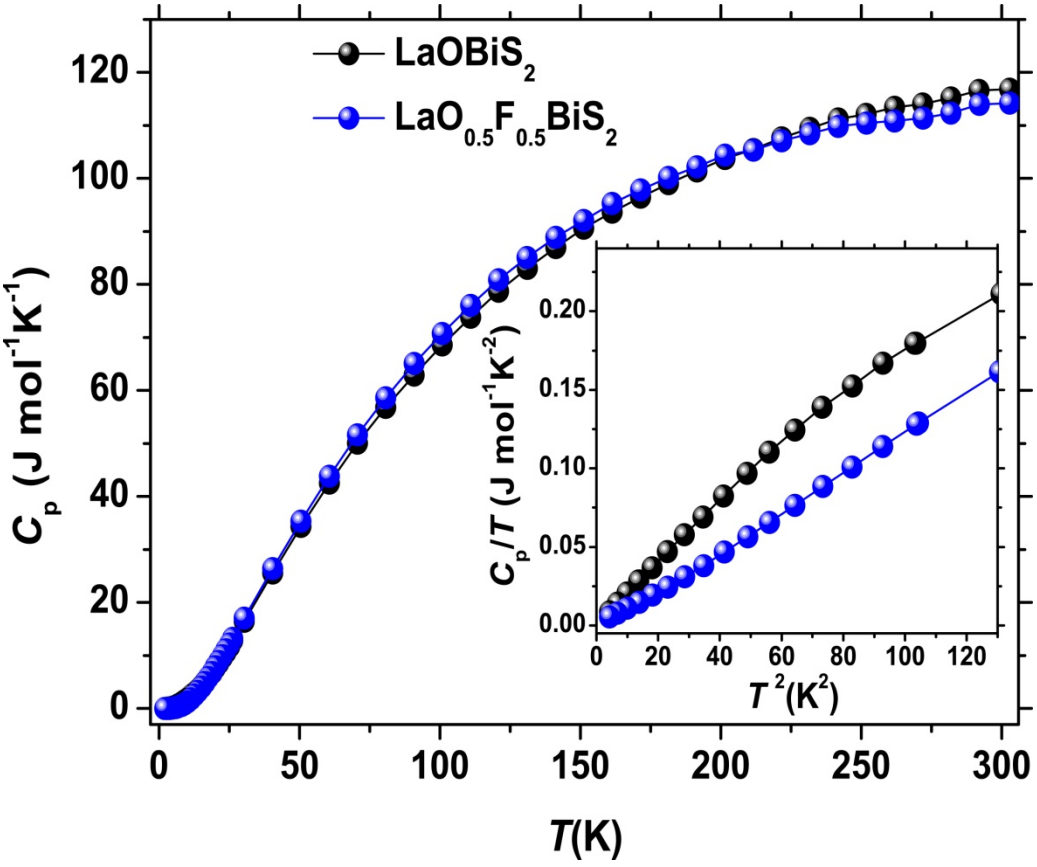

Fig.4.2.6. *T* dependence of specific heat (C_p) for $LaO_{1-x}F_xBiS_2$. Inset shows C_p/T vs. T^2 at the lower temperature limit.

To know further about the electronic properties we measured the specific heat (C_p) for the parent material $LaOBiS_2$ and F substituted $LaO_{0.5}F_{0.5}BiS_2$ samples to temperatures ranging between 2 to 300K as shown in the Fig.4.2.6 From the results we can clearly note that both compounds show a continuous and monotonic temperature dependence of specific heat and no anomalous behavior was noted. Inset of Fig.4.2.6 shows the low temperature part of C_p/T vs. T^2 and no C_p jump is noted and the γ value is estimated to be

very low which are near to zero at 0K. This behavior clearly shows semiconductor like property for both the compounds. $LaO_{1-x}F_xBiS_2$ samples analyzed using the temperature dependence of magnetic susceptibility, resistivity and specific heat measurements clearly states that it is not a bulk superconductor and the superconductive nature might be due to some unknown impurities.

4.2.5 Results and discussion

$LaO_{1-x}F_xBiS_2$ samples analyzed using the temperature dependence of magnetic susceptibility and resistivity clearly states that it is not a bulk superconductor and the superconductive nature might be due to some unknown impurities. In a low melting point element-system there is a possibility for the formation of eutectic alloys, i.e., one or more compositions of crystal forms (new phases) along the grain boundaries during the cooling process after heating the samples to target temperatures while synthesizing and this might be the reason for the formation of superconducting nature in $LaO_{0.5}F_{0.5}BiS_2$ as reported earlier. However, this kind of behavior is not possible to occur in the samples prepared under high-pressure conditions due to quenching process. Well, there are several reports on the superconducting nature of La_3S_4 phase prepared under ambient pressure synthesis conditions with a superconducting transition around 8.25K [22-23], while extrapolating the ZFC and FC curves at temperatures above the transition temperature range, it shows a T_c of around 10.3K is reported by G.L.Guthrie *et al* in 1966 [22]. This might be the core reason for impurity driven superconductive nature in $LaO_{1-x}F_xBiS_2$ phase.

4.3 Conclusion

In summary, I carried out magnetic susceptibility and electrical resistivity measurements as well as electron microprobe analysis on $Bi_4O_4S_3$, which is recently claimed to be a bulk superconductor (T_c = 4.5K). Quality improved polycrystalline $Bi_4O_4S_3$ is successfully prepared by an HP method, and the lattice parameters and normal-state ρ, as well as the density of states at the Fermi level, are found to be comparable with those determined previously. The most notable discovery in this study is the impurity driven SC (>1.6K) in $Bi_4O_4S_3$, which contradicted the results of ongoing studies on this compound. There are two possible reasons for the abovementioned discrepancy: (i) common technical errors, including those related to the presence of superconducting impurity, in the ongoing studies. The impurity is found to be capable of showing zero resistivity, even though its

superconducting shielding fraction is smaller than 0.3 %; (ii) slight local structure and chemical composition differences between the HP phase and the superconducting phase of $Bi_4O_4S_3$, including small variation of the S1–Bi2 bond in the BiS_2 layer as detected in this study. Concentrations of vacancies of SO_4 group in the layered structure of $Bi_4O_4S_3$ might also vary upon the HP heating. If the latter is true, the HP phase can be a host material for the superconducting phase.

As it is very difficult to discuss the details of possible structure and composition variations of $Bi_4O_4S_3$ from normal X-ray diffraction, advanced studies like neutron diffraction are required, I conclude that the SC of the HP prepared $Bi_4O_4S_3$ is most likely impurity driven. The relative sample scale to the λ_L hardly accounted for the negligibly smaller superconducting shielding fraction, as evidenced by the magnetic susceptibility measurements in a magnetic field of 1 Oe as well as 10 Oe on an mm-size HP sample. Hence, full shielding fraction reported in the ongoing studies [1-3]. is possibly complicated by a superconducting link consisting of similar superconducting impurities throughout the grain boundaries and at the surface in a synthesized pellet as evidenced by remarkable decreases of the shielding fraction in a magnetic field of 1 Oe ($<< H_{c1}$) even upon gentle grinding.

Although the various forms of the superconducting link could play a fundamental role of the presence of SC, it was highly challenging to identify chemical composition and structure of the superconducting impurities because partially melted phases can be essential in formation of the superconducting link (Bi melting point: 272°C and S melting point: 115.2°C). Although the Bi powder treated in the same heating procedure as reference is not superconducting above 2K, multiple phases are known to be superconducting with the highest T_c of 8.2K [10]. Thus, neighbor materials in solid and in amorphous forms should be carefully studied for relevance to the observed SC. In addition, surface of the BiS_2 layered phase might be altered under the presence of liquid phases during heating process, resulting in appearance of possible surface superconductivity. No matter which, the observed superconductivity did not truly reflect bulk nature of the BiS_2 layered phase, regardless of the manner in which the $Bi_4O_4S_3$ compound is synthesized. Since the difficulty of identifying the superconducting impurities complicates the ongoing studies, further experimental efforts toward measuring degree of impact from impurities and possible altered particle surfaces on the observed SC would be needed to correctly characterize the BiS_2 layered phase.

While $LaO_{1-x}F_xBiS_2$ phases are successfully prepared using, the high-pressure conditions and I carried out magnetic susceptibility and electrical resistivity measurements. $LaO_{0.5}F_{0.5}BiS_2$ is claimed to be a superconductor with a transition temperature of 10.6K while the current studies clearly prove that the superconducting nature might be due to some un-identified impurities throughout the grain boundaries that might be the reason for the superconducting nature. It was claimed in the previous reports that substitution of fluorine for oxygen was triggering the superconducting nature. But the present results clearly indicate that the small superconducting nature due to the impurity contribution was fairly present throughout the samples with or without substitution of fluorine for oxygen and this clearly states that fluorine has no effect on the superconducting nature throughout different phases. Also from the resistivity measurements, it clearly proved that the samples prepared under the high-pressure conditions shows semiconducting like property like the parent material even after substitution of fluorine. In addition, some unidentified impurities play a key role for the superconducting nature and we guess La_3S_4 phase that has been reported a long back with a T_c of 8.25K might be the reason for the impurity contributed superconducting nature. Further studies are needed to know what is reasonable for the altered impurity that is reasonable for the superconducting nature in BiS_2 layered phase.

References

[1] Y. Mizuguchi, H. Fujihisa, Y. Gotoh, K. Suzuki, H. Usui, K. Kuroki, S. Demura, Y. Takano, H. Izawa, and O. Miura, Phys. Rev. B. **86**, 220510R (2012).

[2] S. G. Tan, L. J. Li, Y. Liu, P. Tong, B. C. Zhao, W. J. Lu, and Y. P. Sun, Physica C. **483**, 94 (2012).

[3] S. K. Singh, A. Kumar, B. Gahtori, Shruti, G. Sharma, S. Patnaik, and V. P. S. Awana, J. Am. Chem. Soc. **134**, 16504 (2012).

[4] H. Kotegawa, Y. Tomita, H. Tou, H. Izawa, Y. Mizuguchi, O. Miura, S. Demura, K. Deguchi, and Y. Takano, Jpn. **81**, 103702 (2012).

[5] S. Li, H. Yang, J. Tao, X. Ding, and H.-H. Wen, arXiv:1207.4955v1.

[6] F. Izumi, and K. Momma, Solid State Phenom. **130**, 15 (2007).

[7] H. Takatsu, Y. Mizuguchi, H. Izawa, O. Miura, and H. Kadowaki, J. Phys. Soc. Jpn. **81**, 125002 (2012).

[8] I. Pallecchi, M. Tropeano, G. Lamura, M. Pani, M. Palombo, A. Palenzona, and M. Puttia, Physica C. **482**, 68 (2012).

[9] E. H. Brandt, Phys. Rev. B. **37**, 2349 (1988).

[10] M. A. Ilina, and E. S. Itskevich, Fiz. Tverd. Tela. **14**, 395 (1972).

[11] J. G. Bednorz, and K. A. Müller, Z. Phys. B. **64,** 189 **(**1986).

[12] M. K. Wu, J. R. Ashburn,C. J. Torng, P. H. Hor, R. L. Meng, L. Gao, Z. J. Huang, Y. Q. Wang, and C. W. Chu, Phy. Rev. Lett. **58**, 908 (1987).

[13] Y. Kamihara, T. Watanabe, M. Hirano, and H. Hosono, J. Am. Chem. Soc. **130**, 3296 (2008).

[14] Hsu F C *et al,* Proc. Natl. Acad. Sci. USA. **105,** 14262 (2008).

[15] J. H. Tapp, Z. Tang, Bing Lv, B. Lorenz, Paul C. W. Chu, and A. M. Guloy, Phys. Rev. B. **78**, 060505R (2008).

[16] Y. Mizuguchi, S. Demura, K. Deguchi, Y. Takano, H. Fujihisa, Y. Gotoh, H. Izawa, and O. Miura et al., arxiv: 1207.3567.

[17] J. Xing, S. Li, X. Ding, H. Yang, and H-H. Wen, Phys. Rev. B. **86**, 214518 (2012).

[18] R. Jha, S. K. Singh, and V. P. S. Awana, arXiv:1208.5873 (2012).

[19] S. Demura, Y. Mizuguchi, K. Deguchi, H. Okazaki, H. Hara, T. Watanabe, S. J. Denholme M. Fujioka, T. Ozaki, H. Fujihisa, Y. Gotoh, O. Miura, T. Yamaguchi, H. Takeya, and Y. Takano, arXiv:1207.5248 (2012).

[20] D. Yazici, K. Huang, B. D. White, A. H. Chang, A. J. Friedman, and M. B. Maple, Phil. Magazine. **93**, 6 (2012).

[21] H. Lei, K. Wang, M. Abeykoon, E. S. Bozin, and C. Petrovic, arXiv:1208.3189v (2012).

[22] G. L. Guthrie, and R. L. Palmer, Pys. Review. **141**, 346-347 (1966).

[23] R. M. Bozorth, F. Holtzberg, and S. Methfessel, Phy. Rev. Lett. **14**, 952-953 (1965).

Chapter 5 Crystal structure and properties of Fe-based silicide system

5.1 Substitution effects of calcium in antiferromagnetic $Yb_2Fe_3Si_5$

In this chapter I would like to explain in detail about the synthesis and characterization of heavy fermion systems like the heavy fermion systems $R_2T_3X_5$ (*R*-rare earth metals, *T*-transition metals, *X*-Si, Ge) and successively studied about the substitution effects using calcium for rare earth element ytterbium. Heavy fermion systems have attracted considerable attention because of their unusual magnetic, electronic, and transport properties. At lower temperatures, some of them exhibit superconducting transitions; for example, rare-earth silicates such as $Lu_2Fe_3Si_5$ and $Tm_2Fe_3Si_5$ shows superconductivity at temperatures of 6.0K and 1.2K, respectively [1-2]. Studies on nonmagnetic impurity doping to superconducting $Lu_2Fe_3Si_5$ revealed rapid suppression of the superconductivity [3]. Studies on the ytterbium (Yb) - based intermetallic compound that crystallizes in a tetragonal (*P*4*/mnc*) structure revealed Kondo-lattice behavior at low temperature with antiferromagnetic (AFM) properties. The absence of superconductivity in heavy fermion systems is likely due to the scattering of electrons influenced by the high density of local magnetic moments. Several reports explain in detail the AFM ordering and the Kondo-lattice behavior in $Yb_2Fe_3Si_5$ [4-6]. However, the application of high pressure and substitution to the heavy fermions remains largely unexplored. I have reported the preparation of $Yb_2Fe_3Si_5$ using a high-pressure and high-temperature synthesis method by substituting calcium (Ca) for Yb in polycrystalline compounds of $Yb_{2-x}Ca_xFe_3Si_5$, which influence the structural, magnetic, and electronic properties. Magnetic and resistivity measurements revealed unusual features, in which the AFM behavior gradually decreased and a semiconductor-like behavior gradually appeared by substituting large amounts of Ca for Yb.

5.1.1 Experimental

Polycrystalline samples of $Yb_{2-x}Ca_xFe_3Si_5$ with x = 0, 0.2, 0.4, 0.6, and 0.8 are synthesized by mixing fine powders of pure Yb (99.9% purity; Rare Metallic Co., Ltd), Iron (Fe; 99.9% purity; Rare Metallic Co., Ltd), Silicon (Si; 99.9% purity; Wako Pure Chemical Industries, Ltd), and calcium silicide (CaSi; laboratory made). CaSi is prepared from Ca and Si pieces (99.9% purity; Rare Metallic Co., Ltd) by an arc melting method in an argon atmosphere by repeatedly arc melting to obtain a homogeneous mixture. Approximately 10%

of Ca pieces is further added to the stoichiometric starting composition during the melting

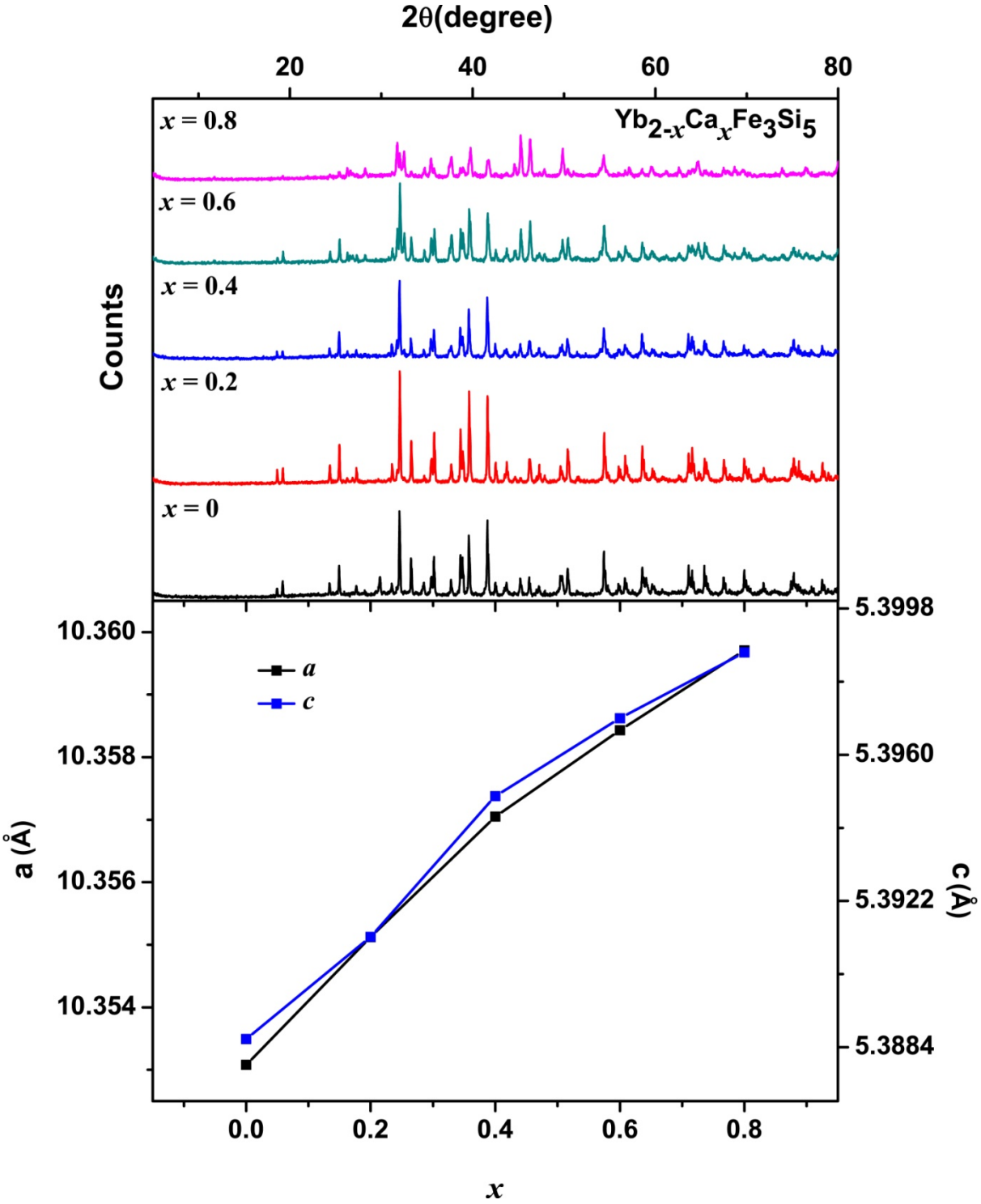

Fig.5.1. (a) Powder XRD patterns of $Yb_{2-x}Ca_xFe_3Si_5$ (x = 0–0.8). (b) Lattice parameters vs. nominal Ca- concentration.

process. A 1:1 ratio of Ca:Si is confirmed by x-ray diffraction (XRD) from a sample of the prepared powder. A well ground mixture of all powders is pressed into a pellet, placed in a pre-prepared pyrophyllite sample cell, and heated in a cubic anvil type high-pressure

apparatus at 1500°C under a pressure of 5 GPa for 20–30 min and quenched to ambient temperature before releasing the pressure. An XRD study is performed to investigate the prepared compounds in ambient temperature conditions using a PANalytical X-pert system with monochromatic Cu-Kα radiation. It should be noted that, substitution by an arc-melting method using metal flakes on a water-cooled heat in the high purity argon atmosphere is unsuccessful as far as we attempted. With temperatures ranging from 2–350 K and an applied magnetic field of 1 kOe, under field-cooling (FC) and zero-field-cooling (ZFC) conditions, magnetic susceptibility (χ) measurements are performed using a magnetic property measurement system (Quantum Design). The electrical resistivity (ρ) of the polycrystalline pellets is measured at temperatures between 2 to 300K by a physical property measurement system (Quantum Design). For the resistivity measurements, gold wires are fixed using silver epoxy over the pellets and the conventional four-terminal method is used; the ac-gauge current and frequency are 1 mA and 110 Hz, respectively.

5.1.2 Structural properties

XRD patterns for $Yb_{2-x}Ca_xFe_3Si_5$ (where x = 0.0, 0.2, 0.4, 0.6, 0.8) is shown in Fig.5.1 (a). Bragg reflections are all indexed very well by a tetragonal unit cell with a space group of *P4/mnc* (128), which agrees well with previously reported results for $Yb_2Fe_3Si_5$ [7]. Lattice parameters are calculated and plotted with respect to *x,* as shown in Fig.5.1 (b), which clearly indicate the gradual increase in the lattice constants *a* and *c* by increasing the substitution percentage of Ca for Yb. This gradual increase in lattice constants clearly indicates the successful substitution of Ca for Yb site. Maximum substitution of Ca for Yb is found at 40%, and further substitution resulted in a structural change that led to distorted phases.

5.1.3 Magnetic properties

For the as measured XRD samples, magnetic susceptibility measurements are carried out under an applied magnetic field of 1 kOe as a function of temperature in ZFC and FC conditions, as shown in Fig. 5.2. This shows an AFM transition at a temperature of 44.5K, which is likely due to the 3*d* spin (Fe) ordering, as suggested previously [5]. With decreased temperature, the curve drops gradually and starts increasing from 8.5K, likely owing to the 4*f* spin (Yb) ordering [5]. Substitution of Ca from 10% to 40% of Yb site show changes in the susceptibility behavior, as shown in the upper half of Fig.5.2; it shows an upturn and the

susceptibility gradually increases with lower temperature to 2K.

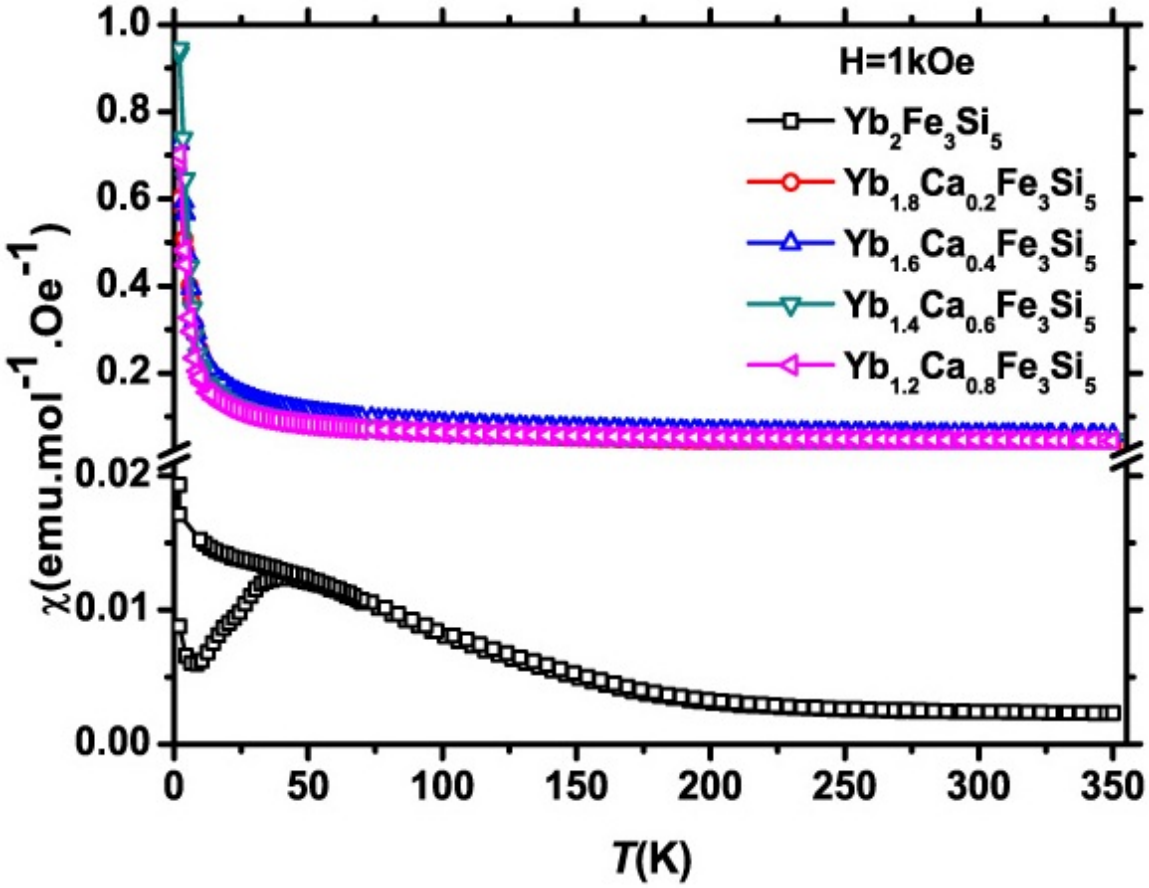

Fig.5.2. *T* dependence of magnetic susceptibility for $Yb_{2-x}Ca_xFe_3Si_5$ (x = 0–0.8), under a magnetic field of 1 kOe.

The paramagnetic characteristics may be due to the decreasing influence of the AFM interactions caused by increasing the Ca substitution. The inverse magnetic susceptibility $1/\chi$ from 2 to 350K for $Yb_{2-x}Ca_xFe_3Si_5$ (where x = 0.0, 0.2, 0.4, 0.6, 0.8) is shown in Fig.5.3. Upon decreasing the temperature in the $Yb_2Fe_3Si_5$ compound below room temperature, $1/\chi$ decreases linearly until 250K and then drops from the Curie–Weiss fitting line. Magnetic susceptibility is explained clearly using the Curie–Weiss law $\chi = \frac{C}{(T-\theta_c)}$, where C is the Curie constant and θ_c is the Weiss temperature. From the value of Curie constant, the effective moment can be calculated using the expression $C = \frac{\mu_{\text{eff}}^2 x}{8}$ (x-concentration of Yb ions) [5-6]. The calculated effective moment of $Yb_2Fe_3Si_5$ is 3.02 μ_B and θ_c is –638.2K. This effective moment is much lower than the combined free ion moments of Yb^{3+} and Fe^{3+}, predicting a mixed valence state. Deviation from the Curie–Weiss plot beyond 250K may be due to Kondo lattice contributions and the crystal field, as discussed in a previous report [8].

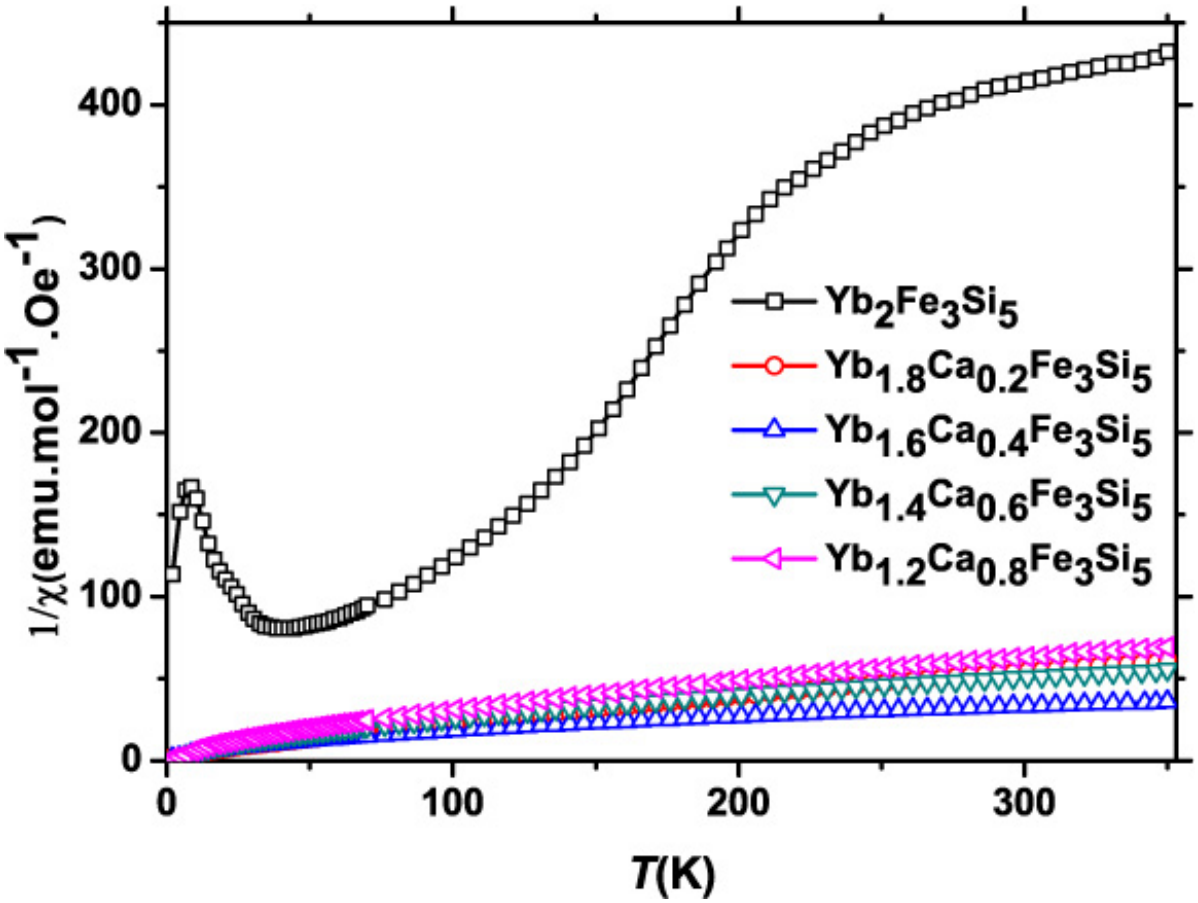

Fig.5.3. *T* dependence of inverse susceptibility for $Yb_{2-x}Ca_xFe_3Si_5$ (x = 0–0.8), under a magnetic field of 1 kOe.

Upon substituting Ca for Yb, the effective moment and θ_c decreased gradually to 3.383 μ_B and -201.5K respectively, in highly Ca substituted $Yb_{1.2}Ca_{0.8}Fe_3Si_5$ compounds. Changes in the effective moment and the negative value of θ_c confirmed again that substitution of Ca for Yb is successful. Unfortunately, 40% substitution of Ca for Yb did not induce superconductivity, likely due to the high scattering rate of the AFM ordered 4*f*-type moments and disorders present in the system.

5.1.4 Transport properties

The temperature dependence of ρ for $Yb_{2-x}Ca_xFe_3Si_5$ (x = 0, 0.2, 0.4, 0.6, 0.8) measured between temperatures of 2 to 300K is shown in Fig.5.4. $Yb_2Fe_3Si_5$ shows a metallic conductivity with higher ρ at room temperature, which slowly decreases with decreasing temperature. The rather poor metallic behavior may be due to scattering related to the highly anisotropic structure of the rare earth iron silicide's [8]. The low temperature region below 35K shows a Kondo-like upturn and below 8K there is a small drop, which corresponds to a

magnetic transition. Substitution of Ca for Yb at x of 0.1 and 0.2, ρ decreases slightly more than the non-substituted Yb site at room temperature. Further substitution of Ca at x of 0.3 to 0.4 shows a change in the conducting property from metal to semiconductor-like behavior. This change is likely governed by the degree of disorder caused by the mixing of Ca and Yb in the structure, otherwise a valance-instability as discussed in Ref. 8.

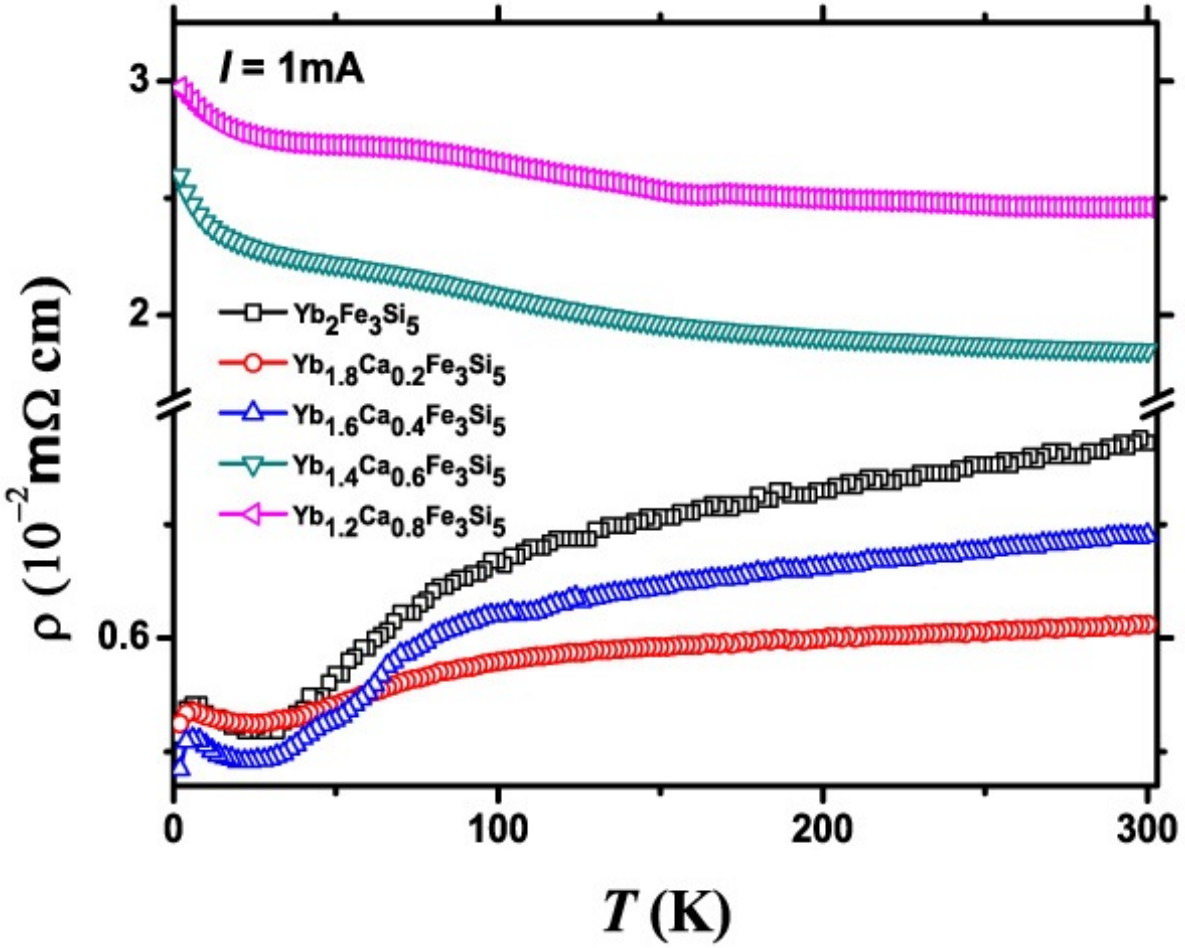

Fig.5.4. T dependence of ρ for $Yb_{2-x}Ca_xFe_3Si_5$ (x = 0–0.8).

5.2 Conclusion

In summary, I have studied the substitution effects of Ca in the polycrystalline $Yb_{2-x}Ca_xFe_3Si_5$ by magnetic susceptibility and electrical resistivity measurements. $Yb_{2-x}Ca_xFe_3Si_5$ (x = 0, 0.2, 0.4, 0.6, 0.8) is successively prepared by using a cubic type multi-anvil high-pressure and high-temperature furnace. Magnetization and electrical conductivity measurements revealed the suppression of the scattering rate in the conduction electrons, which is caused by the substitution of Ca for Yb. The AFM transition with the Kondo-lattice system in the host material gradually decreased by increasing the substituting amount of Ca

to $Yb_{2-x}Ca_xFe_3Si_5$, and became paramagnetic with semiconducting-like behavior. Further studies of substituting to heavy fermion materials will be required to induce superconductivity. Also $REFe_2Si_2$ (RE- rare earth) is successively prepared under high temperature conditions and doping studies are carried out. As further studies are needed to know the exact nature of the properties, experimental results are not included in this thesis.

References

[1] H. F. Braun, Phys. Lett. A. **75**, 5, 386–388 (1980).

[2] J. D. Cashion, G. K. Shenoy, D. Niarchos, P. J. Viccaro, and A. T. Aldred, J. App. Phys. **52**, 2180–2182 (1981).

[3] H. Sasame, T. Masubuchi, K. Takase, Y. Takano, and T. Watanabe, J. Phys: Conf. series: **150**, 052226 (2009).

[4] C. B. Vining, and R. N. Shelton, Phys. Rev. B. **28**, 5, 2732–2742 (1983).

[5] Y. Singh, S. Ramakrishnan, Z. Hossain, and C. Geibel, Phys. Rev. B. **66**, 014415 (2002).

[6] Y. Singh, and S. Ramakrishnan, arXiv: 0303618v1.

[7] H. F. Braun, J. Less, Common Metals. **100**, 105-124 (1984).

[8] B. Becker, S. Ramakrishnan, A. A. Menovsky, G. J. Nieuwenhuys, and J. A. Mydosh, Phys. Rev. Lett. **78**, 1347 (1997).

Chapter 6. General conclusions and Future Prospects

6.1 General conclusions

Superconductivity and magnetism plays a major role in the area of solid-state physics. There are tons of efforts on the synthesis of these materials; they have a good impact in the field of materials science. However, for the past decade these properties are widely studied and still lot of mysteries are existing to be revealed. Studies are mainly focused on the oxide-based materials and less importance are given to the non-oxide phases due to the difficulties in synthesizing these materials. Therefore, my primary aim is to study on the non-oxide materials like the transition carbides, layered bismuth-sulfide and Fe-Si materials. These materials are successively synthesized using the high-pressure and high-temperature synthesis method and to learn about the crystal structure and the intrinsic properties in detail.

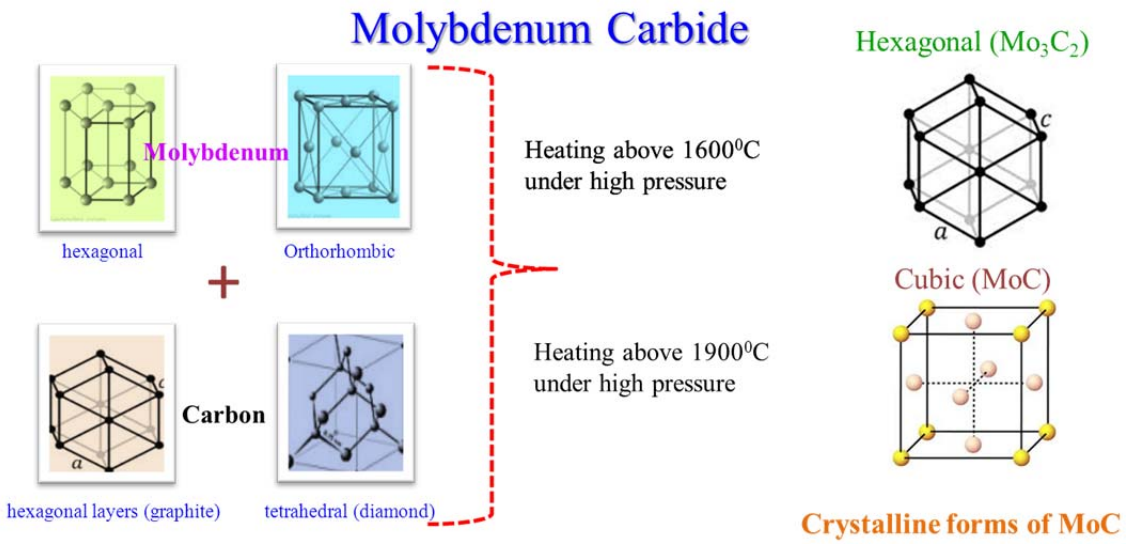

Fig.6.1. Structure views of Hexagonal and cubic MoC

Binary transition carbide materials are widely used in various fields due to their good applications. Most of the transition carbide superconductors are not stable, formation of defect cubic structures are noticed. Mostly MoC crystalizes in a hexagonal structure and cubic phase materials are impossible to be prepared in ambient conditions. Structural views of MoC in hexagonal and cubic forms are shown in Fig.6.1. In addition, the intrinsic properties of these systems are not known yet. To prepare a defect free structure we have utilized the high-pressure and high-temperature technique and we have successively synthesized non-stoichiometric cubic δ-$MoC_{0.681}$ and δ-$MoC_{0.746}$ phases under the high pressure of 6GPa and 17GPa. Crystal systems are analyzed using the neutron, synchrotron

XRD and TEM to find whether some vacancies exist over this phase. The data clearly indicates that the vacancies of carbon did not order in long range and the absence of unusual bonding. This clearly states that the carbon vacancies present in the host cubic structure was found to be robust even when it is prepared from the stoichiometric ratios of carbon and Mo. However, a thermodynamically stable structure with ordered vacancies did not account for the robust features in these phases, the theoretically predicted inherent phonon instability may be the reason for the robust features. The superconducting properties are well studied using a weak coupling model.

When considering the layered type crystal systems, they are expected to show high transition temperatures with good properties in the field of superconductivity and magnetism. Here we focus on the synthesis of BiS_2 layered materials that was recently claimed to be a superconductor. Yet a clear picture of the superconductive nature was a mystery, whether the BiS_2 layer plays as the superconducting layer. So here, I have used the high-pressure synthesis method due to its advantages such as quenching the samples under pressure, and platinum capsules for preparing samples that prevent the escape of gases evolving during synthesizing. Bismuth-sulfide has a low melting point so while heating above its melting point there are possibilities for the formation of eutectic alloys due to slow cooling down and escape of gases while melting process is also possible, this makes the phase to give different properties. It is impossible to overcome these kinds of difficulties in a solid-state synthesis technique. Therefore, HPHT method provides a good route to synthesis these materials under pressure. I have successively synthesized BiS_2 phased $Bi_4O_4S_3$ and $LaOBiS_2$ with additional substitution of fluorine instead of oxygen in $LaOBiS_2$ phase. Studies in these materials clearly states that the superconductive nature appeared in BiS_2 phased materials is due to some unidentified impurities over the grain boundaries. In addition, substitution of fluorine instead of oxygen around 50%-triggered superconductivity is claimed. Result from different characterization techniques clearly indicates that impurity driven superconductive nature was identified from the parent material that exists throughout the substitution and no additional changes happened due to the fluorine substitution is noticed. The material prepared by high-pressure method clearly proved the absence of superconductivity and some unidentified impurities throughout the grain boundaries are the reason for the superconductive nature.

Most of the ternary structured phases that exhibits interesting properties shows

variation in the atomic positions with respect to the unit cell axes. Some unexpected electronic and lattice property changes occur but the same structure and similar lattice properties are retained if there is change in composition is an interesting property in this system [1]. As such in the Fe-Si layered heavy fermion systems only a few superconducting materials are known so far. Notable point in these systems are that Fe atoms donot carry any magnetic moments but helps to build up a large density of states at the Fermi level [2], so this key point can provide researches to develop some useful superconducting materials by substitution studies. In addition, only a few fermion compounds with Fe-Si phases are known and substitution studies are entirely challenging due to practical problems in synthesizing these materials under ambient pressure conditions. Here I have focused on the 235-phase ($RE_2Fe_3Si_5$ where RE-rare-earth) system $Yb_2Fe_3Si_5$ and successively studied in detail about the substitution effects by substituting calcium for Yb up to 40%. The result reveals that the parent compound shows Antiferromagnetic (AFM) transition and by substitution it changed to paramagnetic, but we failed to succeed in preparing superconductors. Our works are now focused on how to overcome the magnetic property shown by the Fe ions in this Fe-Si type system.

6.2 Future Scope of works

Superconductivity and magnetism has given enormous support for the development of useful applications so far. Still there are many unknown truths regarding the superconducting nature and the variations in magnetic nature, so it gives room for research to known more. At present my works are focused on three phases of materials and still there are chances for developing the superconducting nature. My ongoing studies are focused on several projects, among them I am trying to prepare layered molybdenum carbide systems that can contribute high-T_c superconductivity (as layered materials are predicted to show high T_c with good applications). As these binary carbide materials have high melting point and are stable metals in ambient conditions. Also they have good properties which would be very useful if they show extremely high transition temperatures. In the second case of layered Fe-Si materials hole doping or electron doping studies are needed to reduce the large density of states at the Fermi level. So our studies are now focused on doping into the A site and C site of 235 phases by anions and 122 phases like $REFe_2Si_2$ (where RE- rare-earth) too. My main aim is to reduce the magnetic properties arising from the Fe atoms that can help to prepare good superconductors with high T_c. In the case of BiS_2 layered 443 phase systems, I am

preparing different material by changing the C site and doping studies are carried out to introduce the topological insulating systems to show some metallic superconducting properties with high transition temperature. Also the BiS_2 layered $LaOBiS_2$ material shows semiconducting like properties and so substitution studies in La site can help to trigger good superconducting properties is expected.

References

[1] H.F. Braun, J. Less. Comm. Metals. **100**, 105 - 124b (1984).

[2] Y. Singh, S. Ramakrishnan, Z. Hossain, C. Geibel, Phys. Rev. B. **66**, 014415 (2002).

List of appended publications

This thesis is based on the following publications.

1. Scientific papers

[1] **C. I. Sathish**, Y. Guo, X. Wang, Y. Tsujimoto, J. Li, S. Zhang, Y. Matsushita, Y. Shi, H. Tian, H. Yang, J. Li, and K. Yamaura
Superconducting and structural properties of δ-$MoC_{0.681}$ cubic molybdenum carbide phase
J. Solid State Chem. Vol. 196, pp, 579-585 (2012)

[2] **C. I. Sathish**, J. Li, H.-L. Feng, Y. Sun, and K. Yamaura
Substitution effects of calcium in antiferromagnetic $Yb_2Fe_3Si_5$
Physics Procedia. Vol. 45,pp,113-116 (2013)

[3] **C.I. Sathish**, H.-L. Feng, and K. Yamaura
Superconductivity in the bismuth oxysulfide compound $Bi_4O_4S_3$
J. Phys. Soc. Jpn. Vol. 82,pp, 074703 (2013)

2. Verbal presentations

[1] **C. I. Sathish**, Hai-Lukas Feng and Kazunari Yamaura.
Superconductivity in Bismuth Oxysulfide $Bi_4O_4S_3$
12th Asia Pacific Physics conference of AAPPS ASEP3 the Third Asia-Europe Physics Summit, Chiba, Japan.
July. 14-19, 2013.

[2] **C. I. Sathish**, Hai-Lukas Feng and Kazunari Yamaura.
Superconductivity in Bismuth Oxysulfide $Bi_4O_4S_3$
68th Annual meeting, Physical Society Japan (JPS), Hiroshima University, Japan.
March. 26-29, 2013.

[3] **C. I. Sathish**, Hai-Lukas Feng and Kazunari Yamaura.
Superconductivity in Bismuth Oxysulfide $Bi_4O_4S_3$
Challenges in Advanced Chemistry of Asia- HU-NU-SNU-NIMS/MANA Joint Symposium, Sapporo, Japan, Dec. 6-8, 2012.

3. Proceedings

[1] **C. I. Sathish**, Y. Guo, X. Wang, Y. Tsujimoto, J. Li, K. Yamaura

Superconducting and Structural Properties of δ-$MoC_{0.681}$ cubic Molybdenum carbide phase

25th International Symposium on Superconductivity (ISS 2012) Tokyo, Japan. Dec. 4-6, 2012.

[2] **C. I. Sathish**, Y. Guo, X. Wang, Y. Tsujimoto, J. Li, S. Zhang, Y. Matsushita, Y. Shi, H. Tian, H. Yang, J. Li, and K. Yamaura

Superconducting and Structural Properties of δ-$MoC_{0.681}$ cubic Molybdenum carbide phase

IUCr Commission on High Pressure 2012 Meeting "Advances in Crystallography at High Pressures" International Symposium of the Quantum Beam Science Directorate, Japan Atomic Energy Agency, Mito, Japan. Sep. 23-27, 2012.

[3] **C. I. Sathish**, Y. Guo, X. Wang, Y. Tsujimoto, J. Li, K. Yamaura.

Crystal Structure and Superconducting Properties of –$MoC_{1-\delta.}$

ICWNCN Conference, New Delhi, India. Mar. 13-16, 2012.

[4] **C. I. Sathish**, Y. Guo, X. Wang, Y. Tsujimoto, J. Li, K. Yamaura.

Crystal Structure and Superconducting Properties of –$MoC_{1-\delta.}$

24th International Symposium on Superconductivity (ISS 2011) Tokyo, Japan, Oct. 24-26, 2011.

Papers not included in this thesis.

[1] H. L. Feng, **C. I. Sathish**, J. J. Li, X. Wang, and Kazunari Yamaura

Synthesis, structure, and magnetic properties of a new double perovskite Ca_2InOsO_6

Physica C procedia 2013 Vol. 45,pp,113-116 (2013).

[2] Y. Sun, Y. Guo, J. Li, C. Wang, X. Wang, **C. I. Sathish**, and K. Yamaura

The Unusual resistivity behavior and correlated magnetic properties of anti-perovskite $Mn_3Ag_{1-x}M_xN$ (M = Sn, Zn) compounds

Science of Advanced Materials （accepted）.

[3] P. Mohanapriya, **C. I. Sathish**, R. Pradeepkumar, H. Segawa, K. Y. T. S. Natarajan, and N. V. Jaya

OPTICAL AND MAGNETIC STUDIES OF ELECTROSPUN Mn-DOPED SnO_2 HOLLOW NANOFIBER DILUTE MAGNETIC SEMICONDUCTOR

Journal of nanoscience and nanotechnology （accepted）.

[4] A. B. Salunkhe, V. M. Khot, N. D. Thorat, M. R. Phadatare, **C. I. Sathish**, D. S. Dhawale, and S. H. Pawar
Polyvinyl alcohol functionalized cobalt ferrite nanoparticles for biomedical applications
Applied Surface Science 264, 598–604 (2013).

[5] M. R. Phadatare, A. B. Salunkhe, V. M. Khot, **C. I. Sathish**, D. S. Dhawale, and S. H. Pawar
Thermodynamic, structural and magnetic studies in $NiFe_2O_4$ nanoparticles prepared by combustion method: Effect of fuel
Journal of Alloys and Compounds 546, 314–319 (2013).

[6] K. P. S.Prasad, D. S. Dhawale, S. Joseph, C. Anand, M. A. Wahab, A. Mano, **C. I. Sathish**, V. V. Balasubramian, T. Sivakumar, and A. Vinu
Post-synthetic functionalization of mesoporous carbon electrodes with copper oxide nanoparticles for supercapacitor application
Micr & Meso. Mater, 172, 77-86 (2013).

[7] Y. Sun, Y.-F. Guo, Y. Tsujimoto, X. Wang, J. Li, **C. I. Sathish**, C. Wang, and K. Yamaura
Thermodynamic, Electromagnetic, and Lattice Properties of Antiperovskite Mn_3SbN
Advances in Condensed Matter Physics 2013, 286325-1 286325-5 (2013).

[8] Y. Sun, Y. Guo, Y. Tsujimoto, J. Yang, B. Shen, W. Yi, Y. Matsushita, C. Wang, X. Wang, J. Li, **C. I. Sathish**, and K. Yamaura
Carbon-Induced Ferromagnetism in the Antiferromagnetic Metallic Host Material Mn_3ZnN
Inorganic chemistry 52, 800-806 (2013).

[9] H. L. Feng, Y. Tsujimoto, Y. Guo, Y. Sun, **C. I. Sathish**, and K. Yamaura
High pressure synthesis, crystal structure, and magnetic properties of the double-perovskite Sr_2FeOsO_6
High Pressure Research 33, 221-228 (2013).

[10] H. L. Feng, Y. Shi, Y. Guo, J. Li, A. Sato, Y. Sun, X. Wang, S. Yu, **C. I. Sathish**, and K. Yamaura
High-pressure crystal growth and electromagnetic properties of 5d double-perovskite Ca_3OsO_6
Journal of Solid State Chemistry 201, 186-190 (2013).

[11] Y. S. Sun, Y. F. Guo, X. X. Wang, W. Yi, J. J. Li, S. B. Zhang, **C. I. Sathish**, A. A.

Belik, and K. Yamaura

Magnetic and electrical properties of antiperovskite Mn3InN synthesized by a high-pressure method

Journal of Physics: Conference Series 400, 032094-5 (2012).

[12] J. Li, Y. Guo, S. Zhang, J. Yuan, Y. Tsujimoto, X. Wang, **C. I. Sathish**, Y. Sun, S. Yu, W. Yi, K. Yamaura, E. Takayama-Muromachi, Y. Shirako, M. Akaogi, and H. Kontani

Superconductivity suppression of $Ba_{0.5}K_{0.5}Fe_{2-2x}M_{2x}As_2$ single crystals by substitution of transition-metal (M = Mn, Ru, Co, Ni, Cu, and Zn)

Phys. Rev. B 85, 214509 (2012).

[13] J. Li, Y. Guo, S. Zhang, Y. Tsujimoto, X. Wang, **C. I. Sathish**, S. Yu, K. Yamaura, and E. Takayama-Muromachi

Impurity effects on the Fe-based superconductor $A(Fe_{1-y}Co_y)_2As_2$ (A = Ba and Sr)

Solid State Commun. 152, 671-679 (2012).

[14] Y.Tsujimoto, **C. I. Sathish**, K. Hong, K. Oka, M. Azuma, Y. Guo, Y. Matsushita, K. Yamaura, and Eiji Takayama-Muromachi

Crystal structure and Magnetic and Transport properties of Cobalt Oxyfluorides, $Sr_2CoO_{3+x}F_{1-x}$ ($0 \leq x \leq 0.15$)

Inorg. Chem. 51, 4802−4809 (2012).

Acknowledgement

I whole-heartedly would like to thank God for giving me good health and knowledge for performing a healthy atmosphere in my research activities. I should have never achieved this without the faith that I had upon you father almighty.

First, I wish to pay my sincere gratitude to my supervisors Prof. Eiji Takayama-Muromachi and Prof. Dr. Kazunari Yamaura for accepting me as NIMS Junior researcher without any hesitation, followed by enrolling me to the Hokkaido University and continuously supporting me with invaluable guidance throughout my Ph.D. course. I specially thank Prof. Takayama-Muromachi for accepting me to the group of superconductivity and guiding through all the process from the initial days still now even between his busy schedules in the administration of NIMS. I admire his kindness and guiding ways that would be very helpful for me in my future.

I take immense pleasure to express my deep and sincere gratitude to Prof. Yamaura for his guidance throughout my Ph.D. Since I joined under his guidance, he has given good enthusiasm, creative suggestions, motivation and plenty of freedom to work. I have disturbed him to discuss my results even in his busy schedules, but he shares his valuable time to teach me with lots of patience and guide me without any hesitation. I got the opportunity to improve my knowledge in my field during last three years. I admire his hard working style and learned how to work hard and implement my research activities. He has encouraged and supported my collaborations with other groups and it helped me to gain more knowledge in different fields. I hope if I get a chance to work with him I can learn more in my field and achieve great heights.

I would like to pay my sincere thanks to Prof. Teruki Motohashi for his valuable suggestions and ideas throughout my Ph.D. His valuable ideas and suggestions helped me to know more about my research topics.

I would like to thank personally Prof. Ajayan Vinu for his helping mentality and supporting me to achieve a good carrier in my life. Also would like to thank Prof. Naoe Hosoda (NIMS) who accepted me to come to Japan and build up a research carrier and taught me about the basics of research activities. I also thank for the special care and hospitality throughout my stay here so far. I pay my sincere thanks to Dr. Akitsu Shigetou for sharing me good ideas to develop my research, special care and hospitality so far.

I sincerely thank all my group members for all their helps and support, especially for Dr. Yoshihiro Tsujimoto and Dr.Yoshitaka Matsushita for the refinements and

Synchrotron XRD measurements, Drs, Ying Sun, Yan-Feng Guo, for their valuable discussions and helps during my measurements and Dr. Wei Yi, Shan Yu and Xia Wang. I add an extra word to thank Mr. Hai Feng for his good support and help during my Ph.D. In addition, I thank my secretaries Mrs. Shizuko Miyashita and Miss Rumiko Enjoji for their helps throughout my Ph.D.

Additionally, I would like to thank Drs. Yuichi Shirako, Masashi Miyakawa and Takashi Taniguchi, for their kind helps on high-pressure experiments, Dr. Kosuke Kosuda for EPMA, Dr. Akira S Sato for XRD, Dr. Y. Shi for TEM, and Dr. Hiroya Sakurai for PPMS measurements.

I greatly appreciated the support from National Institute for Materials Science and Hokkaido University during my Ph.D. course. I thank for their continuous financial and scientific supports, which helped me to concentrate on my experiments and studies.

Finally, I have no words to thank my parents for their immense support, love, wisdom and prayers. It is my pleasure to thank them for the primary educations they have given me that helped to achieve this PhD course. I also thank my Brothers and Sister for their care, support and understanding. I thank all my friends and relatives for their kind support. Specially, I thank my friend Mr. A. Mano for his encouragement and motivation throughout my studies and still now.